

AN ABSTRACT OF THE THESIS OF

Mario A. Apreotesi for the degree of Master of Science in Mechanical Engineering
presented on June 8, 2007.

Title: Microscale Thermal Management Utilizing Vapor Extraction from a Fractal-
like Branching Heat Sink

Abstract approved:

Deborah V. Pence

It is hypothesized that increases in pressure drop due to vapor generation during boiling in microchannels can be reduced by extraction of vapor at its point of inception. Ultimately, this local vapor extraction decreases the pressure drop required to drive the flow through a fractal-like branching, microchannel flow network within the heat sink. Indeed, by lowering the overall flow rate by vapor extraction the pressure drop can, in principle, be lowered to that of single-phase flow. In the current study, the feasibility of vapor extraction and its influence on the pressure drop across the microchannels are investigated. The concept also has the potential to separate flow independent of heat sink orientation or the influence of gravity.

The fractal-like flow network used here is one that has been previously shown to reduce pressure drop and yield a more uniform surface temperature distribution for single-phase flows than that observed in parallel microchannel flow networks. The disk shaped heat sink was covered with two porous Nylon membranes with an average

pore size of 0.45 microns that were backed with a porous aluminum block. Deionized, degassed water was used as the working fluid.

A theoretical model was developed to predict the pressure drop across the flow network as a function of inlet mass flow rate, heat input, and pressure difference driving extraction across the membranes. Results of the model predictions are presented and discussed in both dimensional and non-dimensional format. Model predictions were used to discuss the trends and physical implications of local vapor extraction. It was observed that conditions existed where further increases in the membrane pressure difference had no influence vapor extraction and network pressure drop values. Experimental data was also collected and analyzed in order to assess the validity of the theoretical model.

The predictive model and experimental data indicated that the two-phase network pressure drop is reduced by locally extracting vapor from the heat sink. The network pressure drop was reduced by as much as 80% theoretically and 50% experimentally in the predictive model and experimental data, respectively, for similar test conditions. A sensitivity analysis was performed on several parameters used in the model in an attempt to help explain some of the discrepancies observed between the experimental results and model predictions. Suggestions are made to improve the theoretical model pressure predictions and to investigate the influence of vapor extraction on the heat transfer coefficient values.

©Copyright by Mario A. Apreotesi

June 8, 2007

All Rights Reserved

Microscale Thermal Management Utilizing Vapor Extraction from a Fractal-like
Branching Heat Sink

by
Mario A. Apreotesi

A THESIS

submitted to

Oregon State University

in partial fulfillment of
the requirements for the
degree of

Master of Science

Presented June 8, 2007
Commencement June 2008

Master of Science thesis of Mario A. Apreotesi presented on June 8, 2007.

APPROVED:

Major Professor, representing Mechanical Engineering

Head of the Department of Mechanical Engineering

Dean of the Graduate School

I understand that my thesis will become part of the permanent collection of Oregon State University libraries. My signature below authorizes release of my thesis to any reader upon request.

Mario A. Apreotesi, Author

ACKNOWLEDGEMENTS

I would like to thank my wife, Angela, for her continual support and assistance. She spent many long hours in the lab helping me fix many problems, taking experimental data, and reassuring me that it would be finished one day. I would also like to thank Dr. Deb Pence and Dr. James Liburdy for their continual input and direction in completing this project and paper. Thanks are also extended to Dr. Vinod Narayanan and Dr. Murty Kanury for their help with different aspects of this project and always being willing to answer my questions and to Greg Mouchka, Keith Davis, and Alex Tulchinsky for their help with aspects of the experimental flow loop design and construction.

TABLE OF CONTENTS

	<u>Page</u>
1 Introduction	1
1.1 Microscale Heat Sinks	1
1.2 Branching Fractal-like Microchannels	2
1.3 Local Vapor Extraction	3
1.4 Objectives	4
2 Literature Review	5
2.1 Forced-air Convection	5
2.2 Single-phase Microscale Flows	5
2.3 Branching Fractal-like Microchannels	6
2.4 Two-phase Flows	8
2.5 Porous Surfaces	11
2.6 Modeling	12
3 Predictive Model Development	18
3.1 Governing Equations and Correlations	18
3.2 Model Setup	26
4 Experimental Apparatus and Procedure	29
4.1 Fractal Network	30
4.2 Test Manifold	35
4.3 Flow Loop	39
4.4 Test Plan	42

TABLE OF CONTENTS (Continued)

	<u>Page</u>
4.5 Data Acquisition	43
4.6 Operating Procedure Summary	45
5 Data Reduction and Analysis	48
5.1 Performance Characteristics	48
5.2 Uncertainty	59
6 Results and Discussion	66
6.1 Predictive Model Results	66
6.2 Predictive Model Validation	76
6.3 Sensitivity Analysis	81
7 Conclusions and Recommendations	91
References	95
Appendices	100

LIST OF FIGURES

<u>Figure</u>		<u>Page</u>
2.1	Typical two-phase flow patterns in horizontal channels similar to that found in [29].	14
3.1	Schematic of the discretization scheme employed in the predictive model.	22
4.1	Schematic of the microscale heat sink comprised of a fractal network, porous membrane and porous aluminum heater.	29
4.2	The microchannel fractal element used in the current study [9].	30
4.3	Representation of a subset of the fractal network showing the different branch levels [27].	31
4.4	Image of the top laminate piece with supporting bridges before being diffusion bonded to the bottom laminate [43].	33
4.5	Image of a channel blank removed from the top laminate after cutting the fractal pattern on the micromachining laser [43].	33
4.6	Detailed schematic of the test manifold.	35
4.7	Schematic representing the layout of the experimental flow loop for the current study.	40
5.1	Schematic of thermal resistance analogy used to approximate heat loss to the surroundings.	55
5.2	Plot of the pressure reading of the vapor plenum pressure transducer as a function of the output voltage.	62
6.1	The vapor mass flow rate versus the membrane pressure difference for an inlet flow rate of 4 g/min for six heat input values.	67
6.2	The normalized extracted vapor flow rate versus the normalized membrane pressure difference for an input heat of 12 W for four inlet flow rates.	68

LIST OF FIGURES (Continued)

<u>Figure</u>		<u>Page</u>
6.3	The normalized extracted vapor flow rate versus the normalized membrane pressure difference for an input heat of 60 W for four inlet flow rates.	70
6.4	Network pressure drop versus the membrane pressure difference for an inlet flow rate of 4 g/min and six input energy values.	70
6.5	Fractal pressure drop versus the membrane pressure difference for an inlet flow rate of 16 g/min and six input energy values.	71
6.6	Normalized network pressure drop reduction versus normalized membrane pressure difference for an inlet flow rate of 4 g/min and six input energy values.	73
6.7	Normalized network pressure drop reduction versus the normalized membrane pressure difference for an inlet flow rate of 16 g/min and six input energy values.	74
6.8	Benefit-to-cost power ratio versus the membrane pressure difference for an inlet flow rate of 4 g/min and six input energy values.	75
6.9	Benefit-to-cost power ratio versus the membrane pressure difference for an inlet flow rate of 16 g/min and six input energy values.	76
6.10	Normalized extracted vapor flow rate versus normalized membrane pressure difference of the predictive model and experimental data for an inlet flow rate of 8 g/min.	78
6.11	Network pressure drop versus membrane pressure difference of the predictive model and experimental data for an inlet flow rate of 10 g/min.	80
6.12	Sensitivity analysis of the network pressure drop versus the membrane pressure difference for perturbed values of the inlet flow rate and exit plenum pressure.	84
6.13	Sensitivity analysis of the extracted vapor flow rate versus the membrane pressure difference for perturbed values of the inlet flow rate and exit plenum pressure.	84

LIST OF FIGURES (Continued)

<u>Figure</u>		<u>Page</u>
6.14	Sensitivity analysis of the network pressure drop versus the membrane pressure difference for perturbed values of the inlet subcooling and input energy.	85
6.15	Sensitivity analysis of the extracted vapor flow rate versus the membrane pressure difference for perturbed values of the inlet subcooling and input energy.	85
6.16	Sensitivity analysis of the network pressure drop versus the membrane pressure difference for perturbed values of the microchannel height, membrane thickness and membrane permeability.	86
6.17	Sensitivity analysis of the extracted vapor flow rate versus the membrane pressure difference for perturbed values of the microchannel height, membrane thickness and membrane permeability.	87

LIST OF TABLES

<u>Table</u>		<u>Page</u>
2.1	Phase interaction parameter correlations.	16
2.2	Void fraction correlations.	16
3.1	Tabulated values for the constants used in Eqs. (3.2) and (3.6) [41].	20
4.1	Channel dimensions of the fractal network (see Figs. 4.2 and 4.3).	32
4.2	Summary of independent variables and their respective values.	43
4.3	Matrix of experimental runs evaluated.	44
5.1	Coefficients values used in Eqs. (5.3) - (5.6).	50
6.1	Base case and perturbed values for the parameters and variables of interest in the sensitivity analysis.	82

LIST OF APPENDICES

	<u>Page</u>
Appendix A: Test Manifold Detail Drawings	101
Appendix B: Experimental Setup Images	105
Appendix C: Component List	108
Appendix D: Calibration and Uncertainty Values	109
Appendix E: Operating Procedure	110
Appendix F: Design Specifications	113
Appendix G: Experimental Data and Predictive Model Results	117
Appendix H: Single-phase Sensitivity Analysis	120

LIST OF APPENDIX FIGURES

<u>Figure</u>		<u>Page</u>
1.A	Exploded view of the test manifold assembly.	101
2.A	Drawing of the clamp enclosing the entire assembly.	102
3.A	Bottom filler piece of fixture through which the flow enters the microchannels.	102
4.A	Porous aluminum layer with path of embedded wire shown.	103
5.A	Top filler part through which the extracted vapor exits.	103
6.A	Encasing to enclose the inner parts of the test manifold.	104
1.B	Image of inlet flow entering and exiting hot oil reservoir to be preheated.	106
2.B	Image of supply tank (clear), bladder tank (white) and surge tank (grey).	106
3.B	Catch and weigh system used to measure flow rate of extracted vapor including liquid collector and condenser.	106
4.B	Transducers used to measure the temperature, pressure and flow rate of the inlet and exit flow lines.	106
5.B	Test manifold with flow lines and its transducers to measure the needed flow properties.	107
6.B	Example of the porous aluminum heater used in this project before embedding the resistance wire.	107
1.G	Normalized extracted vapor flow rate versus normalized membrane pressure difference of the predictive model and experimental data for an inlet flow rate of 10 g/min.	117
2.G	Normalized extracted vapor flow rate versus normalized membrane pressure difference of the predictive model and experimental data for an inlet flow rate of 12 g/min.	118

LIST OF APPENDIX FIGURES (Continued)

<u>Figure</u>		<u>Page</u>
3.G	Network pressure drop versus membrane pressure difference of the predictive model and experimental data for an inlet flow rate of 8 g/min.	118
4.G	Network pressure drop versus membrane pressure difference of the predictive model and experimental data for an inlet flow rate of 12 g/min.	119
1.H	Single-phase sensitivity analysis of the network pressure drop versus the inlet flow rate for perturbed values of the inlet flow rate and exit plenum pressure.	120
2.H	Single-phase sensitivity analysis of the network pressure drop versus the inlet flow rate for perturbed values of the microchannel height.	121

LIST OF APPENDIX TABLES

<u>Table</u>		<u>Page</u>
1.C	Experimental flow loop components.	108
2.C	Instrumentation components.	108
1.D	Calibration curve, uncertainty, and range for each measurement device.	109

NOMENCLATURE

Symbols

A	area
A_z	surface wall area from inlet to z
AC	constant used in Eq. (4.1)
B	inverse mean temperature or volumetric thermal expansion coefficient
C	constant used in Eq. (3.6)
C_{LM}	phase interaction parameter
c_p	specific heat
d	diameter
$d\hat{z}$	differential distance along the flow
D	Euclidian dimension
D_h	hydraulic diameter
e	error
f	friction factor, frequency output of instrumentation
f_{app}	apparent friction factor
f_D	Darcy friction factor
g	gravity constant
G	mass flux
h	heat transfer coefficient
h_f	frictional head loss
H	height of channel
i	enthalpy
I_{ps}	power supply current
k	thermal conductivity
K_{con}	contraction pressure drop coefficient
K_{exp}	expansion pressure drop coefficient
K_{hd}	hydrodynamic entrance length coefficient
K_{90}	ninety degree bend pressure drop coefficient
$K^{(\infty)}$	incremental pressure defect coefficient
L	length, thickness
m	polynomial order
\dot{m}	mass flow rate
M	replications
n	number of branches
N	total number of data points or samples
N_0	number of 0 th level branches
N_M	number of terminal branches
Nu	Nusselt number
P	pressure
\wp_0	Flow power across heat sink with no vapor extraction
\wp_{frac}	Flow power across heat sink

\wp_{vap}	Work done to extract vapor from microchannels
Pr	Prandtl number
\dot{Q}	rate of heat transferred
\dot{Q}''	rate of heat flux across a boundary
R	dependent variable, thermal resistance
R_T	thermal resistance
Ra	Rayleigh number
Re	Reynolds number
S	shape factor
S_x	standard deviation
$\langle S_{\bar{x}} \rangle$	pooled standard deviation of the means
t	Student-t distribution factor
T	temperature
u_B	bias uncertainty
u_P	precision uncertainty
$u_{\bar{x}}$	total uncertainty of an independent variable
u_R	uncertainty of a dependent variable
\bar{U}	overall heat transfer coefficient
v	specific volume
V	flow velocity
\bar{v}	Darcy velocity
V_{ps}	voltage across the power supplies
w	channel width
x	thermodynamic quality
x_i	independent variable
x'	estimate of true measured value
x^+	non-dimensional entrance region length
$\langle \bar{x} \rangle$	pooled mean
X^2	Lockhart-Martinelli parameter
y	data point
z	stream wise flow distance

Greek Symbols

α	actual void fraction, thermal diffusivity
α_{ch}	channel aspect ratio
β	channel diameter ratio
β_v	homogeneous void fraction
γ	length ratio
ΔP	pressure drop or pressure difference
ΔP_0	pressure drop across fractal network with no vapor extraction
ΔT_{sc}	amount of inlet subcooling
Δy	change in gravitational head or elevation
Δz	change in length in the streamwise direction

ε	emissivity
ζ	percent of flow extracted
θ	area ratios
κ	specific permeability
μ	dynamic viscosity
ν	kinematic viscosity
ρ	density
σ	Boltzman's constant
v	degrees of freedom
ϕ^2	two-phase multiplier

Subscripts

1ϕ	single-phase flow or regime
2ϕ	two-phase flow or regime
a	actual value
acc	accelerational
al	porous aluminum
$bend$	ninety degree bend
ci	predicted data value
$cont$	area contraction
cs	cross-sectional
$curvefit$	curve fit
CV	control volume
ex	exit, exit plenum
exp	area expansion
ext	extraction or membrane pressure difference
fcv	forced convection
fd	fully developed flow
$frac$	fractal
$fric$	frictional
$grav$	gravitational
hd	hydrodynamically developing flow
htr	heater
i	inner
in	inlet
k	branch level of fractal network
l	saturated liquid or liquid phase
lo	liquid only
m	measured value, mean or bulk temperature
max	maximum
mem	porous membranes
M	number of branch levels
ncv	natural convection
o	outer

<i>out</i>	out
<i>peek</i>	PEEK™ material
<i>pred</i>	predicted value
<i>rad</i>	radiation
<i>s</i>	side or radial two-dimensional conduction
<i>sample</i>	samples or repetitions
<i>sat</i>	saturated
<i>standard</i>	calibration instrument (standard) uncertainty
<i>std</i>	standard error of calibration curve fit
<i>surf</i>	surface
<i>tot</i>	total
<i>v</i>	saturated vapor
<i>vap</i>	extracted vapor; vapor plenum
<i>V</i>	experimental procedure variants
<i>x</i>	independent variable
∞	free stream

MICROSCALE THERMAL MANAGEMENT UTILIZING VAPOR EXTRACTION FROM A FRACTAL-LIKE BRANCHING HEAT SINK

1 INTRODUCTION

With the emergence of new technological applications in the last few decades, the need for efficient and effective thermal management continues to increase. The greatest needs are arising in microelectronics. With the development of further miniaturization in microelectronics and increased processor speeds, thermal management is drastically affecting overall packaging and system capabilities. The cooling of electronics and other microscale applications is fundamentally different from that of most conventional cooling applications. Not only does the heat need to be removed, but the object needs to be maintained at a low and relatively uniform and stable temperature. Due to the special needs introduced by these new applications, research focusing on microscale heat sinks has increased.

1.1 Microscale Heat Sinks

Thermal management in microscale channel geometries is advantageous due to the high surface area per unit volume, the large heat transfer coefficients, low flow rate requirements and minimal refrigerant volume. It should be noted that microchannels are defined as those containing hydraulic diameters ranging nominally between 10 and 200 μm . For a given Nusselt number, as the hydraulic diameter of the channel decreases, the heat transfer coefficient value increases proportionally. If a

phase change is experienced, the latent heat required to vaporize the flow can further increase the heat transfer coefficient value.

However, microscale heat sinks have some drawbacks. As the cross-section of a channel decreases, the pumping power for a fixed flow rate required to drive the flow through the microchannel increases. This is similar to the greater effort required to blow up a balloon with a restricted opening. This problem is more pronounced for a given flow rate with two-phase flows due to the greatly increased velocity resulting from the decreased density. The benefits of microscale heat sinks can be overshadowed if the pump required to drive the refrigerant flow is the same size as the electronic piece to be cooled, e.g. a computer.

Initial microscale heat sink research focused on single phase flows. From the numerous studies performed, large stream-wise increases in the bulk fluid temperature and heat sink temperature were observed. This inability to maintain a uniform heat sink temperature can lead to uneven thermal expansion of the surrounding materials causing probable changes in the electrical properties and mechanical fatigue of a circuit board. To compensate for the stream-wise increasing temperature, flow rates can be increased, but not without resulting in larger pressure drops. To improve the pressure drop across and temperature distribution along microscale heat sinks, branching fractal-like microchannel networks have been researched.

1.2 Branching Fractal-like Microchannels

Recent breakthroughs have been made to implement the same fractal-like flow networks used in natural and biological processes to overcome high pressure drops in

microchannel flows. Representative examples of fractal-like channel structures are the circulatory system of the human body and root systems found in plants. As either stretches out from its source, the hydraulic diameter slowly decreases as it branches in to more and more ‘sub channels’ resulting in an increase of the flow area. This efficient design accounts for the relatively minimal size of the human heart in comparison to our expansive circulatory system. Implementation of this nature-inspired network design instead of traditional parallel, straight microchannel arrays has the potential to drastically reduce the pressure drop across microscale heat sinks and reduce stream-wise temperature gradients in both single-phase and two-phase flows.

1.3 Local Vapor Extraction

In the present study, the performance of branching fractal-like microchannels may be improved by locally extracting vapor from the two-phase flow through a porous hydrophobic membrane. In this scenario, the large heat transfer coefficient values of two-phase flows are achieved by allowing the flow to reach saturation and incipient boiling. However, the vapor is removed where it is formed rather than having to be pushed through the entire flow network, which ultimately reduces the pressure drop across the heat sink to values similar to those achieved with single-phase flows. Reduction in the amount of vapor present in the flow should also increase local heat transfer rates. Simply, the result is a combination of the positive characteristics of both two-phase and single-phase flows. This idea may have the added benefit of being useful in situations of low gravity. As gravity is no longer required to separate

the vapor from the liquid phase, this application would be feasible in any spatial orientation.

1.4 Objectives

The scope of this study is to validate the hypothesis that the local extraction of vapor utilizing a relatively small pressure differential across a hydrophobic, porous membrane from two-phase flows in branching microchannel heat sinks should maintain the high heat flux capabilities of two-phase flows, but with a reduced stream-wise (radial) pressure drop. The objectives of this thesis are to:

1. develop a model for predicting local vapor extraction and pressure distribution along a branching, microchannel flow network and examining the viability of the thesis project,
2. design, fabricate and instrument an experimental apparatus with which to test the validity of the predictive model with experimental data, and
3. evaluate and quantify the effect of vapor extraction on heat sink performance.

2 LITERATURE REVIEW

As the performance of electronics has increased and their size has miniaturized, research focusing on microscale heat sinks has increased. The evolution of microelectronics has been closely followed by a similar trend in microscale thermal management processes and methods.

2.1 Forced-air Convection

The early investigations in microscale thermal management looked to the conventional cooling process: forced-air convective heat transfer. The size, shape and configuration of electronic modules were investigated to maximize cooling capacity from circuit boards using forced-air convection over the circuit board. Representative studies of forced-air convection cooling include Sparrow et al. [1] investigating the convective heat transfer for air flows in arrays of heat-generating square modules located along one wall of a flat rectangular duct. Jubran et al. [2] furthered such studies by investigating the convective heat transfer of rectangular and cylindrical modules. As the microelectronics capabilities continued to increase along with increasing miniaturization, the heat density being generated and needing to be dissipated increased. Soon thereafter, the upper limits of heat transfer coefficients for forced-air convection cooling were reached. Consequently, new methods were considered and investigations into microchannel heat sinks began.

2.2 Single-phase Microscale Flows

As discussed, thermal management in microscale channel geometries is advantageous due to the high surface area per unit volume, the large heat transfer

coefficients, and minimal volume. Initial research and applications of heat sinks comprised of microchannels centered on single-phase flow. Such studies have been abundant since the pioneering investigation of Tuckerman and Pease [3]. In their report, they proposed that a theoretical cooling capacity of 1000 W/cm^2 could be achieved using single-phase flow in microchannel heat sinks. This objective has become the benchmark for microscale cooling capacity. Their experimental setup was optimized to reach a cooling capacity of 790 W/cm^2 . Qu and Mudawar [4] continued single-phase studies in microchannels and concluded that the outlet fluid temperature and the temperature of the fluid in the heat sink decrease at the expense of a greater pressure drop across the heat sink. Zhang et al. [5] showed that for single-phase flow in microchannels the pressure drop across the microchannels decreases with increasing input power. This inverse relationship is due to the decrease in the liquid viscosity resulting from the increased temperature. From these studies [3-5], large stream-wise increases in the bulk fluid temperature and heat sink temperature were observed. Non-uniform heat sink temperature distribution leads to uneven thermal expansion of the materials causing changes in the electrical properties and mechanical fatigue. Compensations were made by greatly increasing the flow rates resulting in larger pressure drops.

2.3 Branching Fractal-like Microchannels

To improve the cooling characteristics of single-phase flow in microchannels other studies have been performed by re-evaluating the channel geometry and network arrangement of the channels. Bau [6] demonstrated with mathematical models that the

optimization of variable cross-sectional microchannels reduced the maximum temperature and minimized temperature gradients along the length of the channel. Reduction of the surface temperature resulted from tapering the channel in the stream-wise direction. However, this decrease in the stream-wise channel diameter led to an increased velocity and hence increased the pressure drop and pumping power required. Ideally, it is desirable to achieve similar surface temperature distributions without an increased pressure drop. Recently, breakthroughs have been made to implement the same fractal-like flow networks used in natural and biological processes to overcome high pressure drops in microchannel flows. Representative examples of fractal-like channel structures include the circulatory system of the human body and root systems found in plants. The hydraulic diameter slowly decreases in the stream-wise direction. Following proposals made by West et al. [7] fractal-like networks have been engineered with fixed diameter and length scale ratios between consecutive branching levels. Pence [8] first proposed that this geometric layout of the channels, along with helping to reduce the pressure drop, ensures a more even distribution of the flow and surface wall temperature. Later studies by Pence [9] validated those proposals by comparing heat sinks with this fractal-like flow network to those with the conventional parallel channel array. The maximum channel wall temperature and the total pressure drop across a heat sink were the characteristics of interest. The studies concluded that similar maximum wall temperatures and total pressure drop across the heat sink were obtained with a fifty percent less density for the fractal-like network—the fractal-like network provided superior results. In another study, Pence and Enfield [10] defined benefit-to-cost ratio as the quotient of the advected energy dispelled from a surface

and of the flow power. Heat sinks with fractal-like branching networks and parallel channel networks were compared and it was shown that fractal-like networks have a greater benefit-to-cost ratio. The fractal network design improves the performance of microchannels in single-phase flows and is anticipated to enhance the performance of two-phase flows as well.

2.4 Two-phase Flows

Two-phase boiling microchannel studies offer two advantages over single-phase flow in microchannels: nearly uniform heat sink temperature near the fluid saturation temperature and lower fluid flow rates for the same cooling load. The conventional layout of microchannels (and heat sinks in general) with a series of parallel straight channels often leads to several difficulties. Numerous two-phase boiling microchannel studies have been performed revealing the details of these difficulties. Mertz et al. [11] reported fluctuations of the two-phase flow and maldistribution of the phases within a parallel series of microchannels. In separate investigations of two-phase pressure drop in parallel microchannels, Qu and Mudawar [12] observed similar phenomena and identified two types of two-phase instability: pressure drop oscillation and parallel channel instability. Pressure drop oscillation produced periodic, large-amplitude flow oscillations, which could trigger dry-out (critical heat flux—CHF). Parallel channel instability produced only mild flow fluctuations resulting in less frequent occurrences of dry-out. Along with dry-out, flow reversal was observed by Steinke and Kandlikar [13] in an investigation of two-phase boiling of water in parallel microchannels. Rapid evaporation of liquid in the

contact line region led to dry-out and with the absence of film on the heated surface, the local surface temperature rapidly increased. In these investigations, dry-out was occasionally observed in entire channels. Similar results were reported by Jiang et al. [14] in studying even smaller microchannels having hydraulic diameters of 26 and 53 μm . In all these investigations, dry-out was followed by extremely high temperatures that would lead to electronics failure. Parallel channel instability also produced a non-uniform temperature distribution.

The investigations of Jiang et al. [14] also reported an appreciable pressure drop increase upon the commencement of boiling in the microchannels. Similar pressure drop increases shortly after the onset of boiling were reported by Zhang et al. [15]. Their studies accounted for this sharp increase by observing that the density of the vapor is much less than that of the liquid leading to a sudden increase in the local volumetric flow rate. The local acceleration of the flow results in the increased pressure drop. Overall, the two-phase studies in parallel microchannels observed greater pressure drop than that in single-phase flow and flow instabilities leading to possible dry-out and/or non-uniform temperature distribution.

Daniels et al. [16] performed a numerical analysis comparing two-phase convective boiling pressure drop in parallel flow and fractal-like branching flow networks. The pressure drops in the parallel channel configurations were significantly higher than those in fractal-like networks with equivalent wall surface area and exit channel geometry.

Similar to conventional network geometries, the study by Daniels et al. [16] shows that pressure drops are still substantially greater in two-phase flows in

branching fractal-like microchannels than single-phase flows. Despite the fact that the higher pressure drops anticipated in two-phase flow make the use of two-phase microchannels less desirable, the latent energy exchange is required for high heat flux applications and to ensure a uniform temperature distribution. Investigations of Qu and Mudawar [17] using water in parallel microchannels demonstrated that the heat transfer coefficient in two-phase flow decreases with increasing thermodynamic quality and increases with increasing mass velocity. Several explanations have been proposed to explain this decrease in heat transfer coefficient with increasing quality. Ravigururajan [18] proposed that this phenomenon can be explained by possible blockage of channel cross-sections by vapor bubbles. Kew and Cornwell [19] and Warriar et al. [20] attribute this to local dry-out occurring beneath the vapor bubbles. On the other hand, Qu and Mudawar [17] proposed that the unique behavior of annular flow in microchannels accounts for this phenomenon. By definition, annular flow consists of a vapor core that is surrounded by a liquid annular film along the channel wall and contains liquid droplets entrained within it. Their proposal introduces the possibility that a large amount of liquid droplets become entrained in the vapor core at the onset of annular flow. The liquid film thickness increases in the stream-wise direction as these liquid droplets are deposited into the annular liquid film, resulting in an increased film thickness and the observed decrease of heat transfer coefficient values with increasing quality. This inverse relationship between the heat transfer coefficient and the fluid quality is central to this project and has been validated by other investigations. Steinke and Kandlikar [13], also using water as the working fluid, reported very large values for the heat transfer coefficient in the low quality

region with a sharp decline in the coefficient values as the quality increased.

Refrigerant studies performed by Yen et al. [21] observed similar heat transfer coefficient characteristics in microchannel tubes. One of the objectives of this thesis project is to utilize, via local vapor extraction, the large heat transfer coefficient values observed in the low quality region.

2.5 Porous Surfaces

Recently studies have been performed evaluating the performance of convective boiling using a porous surface coating. The first investigations evaluated the effect of a porous surface in pool boiling applications and showed remarkable improvements in heat transfer coefficients and critical heat flux. Subsequent studies examined internal porous coatings on flow boiling. Ikeuchi et al. [22] plated the internal surface of a 17.05 mm diameter tube with 0.115 mm diameter copper particles. Heat transfer coefficient values were improved by approximately five times. Ammerman and You [23] investigated the performance of surface coating in square minichannels and reported similar heat transfer improvements. In the present study, the purpose of the membrane is to facilitate the extraction of vapor; however, the membrane like the porous surface coatings may also help improve the heat transfer characteristics. The feasibility of locally extracting vapor through a porous membrane was shown by Thorud et al. [24]. Using a porous membrane to extract vapor in a high aspect microchannel desorber, they improved the overall rates of desorption of water from an aqueous lithium bromide mixture. The use of porous membranes in the current study is expected to facilitate the extraction of water vapor from the two-phase

flow in the microchannels. The possible improved heat transfer characteristics of the heat sink due to porous membrane will not be investigated.

2.6 Modeling

There are many well-established modeling methods for accurately predicting pressure drop and heat transfer in macroscale flows. Several of these models have been modified to characterize single-phase and two-phase flows for microscale applications.

2.6.1 Single-phase Models

Pence [9] developed a one-dimensional model for predicting pressure and wall-temperature distribution for single-phase flows in fractal-like branching channel networks. The model is based on laminar flow with a constant heat flux applied to the walls of the flow network. Model assumptions included that the thermal and hydrodynamic boundary layer redevelop at the entrance of each new branching level. Pressure drop calculations from the correlation provided in White [25] included the effect due to frictional head loss, core acceleration, and higher shear stress present in the hydrodynamically developing region. In Pence [9], the axial wall temperature of the channel is obtained from Newton's law of cooling and the bulk fluid temperature is determined from an energy balance. Alharbi et al. [26, 27] validated both the pressure drop and heat transfer characteristics models with a fully three-dimensional computational fluid dynamic analysis.

2.6.2 Two-phase Models

Two-phase one-dimensional models fall into two general categories: homogenous flow models and separated flow models. The first model is better suited to deal with mixed flow such as bubble flow and slug flow, while the second is better applied in stratified and annular flow. Examples of two-phase flow patterns are showed in Fig. 2.1. Flow visualization studies have been performed on two-phase water flow in microchannel heat sinks by Qu and Mudawar [28]. Their studies indicate that annular flow is the dominant flow pattern with a large amount of liquid droplets entrained in the vapor core. Several previous visualization studies support this conclusion [14, 15]. The separated flow model is therefore adopted in this thesis as a basis for constructing the two-phase flow model.

The pressure drop of a two-phase flow generally consists of three components: frictional, accelerational, and gravitational change.

$$\left. \frac{dP}{dz} \right|_{tot} = \left. \frac{dP}{dz} \right|_{fric} + \left. \frac{dP}{dz} \right|_{acc} + \left. \frac{dP}{dz} \right|_{grav} \quad (2.1)$$

The heat sink is level in this project so the pressure drop due to the effect of gravity is ignored. The frictional component of the two-phase pressure drop is expressed as

$$\left. \frac{dP}{dz} \right|_{fric} = \phi_{lo}^2 \left. \frac{dP}{dz} \right|_{1\phi} = \frac{2\phi_{lo}^2 f_{lo} G^2 v_l}{D_h} = \frac{2\phi_l^2 f_l G^2 v_l (1-x)^2}{D_h} \quad (2.2)$$

or the product of the two-phase multiplier, ϕ_{lo}^2 , and the single-phase pressure drop.

The single-phase pressure drop is calculated assuming all of the flow is in the liquid phase and is a function of the mass flux, G , liquid specific volume, v_l , hydraulic diameter, D_h , the friction factor, f_l (calculated as if the mixture flows as liquid), and

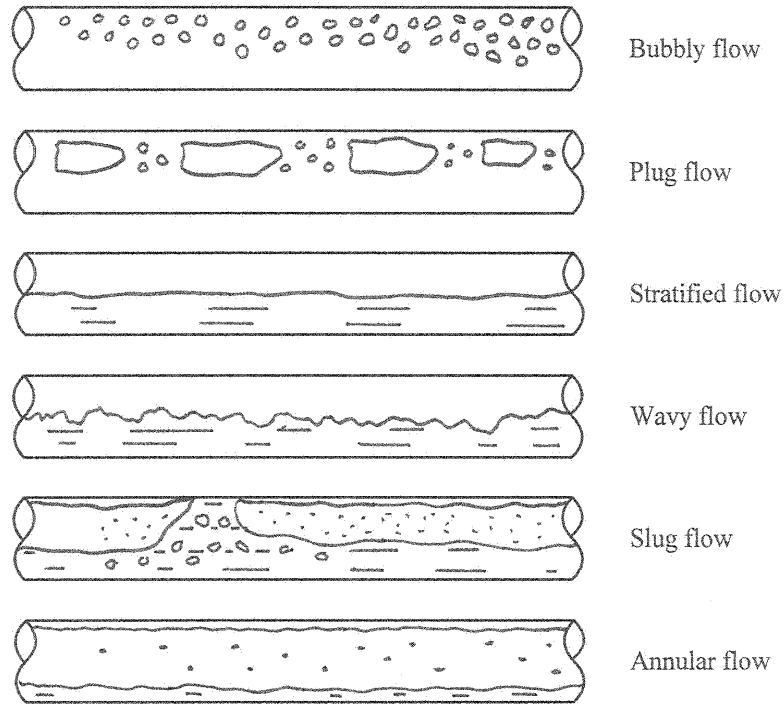


Figure 2.1: Typical two-phase flow patterns in horizontal channels similar to that found in [29].

the quality, x . The single-phase friction factor correlations are used based on the liquid Reynold's number, Re_l , which is defined as

$$Re_l = \frac{GD_h(1-x)}{\mu_l} \quad (2.3)$$

Curves for the two-phase multiplier were developed by Lockhart and Martinelli [30] as a function of X^2 , known as the Lockhart-Martinelli parameter. They did not provide a closed form expression, but Chisholm [31, 32] approximated the curves provided in [30] by developing an analytic expression

$$\phi_l^2 = 1 + \frac{C_{LM}}{X} + \frac{1}{X^2} \quad (2.4)$$

where C_{LM} is the phase interaction parameter. The phase interaction parameter is a constant dependent upon the flow regimes of the liquid and vapor phases. For example, the liquid phase may be a laminar flow while the vapor phase is turbulent. More documentation on this frictional pressure drop model can be found in any two-phase flow book, including Butterworth and Hewitt [33].

Most separated flow models define the Lockhart-Martinelli parameter, X^2 , as the ratio of the pressure drop due to the liquid phase to the pressure drop due to the vapor phase. Mathematically, this parameter is expressed as

$$X^2 = \left(\frac{1-x}{x} \right) \left(\frac{\mu_l}{\mu_v} \right) \left(\frac{v_l}{v_v} \right) \quad (2.5)$$

where x , μ , and v represent the thermodynamic quality, the dynamic viscosity, and the specific volume, respectively, and the subscripts l and v represent liquid and vapor phase, respectively [12].

Several investigations [12, 34-36] have examined the frictional pressure drop through minichannels and microchannels with gas-liquid and vapor-liquid flows. The one dimensional separated flow model was found to correlate well with their data by modifying the phase interaction parameter, C_{LM} . Four examples of phase interaction correlations are given in Table 2.1. Chisholm [34] initially approximated the phase interaction factor for laminar liquid and laminar vapor two-phase flows as a constant. Lee and Lee [35] studied air-water flows through minichannels and proposed a correlation for the phase interaction parameter that includes effects due to surface tension, liquid viscosity, inertia, body forces, and hydraulic diameter. Mishima and Hibiki [36] investigated air-water flows in circular minichannels and developed a

Table 2.1: Phase interaction parameter correlations.

Source	Correlation	Eq.
Lockhart-Martinelli (laminar liquid-laminar vapor) [30,34]	$C_{LM} = 5$	(2.6)
Lee and Lee [35]	$C_{LM} = A\varphi^{-1.317}\psi^{0.719}\text{Re}_{lo}^{0.557}$ $\varphi = \frac{\mu_l^2}{\rho_l\sigma D_h}; \psi = \frac{\mu_l j}{\sigma}; A = 6.933 \times 10^{-8}$	(2.7)
Mishima and Hibiki [36]	$C_{LM} = 21(1 - e^{-319D_h})$	(2.8)
Qu and Mudawar [12]	$C_{LM} = 21(1 - e^{-319D_h})(0.00418G + 0.0613)$	(2.9)

correlation for the phase interaction parameter that is only a function of the channel hydraulic diameter. Qu and Mudawar [12] compared experimental data to predictions using several phase interaction parameter models and reported the specific correlations used by each model. The best fit was achieved with the Mishima and Hibiki correlation [36]; however, Qu and Mudawar [12] modified this correlation to also include the effect of mass flux through the channel.

The acceleration pressure gradient in a constant area channel is expressed as

$$\left. \frac{dP}{dz} \right|_{acc} = G^2 \frac{d}{dz} \left(\frac{x^2 v_v}{\alpha} + \frac{(1-x)^2 v_l}{(1-\alpha)} \right) \quad (2.10)$$

where α is the actual void fraction. For homogenous flows, the homogenous void fraction, denoted as β_v , is used rather than the actual void fraction. Table 2.2 provides a couple of void fraction correlations. Armand [37] and Zivi [38] developed void

Table 2.2: Void fraction correlations.

Source	Formula	Eq.
homogenous [28]	$\beta_v = \frac{xv_v}{\bar{v}}$	(2.11)
Armand [35]	$\alpha = 0.833\beta_v$	(2.12)
Zivi [36]	$\alpha = \frac{1}{1 + \left(\frac{1-x}{x} \right) \left(\frac{v_l}{v_v} \right)^{2/3}}$	(2.13)

fraction models for separated flows in minichannels. The correlation developed by Armand is based on the homogeneous void fraction, whereas that of Zivi is a function of quality and density of each phase. Zhao and Bi [39] and Chung and Kawaji [40] show that the Armand correlation matches well with experimental data for channels having a hydraulic diameter larger than 250 μm . However, the more accurate two-phase pressure-drop separated-flow models compared by Qu and Mudawar [12] used the Zivi [38] void fraction correlation.

Daniels et al. [16] extended the one-dimensional model developed by Pence [9] to predict the pressure drop and bulk fluid temperature for two-phase flows in microscale fractal-like branching flow networks. The extended model accounted for variable flow properties and two-phase flow conditions. The details of the bifurcation at each branch were not included, but it was assumed that the flow instantly split from the larger channel into two smaller channels. Hydrodynamic and thermal redevelopment was assumed in the model at each bifurcation.

3 PREDICTIVE MODEL DEVELOPMENT

A theoretical model is developed to predict the pressure drop characteristics and vapor extraction of the microscale heat sink utilizing local vapor extraction. The model is developed using equations and correlations derived for incompressible, laminar, Newtonian liquid flows in microchannels. The relevant equations and correlations used to model the performance of the microscale heat sink are first identified. Using these relationships and a control volume numerical approach, a predictive model was programmed in MATLAB[®].

3.1 Governing Equations and Correlations

Subcooled, deionized and degassed water is supplied to the heat sink fluid and it is assumed that the water remains a single-phase liquid until it reaches saturation conditions based on the local pressure and temperature. The flow then transitions into a saturated two-phase mixture immediately downstream from the location of zero quality. The predicted heat sink pressure drop can be expressed as

$$\Delta P_{pred} = \Delta P_{1\phi,hd} + \Delta P_{1\phi,fd} + \Delta P_{2\phi} \quad (3.1)$$

where $\Delta P_{1\phi,hd}$ and $\Delta P_{1\phi,fd}$ denote the pressure drops in the single-phase hydrodynamically developing and fully developed regions, and $\Delta P_{2\phi}$ is the pressure drop in the two-phase region. Hydrodynamic redevelopment is assumed at each bifurcation.

3.1.1 Single-phase Pressure Drop

The inlet water enters the microscale heat sink as a single-phase liquid and the pressure drop in this single-phase region can be associated with two sub-regions: the

fully-developed and developing hydrodynamic regions. As flow enters an internal duct, the velocity profile develops in the streamwise direction until it reaches the fully-developed Hagen-Poiseuille velocity profile. The length of the hydrodynamic developing region, L_{hd} , is evaluated as

$$L_{hd} = K_{hd} \text{Re} D_h \quad (3.2)$$

where K_{hd} is the hydrodynamic developing length coefficient provided in Table 41 of Shah and London [41], Re is the Reynold's number of the flow and D_h is the hydraulic diameter. The value of the K_{hd} is dependent on channel geometry and is given in Table 3.1.

The pressure drop in the developed region is calculated using

$$\Delta P_{1\phi,fd} = \frac{2f\rho V^2 L_{1\phi,fd}}{D_h} \quad (3.3)$$

where f is the Fanning friction factor and $L_{1\phi,fd}$ is the length of the developed region or L_{hd} in the single-phase region. The friction factor depends on flow conditions, channel geometry, and channel wall surface conditions. For laminar flow in rectangular channels, Shah and London [41] provide the following relationship

$$f \text{Re} = 24 \left(1 - 1.3553\alpha_{ch} + 1.9467\alpha_{ch}^2 - 1.7012\alpha_{ch}^3 + 0.9564\alpha_{ch}^4 - 0.2537\alpha_{ch}^5 \right) \quad (3.4)$$

where α_{ch} is the aspect ratio of the channel. The aspect ratio is calculated as the ratio of the width to the height of the channel or vice-versa such that the ratio ranges between 0 and 1.

To account for the developing region, the pressure drop equation, Eq. (3.3), is modified by replacing f by the apparent friction factor, f_{app} . The apparent friction

Table 3.1: Tabulated values for the constants used in Eqs. (3.2) and (3.6) [41].

α	K_{hd}	$K(\infty)$	C
0.00	--	0.674	0.000029
0.20	0.080	0.931	0.000076
0.25	0.075	--	--
0.50	0.085	1.28	0.00021
1.00	0.090	1.43	0.00029

factor accounts for the greater friction in the developing region due to the greater velocity gradient and wall shear stress at the channel walls. The pressure drop in the developing region is thus expressed as:

$$\Delta P_{1\phi,hd} = \frac{2f_{app}\rho V^2 L_{1\phi,hd}}{D_h} \quad (3.5)$$

Shah and London [41] proposed the following equation for the apparent friction factor

$$f_{app} \text{Re} = \frac{3.44}{\sqrt{x^+}} + \frac{f \text{Re} + \frac{K(\infty)}{4x^+} - \frac{3.44}{\sqrt{x^+}}}{1 + \frac{C}{(x^+)^2}} \quad (3.6)$$

where x^+ is the non-dimensional entrance region length given by

$$x^+ = \frac{z/D_h}{\text{Re}}, \quad (3.7)$$

$K(\infty)$ is the incremental pressure defect and C is a constant dependent on the channel geometry. The values for $K(\infty)$ and C are interpolated from tabulated values in Shah and London [41] and are given in Table 3.1. It should be noted that apparent friction factor is defined as the average value of the local friction factor over the length z or in other words:

$$f_{app}(z) = \frac{1}{z} \int_0^z f d\hat{z} \quad (3.8)$$

where $d\hat{z}$ represents the differential distance along the flow. Taking the derivative of both sides and using the product rule of differentiation, the local friction factor is:

$$f(z) = f_{app}(z) + z \left. \frac{df_{app}}{d\hat{z}} \right|_z \quad (3.9)$$

where

$$\frac{df_{app}}{d\hat{z}} = \frac{1}{D_h \text{Re}^2} \left[\frac{-3.44}{2(x^+)^{3/2}} + \frac{\frac{2f \text{Re} C}{(x^+)^3} - \frac{K(\infty) \left(1 - \frac{C}{(x^+)^2}\right)}{4(x^+)^2} + \frac{3.44 \left(1 - \frac{3C}{(x^+)^2}\right)}{2(x^+)^{3/2}}}{\left(1 + \frac{C}{(x^+)^2}\right)} \right] \quad (3.10)$$

3.1.2 Energy Balance

As mentioned earlier, the transition from single-phase to two-phase flow occurs when the thermodynamic quality is equal to zero. It can also be identified when the bulk temperature of the fluid flow is equal to the saturation temperature of the fluid, which is calculated as a function of the local pressure of the flow. An energy balance can be performed to calculate the bulk fluid temperature in the single-phase region:

$$T(z) = T_{in} + \frac{\dot{Q}_{frac}'' A_z}{\dot{m}_z c_p} \quad (3.11)$$

where $T(z)$ and T_{in} are the bulk temperature a streamwise distance z from the entrance and the inlet bulk temperature, respectively, \dot{Q}_{frac}'' is the flux of heat transferred to the flow, A_z is the surface wall area across which heat transfer occurs from the inlet to z ,

\dot{m}_z is the mass flow rate of the fluid, and c_p is the specific heat capacity of the fluid.

Once the flow becomes saturated, the energy balance is modified to account for the local extraction of vapor from a control volume as defined in Fig. 3.1:

$$\dot{Q}_{CV} = (\dot{m}_{vap} i_{vap} + \dot{m}_{out} i_{out} - \dot{m}_{in} i_{in})_{CV} \quad (3.12)$$

where \dot{Q}_{CV} is the rate of heat transferred to the control volume, i represents the enthalpy of the flow crossing the control volume boundary and the subscript *vap* refers to the extracted vapor. Conservation of mass for a control volume dictates that

$$\dot{m}_{in} = \dot{m}_{out} + \dot{m}_{vap} \quad (3.13)$$

3.1.3 Flow through Porous Media

The flow rate of the extracted vapor through the porous membranes and the porous aluminum is governed by Darcy's law. The fictitious flow velocity or Darcy velocity, \bar{V}_{vap} , is defined as the ratio of the volumetric flow rate over the porous media

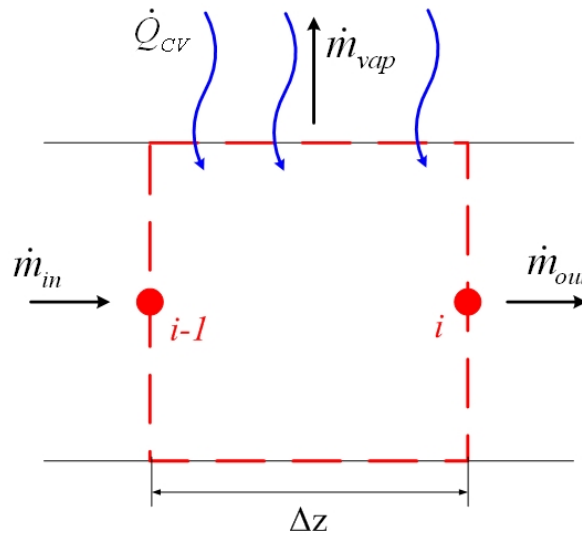


Figure 3.1: Schematic of the discretization scheme employed in the predictive model.

cross sectional area. Details of the microscopic flow are avoided and an averaged macroscopic perspective over the cross sectional area is used to quantify flow through porous media. The complete form of Darcy's law is

$$\bar{V}_{vap} = - \left(\frac{\kappa}{\mu_{vap}} \right) (\rho g \nabla y + \nabla P) \quad (3.14)$$

where κ is the specific permeability of the media with m^2 units, μ_{vap} is the dynamic viscosity of the extracted vapor, ∇y represents the change in elevation and ∇P represents the pressure difference across the porous media [42]. Through an order of magnitude analysis for the flow situation in the experimental setup where the elevation change is on the order of millimeters and the pressure difference is on the order of kilopascals, the pressure difference term is found to be ninth order and the change in elevation term is zero order. Based upon this analysis, the change in elevation term is neglected in computing the Darcy velocity, in which case Eq. (3.14) reduces to:

$$\bar{V}_{vap} = \left(\frac{\kappa}{\mu_{vap}} \right) \frac{\Delta P_{vap}}{L} \quad (3.15)$$

where ΔP_{vap} is the pressure difference across the porous medium and L is the thickness of the porous medium. The dynamic viscosity is evaluated at the average temperature of the vapor in the control volume as it is extracted.

The hydrophobic membranes and porous aluminum can be thought of as resistors in series allowing Eq. (3.15) to be rewritten in terms of the extracted vapor mass flow rate:

$$\dot{m}_{vap} = \Delta P_{vap} \frac{A_{cs}}{\nu_{vap}} \left(\frac{\kappa_{mem}}{L_{mem}} + \frac{\kappa_{al}}{L_{al}} \right) \quad (3.16)$$

where A_{cs} is the vapor extraction cross-sectional area, ν_{vap} is the kinematic viscosity of the vapor, and the subscripts *mem* and *al* refer to the porous membranes and the porous aluminum, respectively. The cross-sectional area, A_{cs} , is calculated as the top planar area of the microchannels through which vapor could be extracted and not as the open pore area in this region. The inner radius of this area is the length of the single-phase region and the outer radius is the periphery of the fractal disk. The specific permeability values for the hydrophobic membranes and porous aluminum are given by the manufacturers as 1.37×10^{-14} and $3.20 \times 10^{-13} \text{ m}^2$, respectively.

3.1.4 Two-phase Pressure Drop

As discussed in the literature review (§ 2.6.2 Two-phase Models), the pressure drop of the two-phase flow in this project can be divided into a frictional and accelerational component:

$$\left. \frac{dP}{dz} \right|_{2\phi} = \left. \frac{dP}{dz} \right|_{2\phi,fric} + \left. \frac{dP}{dz} \right|_{2\phi,acc} \quad (3.17)$$

The frictional component of the two-phase pressure drop is the product of the two-phase multiplier, ϕ_{lo}^2 , and the single-phase pressure drop. The single-phase pressure drop is calculated using Eq. (3.3) if the two-phase flow is fully developed or Eq. (3.5) if the flow is developing. Qu and Mudawar [12] compared the accuracy of eleven flow models for predicting two-phase pressure drop experimentally measured in their heat sink. Based on these recommendations, the following correlation for the two-phase multiplier is used:

$$\phi_l^2 = 1 + \frac{C_{LM}}{X} + \frac{1}{X^2} \quad (3.18)$$

where C_{LM} is the phase interaction parameter and X^2 is the Lockhart-Martinelli parameter. The correlation used for the phase interaction parameter is given by Qu and Mudawar [12]:

$$C_{LM} = 21(1 - e^{-319D_h})(0.00418G + 0.0613) \quad (3.19)$$

The Lockhart-Martinelli parameter is given by the following relationship:

$$X^2 = \left(\frac{1-x}{x} \right) \left(\frac{\mu_l}{\mu_v} \right) \left(\frac{v_l}{v_v} \right) \quad (3.20)$$

where x is the local quality of the flow. The two-phase pressure drop due to friction is

$$\Delta P_{2\phi,fric} = \frac{2G^2 L_{2\phi}}{D_h} \left[\frac{1}{x_{ex} x_{in}} \int_{x_{in}}^{x_{ex}} \phi_l^2 f_l (1-x)^2 v_l dx \right] \quad (3.21)$$

where ex and in refer to the exit and inlet of the control volume region, respectively.

The two-phase pressure drop due to acceleration is expressed as

$$\Delta P_{2\phi,acc} = G^2 \left[\left(\frac{x^2 v_v}{\alpha} \right)_{ex} - \left(\frac{x^2 v_v}{\alpha} \right)_{in} + \left(\frac{(1-x)^2 v_l}{(1-\alpha)} \right)_{ex} - \left(\frac{(1-x)^2 v_l}{(1-\alpha)} \right)_{in} \right] \quad (3.22)$$

Based on the recommendations of the comparative study by Qu and Mudawar [12], the void fraction correlation proposed by Zivi [38] is used in this predictive model:

$$\alpha = \frac{1}{1 + \left(\frac{1-x}{x} \right) \left(\frac{v_l}{v_v} \right)^{2/3}} \quad (3.23)$$

3.2 Model Setup

A one-dimensional model is developed using the governing equations discussed in the previous sections. The flow path is discretized using a nominal grid spacing (the nominal grid spacing determination is discussed later in this section) and then the pressure drop and energy balance equations are propagated in the streamwise direction. A schematic of the discretization scheme used in the model is showed in Fig. 3.1 where the box represents the control volume region bounded by the nodal points. The inputs required to run the predictive model included the inlet subcooling, inlet flow rate, exit plenum pressure, vapor plenum pressure and the rate of heat transferred to the microchannel flow. The model was generated so that flow geometries for either branching channels or straight channels could easily be integrated into the present model. Conservation of mass and energy relationships are applied to the control volume regions. The static pressure of the flow, the bulk fluid temperature, and the fluid properties are calculated locally at each node.

The grid spacing is represented by the distance Δz . To identify the nominal discretization length, a grid refinement study was performed. The study set out to identify the largest discretization length at which the predictions of the model are not significantly altered by using a smaller discretization length. The nominal step size was identified as 1 micron with less than 0.25% change in the predicted pressure drop values at reduced step sizes with and without local vapor extraction.

Inputs required to run the predictive model are the channel geometry, the exit plenum pressure, the inlet mass flow rate, the energy input, the vapor plenum pressure,

the porous media characteristics and either the inlet temperature or inlet subcooling. The channel geometry includes the length, width and height for straight channels as well as the number of initial branches, the number of branching levels, and the length and hydraulic diameter ratios for branching fractal-like geometries. The porous media characteristics are the specific permeability value and the thickness of the hydrophobic membrane and porous aluminum.

The model predicts pressure, thermodynamic quality, enthalpy, void fraction, density, dynamic viscosity and bulk fluid temperature at each discrete node in the flow network. In the control volume regions bounded by the discretized nodes, the model outputs the average flow rate of extracted vapor as a function of the average local extraction pressure difference which is defined as the difference between the vapor plenum pressure and the average pressure in the control volume. Independent calculations of the two-phase accelerational and frictional pressure drops are averaged from point 1 to point 2 (the inlet and exit of each control volume) to determine the local pressure. Since the exit plenum pressure is specified but the inlet pressure is required in order to march in the streamwise direction, an initial guess is made of the inlet pressure. The predicted exit pressure generated by the model is then compared to the exit plenum pressure provided. If these pressures are not within the tolerance of 5 Pa, the inlet pressure is modified and the model is rerun. If the predicted pressure is greater than the provided pressure, the inlet pressure is reduced by 95% of the difference to prevent oscillations of the predicted pressure about the provided value. The process is repeated until the predicted and specified exit pressures agree within the level of tolerance.

The model was verified against results published for similar single-phase and two-phase models. The model was verified with a difference less than one percent for single-phase pressure drop and bulk fluid temperature profiles using the theoretical results reported by Pence [9], which were validated by Alharbi et al. [26, 27]. Model predictions of two-phase flow without local vapor extraction were compared to the theoretical results of straight, parallel microchannels in Qu and Mudawar [12] and of branching, fractal-like microchannels in Daniels et al. [16]. The model predictions matched those of Daniels et al. [16] with a difference less than 0.5%. Model predictions matched well those of Qu and Mudawar [12]; however it is not possible to quantify the difference in the predictions due to information concerning the size of the inlet and exit plenums missing in their publication.

The predictive model is used to investigate the vapor phase extraction feasibility and characteristics and the resultant reduction in the two-phase network pressure drop. Possible important trends and effects are identified from the predictive model and experimental data and are further investigated using the predictive model. The effect of local vapor extraction added in the current study is validated against experimental data collected during this project. The predictive model results and validation are presented in the Results and Discussion section (§6.1 & §6.2) of this thesis.

4 EXPERIMENTAL APPARATUS AND PROCEDURE

The experimental apparatus was assembled and tested in the Microscale Transport Enhancement Lab at Oregon State University. A schematic, cross-section representation of the heat sink is detailed in Fig. 4.1. A fractal-like microchannel network and porous membranes (bottom of the schematic in Fig. 4.1) were combined to simulate the microscale flow network of a heat sink. Subcooled water enters the center of the fractal network and flows radially toward the periphery of the disk. Heat is supplied by the porous aluminum heater using a coiled resistance wire (top of the schematic in Fig. 4.1). Vapor is extracted locally from the flow network through the porous membranes and block heater. The remaining liquid, or two-phase mixture if not all of the vapor is extracted, discharges at the periphery of the heat sink. The heat sink is enclosed by a test manifold, which is plumbed into an experimental flow loop. The test manifold and experimental flow loop facilitated performance characterization of the experimental microscale heat sink.

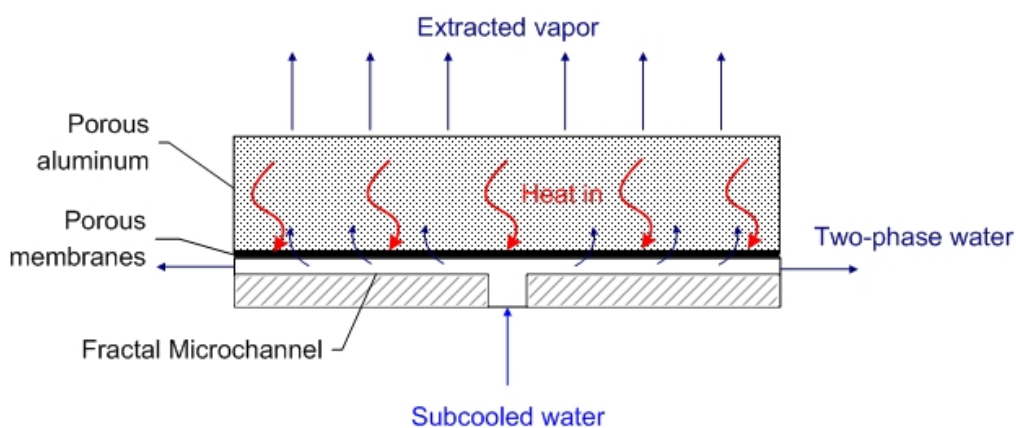


Figure 4.1: Schematic of the microscale heat sink comprised of a fractal network, porous membrane and porous aluminum heater.

4.1 Fractal Network

The central piece of the microscale heat sink and experimental evaluation is the fractal-like branching microchannel network. The pattern of the fractal network is shown in Fig. 4.2 and a more detailed schematic of a set of branching levels is shown in Fig. 4.3. Its design is characterized by the following scaling laws [9]:

$$\beta = \frac{D_{h,k+1}}{D_{h,k}} = n^{-1/AC} \quad (4.1)$$

$$\gamma = \frac{L_{k+1}}{L_k} = n^{-1/D} \quad (4.2)$$

$$N_M = N_0 n^M \quad (4.3)$$

The symbols γ and β represent the branching length and hydraulic diameter ratios, respectively, M is the total number of branching levels not including the 0th level, n is the number of branches into which a single channel splits. D is the Euclidean dimension, $D_{h,k}$ and L_k are, respectively, the hydraulic diameter and length of the

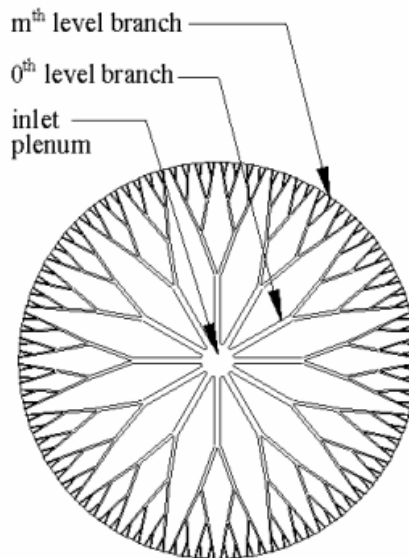


Figure 4.2: The microchannel fractal element used in the current study [9].

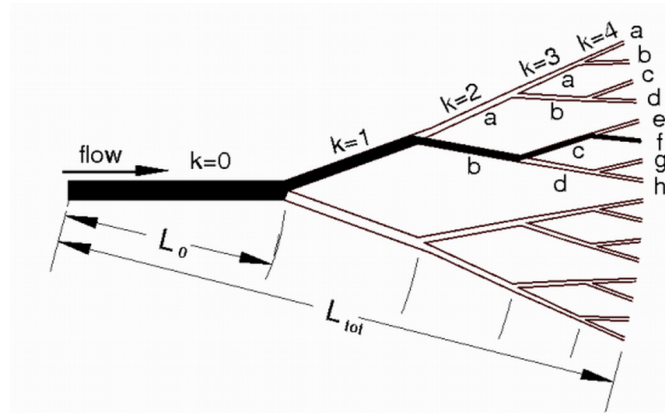


Figure 4.3: Representation of a subset of the fractal network showing the different branch levels [27].

channel in level k , and N_0 is the number of 0th-level channels. The index k numbers from zero to M . For the two-dimensional heat sink used in this study, the Euclidean dimension, D , is two, the number of branches, n , is two, and the constant in Eq (4.1), AC , is equal to three. The channel depth remains constant throughout the fractal network and the number of 0th-level channels, N_0 , is twelve. The fractal network used has four branching levels, M . With these values, the hydraulic diameter and length ratios are 0.7937 and 0.7071, respectively. Given a fixed channel depth, the hydraulic diameter is given by the following relationship:

$$D_{h,k} = \frac{4(H_k w_k)}{2(H_k + w_k)} = \frac{4(H w_k)}{2(H + w_k)} \quad (4.4)$$

where w_k is the channel width in level k . The channel height, H_k , remains constant and can be represented simply by H . The channel widths can be determined from

$$w_k = \frac{w_{k+1} H}{\beta(w_{k+1} + H) - w_{k+1}} \quad (4.5)$$

starting with the known terminal channel width. The terminal channel length is determined by using a specified total channel length and the relationship:

$$L_M = \frac{L_{tot}}{\sum_{i=0}^M (1/\gamma^i)} \quad (4.6)$$

The total channel length is defined as the sum of the channel length of each branching level. Lower-level branching lengths are subsequently determined using Eq. (4.2) and are graphically represented in Fig. 4.3 as the distance between each bifurcation.

Table 4.1 details the specifications of the fractal network which has a total channel length of 17.5 mm (0.689 in). The overall diameter of the heat sink is 3.556 cm (1.4 in).

The fractal microchannel network used in this project was created by machining the fractal pattern in a stainless steel laminate 36 mm in diameter and 250 μm thick using a micromachining laser [43]. The machining laser utilized a green-light laser having a wavelength of 432 nm. The diameter of the kerf, which is the groove created by the laser, was approximately 40 μm . The operating parameters of the laser were set at a power level of 3 W, a frequency of 3 kHz and a bite size of 3 μm . After the laser cut the fractal pattern, the channel blanks or patterns were removed. The laminate layer with the flow network and supporting bridges are shown in Fig. 4.4. Supporting bridges are needed to preserve the geometry and alignment of the channels, especially the terminal channels, during the diffusion bonding process.

Table 4.1: Channel dimensions of the fractal network (see Figs. 4.2 and 4.3).

k	H_k (mm)	w_k (mm)	$D_{h,k}$ (mm)	L_k (mm)
0	0.250	0.643	0.360	6.23
1	0.250	0.333	0.286	4.40
2	0.250	0.204	0.227	3.11
3	0.250	0.141	0.180	2.20
4	0.250	0.100	0.143	1.56
				<i>Total:</i> 17.5

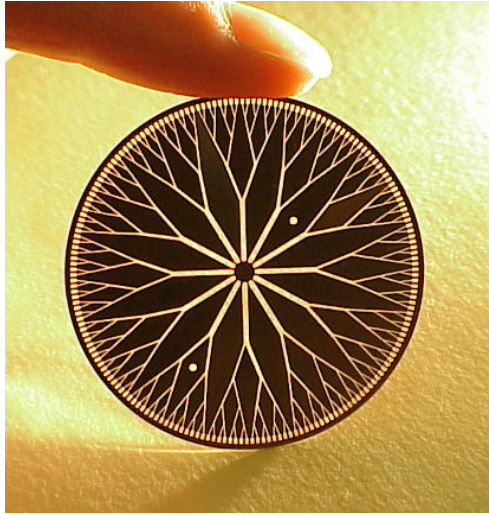


Figure 4.4: Image of the top laminate piece with supporting bridges before being diffusion bonded to the bottom laminate [43].

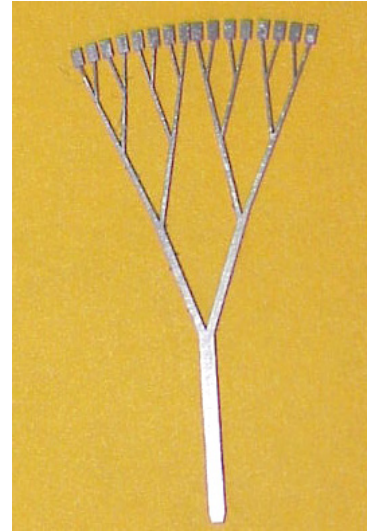


Figure 4.5: Image of a channel blank removed from the top laminate after cutting the fractal pattern on the micromachining laser [43].

An example channel pattern removed from the top laminate is shown in Fig. 4.5. The cut laminate is then stacked on a bottom laminate in an alignment chuck. The two pieces are aligned with alignment pins. A hole is placed in the center of the bottom laminate to allow fluid to enter the microchannel network from the bottom. A vacuum hot press is then used to diffusion bond the laminate pieces together. The last step removes the supporting bridges to allow fluid to exit at the periphery of the disk using the same laser.

Since the manufacture of this fractal network, the geometry pattern and fabrication process of the fractal networks have changed. For a constant channel depth, as required by the fabrication process mentioned, a fixed hydraulic diameter ratio can result in an infinite channel width for the lower order branching levels [10]. A width ratio is now used to avoid this problem and has been determined using an

optimization process similar to that in Bejan [44]. The branching of the fractal network used in the current study is asymmetric as shown in Fig. 4.3. After the investigations of Alharbi et al. [27], symmetric branching was employed in the geometry of the more recent networks. Other fractal networks have been manufactured using chemical etching and micromachining methods. The fabrication processes were changed to allow for greater terminal channel width, to improve the geometric layout accuracy, and to simplify the fabrication process. The old pattern is used in the current study because the recent networks were not available when the current study began.

As shown in Figs. 4.1, porous membranes are placed between the fractal network and the porous aluminum heater block to enclose the open channel paths of the fractal network and form the top surface of the microchannel. The membranes are composed of a Nylon membrane material on a Nylon support system from GE Osmonics. Vapor molecules can pass through the hydrophobic porous membranes, but liquid molecules cannot. Due to small surface imperfections of the porous aluminum and fractal disk, two membranes instead of one are used to provide a sufficient seal between the fractal and heater block to prevent leaks. The compression of the test manifold reduced the thickness of the membranes and caused them to partially fill the microchannels. The total thickness of the two membranes was measured to be $140\ \mu\text{m}$ by digital calipers with a combined variation and uncertainty of approximately $15\ \mu\text{m}$. From the pattern left in the membranes after being removed from the test manifold, it was measured by calipers that the membranes reduced the channel height by $50\ \mu\text{m}$ to $200\ \mu\text{m}$ with an uncertainty of approximately $15\ \mu\text{m}$. The

combined effects of compression of the membranes and elevated surface temperature found at the stainless steel in between the microchannels caused the membranes to slowly degrade. Due to this degradation, the porous membranes were replaced approximately every six hours of data collection to prevent complete degradation of the membranes.

4.2 Test Manifold

The main purpose of the test manifold was to house the microscale heat sink, provide flow at the heat sink inlet, collect the extracted vapor and facilitate

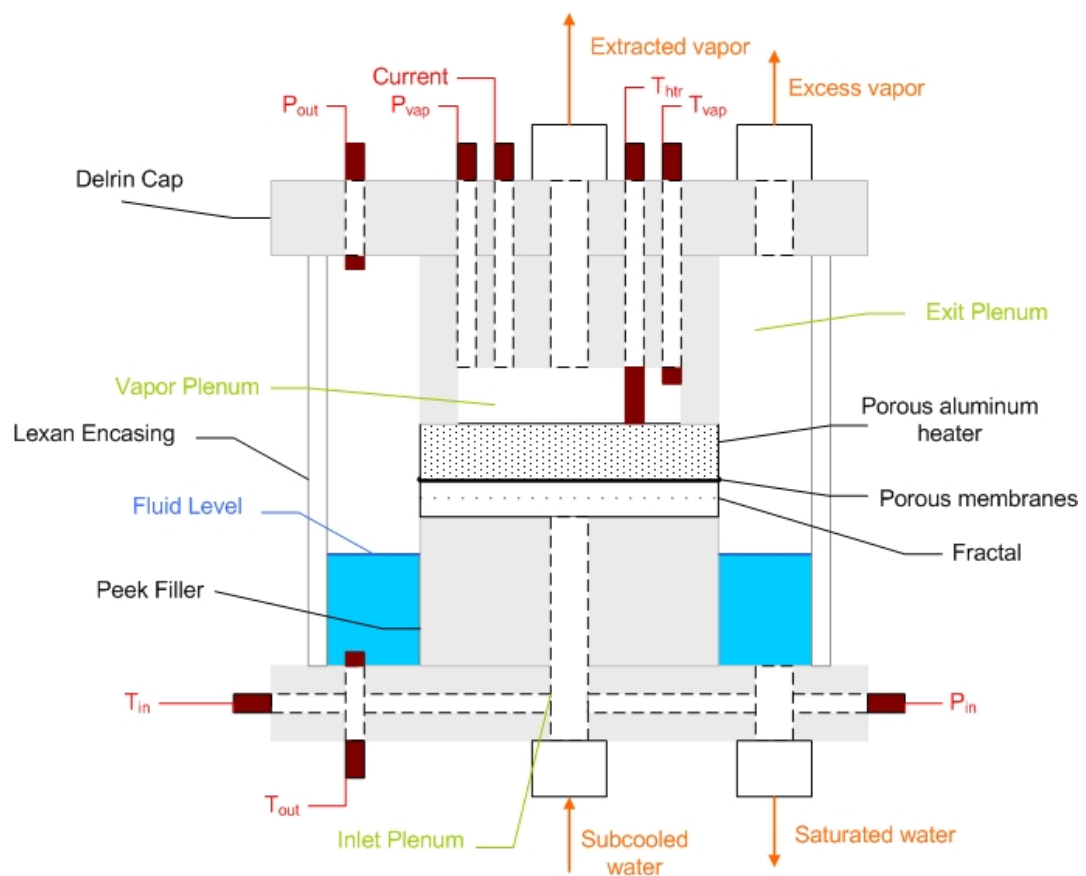


Figure 4.6: Detailed schematic of the test manifold.

experimental analysis of heat sink pressure drop performance. A detailed schematic of the test manifold is given in Fig. 4.6. Pre-heated, deionized, degassed water within a few degrees of saturation was introduced at the bottom of the manifold. After passing through the inlet plenum of the test manifold, the flow entered the microchannels at the center of the disk and traveled radially toward the periphery of the heat sink. The supplied heat boiled the subcooled flow. Vapor was locally extracted through the hydrophobic porous membranes and porous aluminum into a pressure regulated vapor plenum. The remaining two-phase flow, if local extraction was not maximized, exited the fractal network into the exit plenum where the excess vapor exited through the top cap and the saturated liquid through the bottom cap. A constant liquid level in the exit plenum was important to ensure steady state experimental conditions (see the Operating Procedure §4.6 and Data Analysis and Reduction §5.1). Detail drawings of the test manifold parts are provided in Appendix A and images of the assembled manifold are provided in Appendix B.

4.2.1 Design

The material choice for the test manifold components was dictated by temperature constraints, functional requirements, and cost. Besides the fractal piece and the porous aluminum heater, the main components of the manifold are made from plastics. Several characteristics of plastics made them desirable in this application, including: relatively small thermal conductivity values to thermally isolate the heat sink, large ultimate tensile strength values to withstand deformation, and low wear factors to endure continuous and repetitive testing and use. PEEKTM plastic was

chosen for the top and bottom fillers adjacent to the microscale heat sink because of its low thermal conductivity value, relatively large ultimate tensile strength value (comparable to low grade metals), and exceptionally low wear factor value. These characteristics made PEEKTM the optimal material, but due to the high cost of PEEKTM, Delrin[®], which has comparable physical properties to PEEKTM, was used for the top and bottom caps. The encasing is made of Lexan[®] to allow visibility of the exit plenum and the fluid level. The flow and instrument fittings are either stainless steel, PVDF (Kynar[®]) or Delrin[®] to withstand the elevated temperatures. Silicone o-rings are used at all interfaces between the manifold components and heat sink.

The porous aluminum heater added energy to boil the water inside the microchannels. Coiled nickel-chromium alloy resistance heating wire, common in many high-temperature applications, is embedded in the porous aluminum. For this project, Nichrome-60 wire containing sixty percent nickel and sixteen percent chromium with a wire diameter of 0.25 mm (30 AWG) and a coil outside diameter of 1.6 mm (1/16") was selected. The wire was embedded in a spiral path to maximize wire length and provide a relatively uniform heat flux to the microchannel flow while still allowing for vapor extraction. Figure 3.A in Appendix A shows the block heater apparatus with the embedded groove. The radius of the spiral groove path was set to leave exposed aluminum in between the grooves to provide sufficient area for the extracted vapor to enter the vapor plenum. The resistance wire is potted in the groove using Omegabond[®] 600, a high-temperature, non-porous chemical set cement. The cement surrounds the coiled wire to maximize heat transfer to the porous aluminum and to electrically insulate the coiled wire. The resistance of the potted heater wire is

measured to be approximately 27.5Ω with slightly greater resistance at elevated temperatures. Lead wires were soldered to the potted resistance wire and exit the test manifold through the vapor plenum through finger-tight fittings sealed by ferrules surrounding the lead wires.

The test manifold was examined for leaks at each fitting and the interfaces between the heat sink, porous membrane and porous aluminum. Air was compressed to 4 bar into isolated regions of the manifold with the bubbling of soapy water around the exterior of the fitting or at the interface signifying any leaks. The fittings were sufficiently tightened to prevent any leaks. The outer edge of the porous aluminum was coated with high-temperature paint to prevent vapor transport to the exit plenum and to prevent drawing excess vapor from the exit plenum into the vapor plenum. A visual inspection of the periphery of the network during operation verified that liquid remains in the microchannels and does not travel in any voids between the fractal and porous membranes.

4.2.2 Instrumentation

The placement of the instrumentation in the manifold is detailed in Fig. 4.6. The temperature and pressure of the inlet flow were measured at the inlet plenum 3.5 cm directly upstream of the fractal disk. Similarly, the extracted vapor temperature and pressure were obtained in the vapor plenum. The temperature of the porous aluminum is also monitored to ensure that the thermal operating limits of the porous aluminum and porous membranes are not surpassed, which are 210 and 180 °C, respectively. The pressure of the exit flow is obtained in the exit plenum using a

differential pressure transducer between the inlet and exit plenums and the absolute pressure transducer in the inlet plenum. The exit liquid temperature is measured in the exit plenum. The temperatures of the inlet, extracted vapor and exit liquid flows were measured with 1.6 mm (1/16") diameter, grounded, shielded, K-type thermocouple temperature probes. An exposed junction, insulated, T-type thermocouple monitors the top surface temperature of the heater in the exit plenum. Like the resistance wire, this thermocouple is potted to the surface of the heater with Omegabond[®] 600 cement. The inlet and vapor pressure measurements were obtained with general purpose pressure transducers having a 0 – 100 mV output and an absolute range of 0 – 2.07 bar (0 – 30 psi). A differential pressure transducer with a 4 – 20 mA output and a gauge pressure range of 0 – 14 kPa (0 – 2 psi) is used to measure the pressure drop across the fractal network. The uncertainty of each measurement device is reported in Appendix D.

4.3 Flow Loop

The experimental flow loop provided preheated water to the test manifold and removed the extracted vapor, exit liquid and excess vapor. A schematic of the open-loop test facility is shown in Fig. 4.7. The forty-gallon bladder tank is filled by pumping distilled deionized water in from the carboy water supply. Once the bladder tank is sufficiently filled, the shut-off valve before the bladder tank is closed. The bladder tank is pressurized by the surge tank, which ensured that fluctuations in the building air supply have a negligible effect on the flow rate and a constant air pressure is supplied to the bladder tank. Water passed from the bladder tank through a

15 micron filter to rid the flow of impurities greater than the filter pore size. The inlet fluid flow rate is regulated by a needle valve in the inlet line and is measured with a Coriolis mass flow meter. The fluid is preheated in a hot oil reservoir to a few degrees below saturation. Analysis of the hot oil reservoir provided in Appendix F indicates that the flow leaves the reservoir at the oil reservoir temperature. Cavitation of the

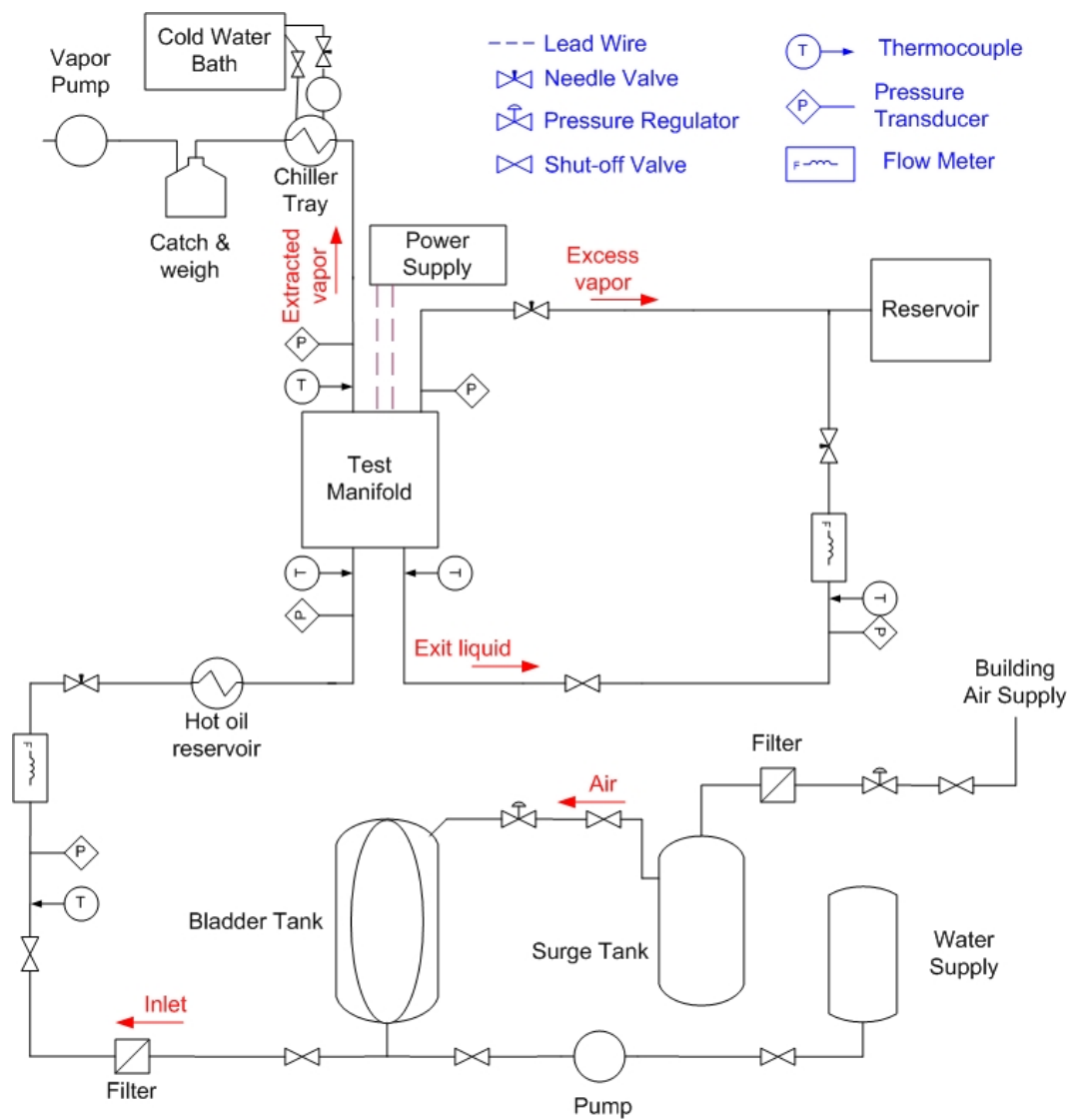


Figure 4.7: Schematic representing the layout of the experimental flow loop for the current study.

inlet flow is avoided by setting the oil reservoir temperature just below the saturation temperature of the flow. Heat loss from the preheated flow is minimized by and the saturation temperature is essentially maintained by heat supplied to the line between the hot oil reservoir and the manifold using a heater rope. As mentioned previously, the temperature, pressure and subcooling of the inlet flow were measured in the inlet plenum of the manifold. A power supply with an output range of zero to one amp provided current to the coiled resistance heater.

A vapor vacuum pump created the needed pressure differential to extract vapor from the two-phase flow in the microchannels through the porous media. The temperature and pressure of the extracted vapor were measured in the vapor plenum of the manifold (see Fig. 4.6). A cold water bath supplied water to a chiller tray that condensed the extracted vapor. The vapor was then collected in a glass jar. It was critical that the extracted vapor completely condensed in the chiller tray to avoid being lost to the surrounding environment. A lack of condensed water in the tubing downstream of the catch jar visually verified that water vapor completely condensed in the cold water bath. A catch jar sat on a scale to measure the flow rate by monitoring the collected mass reading as a function of time. The vacuum pump was connected to the top of the catch jar, but did not draw the condensed fluid. Gasket maker material was applied around the two fittings in the jar lid and the lid itself to seal the catch jar and prevent pressure losses between the vapor pump and vapor plenum of the test manifold.

The two-phase fluid that passed through the microchannels was driven by the pressure difference between the inlet and exit plenums, which was near ambient

pressure. Needle valves regulated the exit liquid and excess vapor flow rates. The temperature and pressure of the exit liquid was measured in the exit plenum of the manifold. The exit vapor temperature was not measured because of data acquisition limitations. A downstream Coriolis mass flow meter measured the liquid flow rate exiting the manifold. The excess vapor flow rate was not measured but is easily determined from a conservation of mass evaluation of the other three flow rates. This assessment required the liquid level in the exit plenum to remain steady. The exit liquid and excess vapor streams were collected in a reservoir downstream.

4.4 Test Plan

A test plan was devised to measure pressure drop subjected to local extraction of vapor from the branching, fractal-like microchannel heat sink. The parameters of the study included inlet flow rate, vapor extraction pressure difference, and supplied heat. The exit plenum pressure and inlet subcooling were kept as close as possible to constant throughout the study varying by no more than 2 kPa and 1.5 K, respectively. Pressure drop characteristics were calculated from pressure values in the inlet, vapor and exit plenums of the manifold. Vapor extraction was characterized by the membrane pressure difference and extracted vapor flow rate.

The range of the supplied heat was determined from the thermal limitations of the porous aluminum and porous membranes and the lowest energy input needed to boil the water flow. The maximum operating temperature of the two materials is, respectively, 210 and 180 °C. From the temperature response of the resistance wire, the maximum possible supplied heat was identified as 50 W. However, the maximum

Table 4.2: Summary of independent variables and their respective values.

Independent Variable	Value(s)
ΔT_{sc}	2.5 K
\dot{Q}_{hr}	18 – 30 W
\dot{m}_{in}	8 – 12 g/min
ΔP_{vap}	0 – 55 kPa
P_{ex}	100.7 kPa

input heat was limited to 30 W to ensure that the porous aluminum and membranes did not thermally deteriorate. An energy balance analysis showed that a minimum of 10 W of supplied heat is needed to boil the microchannel flow at the median inlet flow rate; the input heat values were chosen to be 18, 24 and 30 W. An energy balance analysis is used to establish that the inlet flow rate range is 6 – 15 g/min at the supplied heat center point. Inlet flow rates of 8, 10 and 12 g/min are chosen for analysis. Details of the energy analysis are provided in Appendix F. The extraction pressure differential test range is dictated by the operating limits of the vapor pump and is 0 – 55 kPa (0 – 8 psi). The inlet water subcooling was maintained at 2.5 K to ensure that the flow entered in the single-phase regime. The exit plenum pressure was maintained constant throughout the data collection at 100.7 kPa (14.5 psi). Table 4.2 summarizes the independent variables and their respective values and the matrix of test points is given in Table 4.3.

4.5 Data Acquisition

National Instruments LabVIEWTM software was used to monitor, acquire, and store experimental data. The test conditions were monitored and adjusted until steady state conditions were reached.

Table 4.3: Matrix of experimental runs evaluated.

Run Order	Input Heat (W)	Inlet Flow Rate (g/min)	Extraction difference (kPa)	Run Order	Input Heat (W)	Inlet Flow Rate (g/min)	Extraction difference (kPa)
1	18	12	0	24	24	10	42
2	18	12	14	25	24	10	55
3	18	12	28	26	30	10	0
4	18	12	42	27	30	10	14
5	18	12	55	28	30	10	28
6	24	12	0	29	30	10	42
7	24	12	14	30	30	10	55
8	24	12	28	31	18	8	0
9	24	12	42	32	18	8	14
10	24	12	55	33	18	8	28
11	30	12	0	34	18	8	42
12	30	12	14	35	18	8	55
13	30	12	28	36	24	8	0
14	30	12	42	37	24	8	14
15	30	12	55	38	24	8	28
16	18	10	0	39	24	8	42
17	18	10	14	40	24	8	55
18	18	10	28	41	30	8	0
19	18	10	42	42	30	8	14
20	18	10	55	43	30	8	28
21	24	10	0	44	30	8	42
22	24	10	14	45	30	8	55
23	24	10	28				

Data were gathered in repetitions and replications. Repetitions were the number of measurements recorded in each block of time or replication. A replication was completed approximately every fifteen seconds. For example, all analog measurements (temperature and pressure) were recorded at a rate of 1000 Hz for one second, yielding one thousand measurement values for each replication. Approximately seventy five replications were recorded for each experimental run giving a total of 75,000 data points for pooled statistics.

The Coriolis mass flow meters operated in frequency output mode and transmitted a 0.8 V peak-to-peak digital signal. The frequency of the signal is directly proportional to the mass flow rate. To measure the frequency, the data acquisition

board counts the number of pulses during an “open gate” time period. In each replication, one thousand repetitions (pulses per open gate) are recorded for both mass flow meters.

The mass flow rate of the extracted vapor is measured by monitoring the mass change inside the glass catch jar. The jar rests on an ADAM[®] ACBplus-600H portable scale. The mass reading is acquired by LabVIEW[™] via a RS-232 serial bus connection. For each replication (every 15 seconds), one hundred mass readings are acquired and recorded. Simultaneously, a time stamp is recorded in LabVIEW[™]. The time elapsed between replications is used to calculate the extracted vapor mass flow rate.

Raw voltage data were assigned physical units using calibration curve fit equations. Calibration procedures and curve fit equations are detailed later in §5.2.1. The mean and variance of the repetitions were stored in a spreadsheet after each replication. The replication data were reviewed for any extreme variations from steady state conditions and within replications.

4.6 Operating Procedure Summary

A standardized operating procedure was used to maximize uniformity in data collection. As discussed, data for each experimental run are only analyzed at steady state conditions. Steady state was reached when the fluid level in the exit plenum, the exit pressure, and all the manifold temperatures did not change more than approximately five percent for a minimum of fifteen minutes. The operating procedure is conveniently divided into three sets of procedures: warm-up, steady state

and shut-down procedures. A summary of the operating procedure follows with a more comprehensive operating procedure provided in Appendix E.

The warm-up procedure brought the experimental flow loop to steady state operating conditions. As the hot oil bath reached the desired operating temperature, the inlet flow was adjusted to the desired flow rate. At the same time, the chiller tray and cold water bath, which were kept at approximately 1 °C throughout the experiments, were allowed to come to temperature. The power supplies to the resistance heater were turned on and the current was set to the desired amount. The vapor pump was also turned on and the vapor plenum pressure was adjusted to achieve the desired vapor extraction pressure difference. Adjustments were made to the needle valves controlling the exit flow rates to steady the liquid hold-up volume inside the exit plenum. Once the exit plenum pressure and inlet subcooling reached the desired values, all temperature and pressure values were monitored for oscillations. Charts of logged replication average values on the LabVIEW™ data acquisition front panel helped verify that steady state conditions were reached.

Upon reaching steady state conditions, data measurements were collected and stored. The inlet flow rate and liquid hold-up level are closely monitored. The hold-up level is monitored by using a reference mark on the Lexan encasing. Small oscillations in the hold-up volume were acceptable but adjustments were made, as necessary, to stabilize it by adjusting the two needle valves downstream of the test manifold. Data were collected for approximately 30 minutes at each test condition.

After data collection for each condition was finished either the warm-up procedure was again performed for a new data point or the shut-down procedure was

begun. The shut-down procedure ensured that the experiment was safely stopped without damaging the test equipment. The power supplies, cold water bath, hot oil reservoir, mass scale and vapor pump were turned off while water circulated through the flow loop, test manifold, and test device. Once the heat sink temperatures were below 40 °C and the hold-up volume drained, the shut-off valves were closed.

5 DATA REDUCTION AND ANALYSIS

To assess the performance of the microscale heat sink utilizing local extraction of vapor, the data must be reduced from measured values such as pressure, mass flow rate, temperature, heater voltage and heater current. The pressure drop and vapor extraction characteristics are calculated from the measured values. The same characteristics are used in representing the predictive model results. Non-dimensional variables used to quantify the heat sink performance are introduced and are used to present experimental data and predictive model results. An uncertainty analysis is then performed to estimate the uncertainty of the results.

5.1 Performance Characteristics

To determine the effect of locally extracting vapor from a two-phase flow on the pressure drop across the heat sink, the inlet and exit pressures must be established. The exit pressure is indirectly measured in the exit plenum with a differential pressure transducer. The differential transducer measures the pressure difference between the inlet and exit plenums and it is subtracted from the measured inlet plenum pressure. As detailed in Fig. 4.6, the inlet pressure is measured 3.5 cm upstream of the heat sink inlet. The measured exit pressure is modified by a pressure drop due to expansion that occurs in the exit plenum. The measured inlet pressure is adjusted to account for the pressure drop due to friction between the pressure transducer and the heat sink inlet, to the ninety degree bend at the inlet and to the abrupt contraction from the inlet plenum of the test manifold to the inlet of the microchannel network. It is probable that other pressure corrections need to be included that are present due to the arrangement and

geometry of the test manifold, e.g. flow around the inlet plenum thermocouple and possible misalignment of heat sink entrance over the inlet plenum of the test manifold. The actual inlet pressure, $P_{in,a}$, is calculated from the measured inlet pressure, $P_{in,m}$, using the following relationship:

$$P_{in,a} = P_{in,m} - \Delta P_{cont} - \Delta P_{bend} - \Delta P_{in,fric} \quad (5.1)$$

where ΔP_{cont} , ΔP_{bend} , and $\Delta P_{in,fric}$ are the pressure drop due to the contraction of the flow, to the ninety degree bend at the inlet and to friction, respectively. Similarly, the actual exit pressure, $P_{ex,a}$, is calculated from the measured exit pressure, $P_{ex,m}$, using

$$P_{ex,a} = P_{ex,m} + \Delta P_{exp} \quad (5.2)$$

where ΔP_{exp} is the pressure drop due to expansion.

The contraction pressure drop is made up of two parts: that due to flow area change alone and that due to the free expansion of the flow following the abrupt over contraction immediately downstream of the contraction. A further explanation is detailed in §6.5.1 and Fig. 6-16 of Blevins [45]. The entrance contraction pressure drop is calculated as

$$\Delta P_{cont} = \frac{\rho V^2}{2} \left[(1 - \theta_{in}^2) + K_{cont} \right] \quad (5.3)$$

where V is the average velocity in the initial heat sink channels ($k = 0$), θ_{in} is the ratio of the total inlet microchannel to total inlet plenum cross-sectional area, and K_{cont} is the abrupt contraction coefficient [12]. The abrupt contraction coefficient is obtained from Table 6-2 in Blevins [45] for laminar flows and is provided in Table 5.1.

Table 5.1: Coefficients values used in Eqs. (5.3) - (5.6).

Coefficient	Value
θ_{in}	0.31
K_{cont}	1.3
θ_{ex}	0.0031
K_{exp}	0.99
K_{90}	1.2

The expansion pressure recovery is similarly broken into two parts and is given as the sum of a reversible pressure rise due to the increased flow area and the irreversible loss due to viscous friction [45]. The expansion pressure drop is calculated as

$$\Delta P_{exp} = \frac{\rho V^2}{2} [(\theta_{ex}^2 - 1) + K_{exp}] \quad (5.4)$$

where K_{exp} is the abrupt expansion coefficient, θ_{ex} is the ratio of the total exit microchannel cross-sectional area to the test manifold exit plenum cross-sectional area, and ρ is the density of the exiting single- or two-phase flow [12]. The expansion coefficient is defined as

$$K_{exp} = (1 - \theta_{ex})^2 \quad (5.5)$$

and its value is provided in Table 5.1.

The loss due to the ninety degree bend is calculated in a similar fashion using

$$\Delta P_{bend} = \frac{\rho V^2}{2} \theta_{in}^2 K_{90} \quad (5.6)$$

where K_{90} is the loss coefficient at the ninety degree bend. Phillips [46] studied these losses and recommended K_{90} to be approximately 1.2. Table 5.1 provides the values used for the coefficients in Eqs. (5.3) – (5.6).

The inlet pressure correction due to friction is used to account for the pressure drop due to friction in the circular flow path between the inlet pressure measurement and microchannel inlet as seen in Fig. 4.6. This correction is calculated using the following form of the steady flow energy equation [47]:

$$\Delta P_{in,fric} = \rho g (h_f - \Delta z) \quad (5.7)$$

where ρ is the density of the inlet flow, g is the gravitational constant, and Δz is the change in gravitational head. The frictional head loss, h_f , is calculated using the correlation

$$h_f = f_D \frac{L V^2}{d 2g} \quad (5.8)$$

where f_D is the Darcy friction factor, L is the length traveled by the flow in the inlet plenum (3.5 cm), d is the diameter of the inlet plenum channel, and V is the velocity of the flow. The friction factor for laminar flow in circular pipes is defined as

$$f_D = \frac{64}{\text{Re}_d} \quad (5.9)$$

where Re_d is the Reynolds number. The Reynolds number for flow in a channel is calculated using the dynamic viscosity, μ , density, velocity, and diameter of the flow in the following relationship:

$$\text{Re}_d = \frac{\rho V d}{\mu} \quad (5.10)$$

Equations (5.7) – (5.10) can be arranged in the following form to calculate the inlet pressure correction due to friction as a function of \dot{m}_{in} , inlet flow rate:

$$\Delta P_{in,fric} = \frac{\rho g \Delta z}{1000} - \frac{0.128 \mu L \dot{m}_{in}}{\pi \rho d_{in}^4} \quad (5.11)$$

Because the flow in the inlet plenum of the test manifold is subcooled, the fluid properties are calculated using tabulated values for compressed liquid water from Engineering Equation Solver (EES). The corrected pressure drop across the fractal is calculated as the difference between the inlet and exit pressures:

$$\Delta P_{frac} = P_{in,a} - P_{ex,a} \quad (5.12)$$

The predictive model similarly calculates the heat sink pressure drop as the pressure difference between the inlet and exit of the microchannels.

The extraction pressure differential, in the strictest sense, is the pressure difference between the pressure at a particular point in the fractal microchannels and the vapor plenum pressure. However, a simplification is made in the current study and it is calculated as the difference between the average corrected pressure of the inlet and exit of the microchannels in the microchannels and the vapor plenum pressure, P_{vap} :

$$\Delta P_{ext} = \frac{P_{in,a} + P_{ex,a}}{2} - P_{vap} \quad (5.13)$$

The effect of local vapor extraction on the pressure drop through the heat sink is represented by introducing a normalized pressure drop. The pressure drop across the microscale heat sink with no vapor extraction, ΔP_0 , is used as the comparison case. The normalized network pressure drop is then defined as

$$\frac{\Delta P_0 - \Delta P_{frac}}{\Delta P_0} \quad (5.14)$$

The pressure drop across the heat sink is a function of, but not limited to, the inlet mass flow rate and extracted vapor flow rate. The total inlet mass flow rate, \dot{m}_{in} , and total exit liquid mass flow rate, $\dot{m}_{ex,l}$, are directly measured using Coriolis mass flow meters. As discussed, the mass flow rate of the extracted vapor is obtained by evaluating the change in mass of condensed vapor as a function of time. Scale readings and a time stamp are recorded simultaneously and a linear regression model is generated during the post-processing. The slope of the regression model represents the extracted vapor mass flow rate, \dot{m}_{vap} . The mass flow rate of the excess vapor, $\dot{m}_{ex,v}$, that was not withdrawn from the microchannel flow through the membranes but rather entered the exit plenum of the test manifold is obtained from the conservation of mass:

$$\dot{m}_{ex,v} = \dot{m}_{in} - \dot{m}_{ex,l} - \dot{m}_{vap} \quad (5.15)$$

The extracted vapor mass flow rate, \dot{m}_{vap} , of the experimental data and predictive model is normalized by defining the ratio of extracted flow, ζ , as:

$$\zeta = \frac{\dot{m}_{vap}}{\dot{m}_{in}} \quad (5.16)$$

To examine the benefit and cost of local vapor extraction, the power required to pump the flow through the microchannel heat sink is compared to the work needed to extract vapor. The network flow power is calculated as

$$\mathcal{P}_{frac} = \frac{\Delta P_{frac} \dot{m}_{in}}{\rho_{in}} \quad (5.17)$$

and the extraction work is calculated using the following relationship:

$$\wp_{vap} = \frac{\Delta P_{ext} \dot{m}_{vap}}{\rho_{vap}} \quad (5.18)$$

If the extracted flow were condensed before it reached the pump that generates the pressure difference across the porous membranes, the density would be increased and the extraction work reduced. In the current study, the extracted flow was condensed but it did not pass through the vapor pump. In presenting the results, it is assumed that in a future application of local vapor extraction from a microscale heat sink that the extracted flow would be condensed before it reached the downstream pump. The cost of condensing the extracted flow is ignored in the current study because it is application dependent. A benefit-to-cost power ratio is developed to compare the reduction in network flow power due to vapor extraction to the extraction work and is expressed as

$$\frac{\wp_0 - \wp_{frac}}{\wp_{vap}} \quad (5.19)$$

where \wp_0 is the network flow power with no vapor extraction. A benefit-to-cost power ratio below one indicates the extraction work is greater than the reduction in the network flow power and vice-versa.

As mentioned in the Test Plan section, the inlet subcooling temperature is nominally maintained constant throughout the experiments at 2.5 K with deviations as large as 1.5 K from this value. The subcooling is measured as the difference between the saturated temperature at the inlet and the inlet temperature. The saturation temperature at the inlet is calculated as a function of the heat sink inlet pressure, $P_{in,a}$, using EES tabulated values.

The rate of heat generated by the resistance heater, \dot{Q}_{htr} , during the experimental data collection is calculated as the product of the voltage across the power supply and the current supplied to the resistance wire:

$$\dot{Q}_{htr} = V_{ps} I_{ps} \quad (5.20)$$

A fraction of the heat generated is not transferred to the flow in the heat sink and is lost to the surrounding environment. An electric circuit analogy illustrated in Fig. 5.1 is used to determine the amount of heat transferred to the fluid inside the heat sink where

$$\dot{Q}_{frac} = \dot{Q}_{htr} - \dot{Q}_{vap} - \dot{Q}_{ex} \quad (5.21)$$

The top two circuit branches in Fig. 5.1 represent the heat transferred to the vapor plenum, \dot{Q}_{vap} , by natural convection, radiation and forced convection and to the exit plenum, \dot{Q}_{ex} , by radial conduction through the porous aluminum, PEEK™, and water

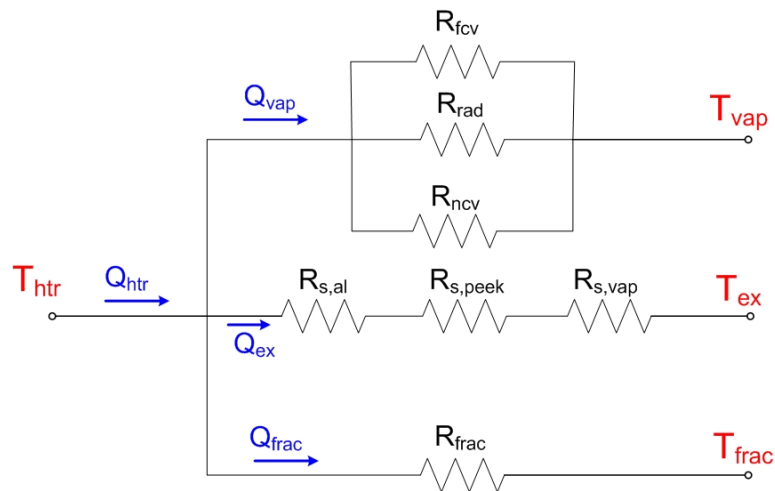


Figure 5.1: Schematic of thermal resistance analogy used to approximate heat loss to the surroundings.

vapor in the exit plenum. The resistors, R , represent thermal resistance to the transfer of heat and the subscripts fcv , rad , ncv , s , al , $peek$, vap , and $frac$ refer to forced convection to the vapor plenum, radiation to the vapor plenum, natural convection to the vapor plenum, side (or radial) conduction, radial conduction through the porous aluminum, radial conduction through the PEEKTM material of the manifold, radial conduction to the excess water vapor in the exit plenum and conduction through the fractal heat sink, respectively. It should be noted that to calculate the rate of heat transferred to the fluid inside the heat sink the thermal resistance of the fractal (of the conduction of heat through the stainless steel) is not needed because it can be calculated from the three other rates of heat transfer. The thermal resistances can be calculated using one of the following relationships, representing two-dimensional conductive and convective or radiative resistances, respectively:

$$R_T = -1/Sk \quad (5.22)$$

$$R_T = 1/hA \quad (5.23)$$

where k is the thermal conductivity of the conductive medium, A is the cross-sectional area, S is the shape factor for two-dimensional conduction (explained later in this section), and h is the convective or radiative heat transfer coefficient.

The thermal resistances in the middle branch of Fig. 5.1 represent the loss of heat to the exit plenum, \dot{Q}_{ex} . Each thermal resistance in this branch represents a radial conductive resistance calculated using Eq. (5.22) and the shape factor for two-dimensional conduction in concentric cylinders [48]:

$$S = \frac{2\pi L}{\cosh^{-1}\left(\frac{d_o^2 + d_i^2}{2d_o d_i}\right)} \quad (5.24)$$

where L is the height of the cross-sectional area through which radial conduction occurs (approximately 6.4 mm), d_o and d_i represent the outer and inner diameter of the cylindrical area through which the radial conduction occurs, respectively. The rate of heat loss to the exit plenum is approximated using the temperature difference between the heater, T_{hr} , and the exit plenum, T_{ex} , and the sum of the radial conduction thermal resistances:

$$\dot{Q}_{ex} = \frac{T_{hr} - T_{ex}}{R_{s,al} + R_{s,peek} + R_{s,vap}} \quad (5.25)$$

The rate of heat loss to the vapor plenum, \dot{Q}_{vap} , is the sum of the rates of heat transfer due to forced convection, radiation and natural convection to the vapor plenum and is approximated using the relationship:

$$\dot{Q}_{vap} = \frac{T_{hr} - T_{vap}}{R_{vap}} + \dot{Q}_{fcv} \quad (5.26)$$

where T_{vap} is the vapor plenum pressure, \dot{Q}_{fcv} is the forced convection heat transfer to the exit plenum and R_{vap} is the effective thermal resistance of heat transfer to the vapor plenum due to natural convection and radiation. Due to complexity, the thermal resistance of heat transfer due to forced convection is not calculated but rather this rate of heat loss, \dot{Q}_{fcv} , is directly calculated and added to the rate of heat loss due to both natural convection and radiation. This rate is calculated using the energy balance relationship:

$$\dot{Q}_{fcv} = \dot{m}_{vap} (i_{vap} - i_{frac}) \quad (5.27)$$

where i_{vap} is the enthalpy of vapor in the vapor plenum and i_{frac} is the enthalpy of saturated vapor at the average pressure in the microchannels. In essence, an increase in the enthalpy of the extracted vapor signifies that heat is being lost due to forced convection.

The thermal resistance of heat transfer due to natural convection in the vapor plenum is calculated using Eq. (5.23) and is found by first using the Rayleigh number to find the average Nusselt number from a horizontal heated plate based on the following correlation [48]:

$$Ra = \frac{gB(T_{htr} - T_{vap})L^3}{\nu\alpha} \quad (5.28)$$

$$\overline{Nu}_L = 0.54Ra^{1/4} \quad (5.29)$$

In these correlations, B is the inverse of the mean temperature of T_{htr} and T_{vap} , T_{htr} is the porous aluminum surface temperature, L is the characteristic length defined as the ratio of the heater's top surface area and the perimeter of the top surface of the heater, and ν and α are the kinematic viscosity and thermal diffusivity of the extracted vapor, respectively. The average forced convective heat transfer coefficient, \overline{h}_{fcv} , is then calculated using the definition of the Nusselt number:

$$\overline{Nu}_L = \frac{\overline{h}_{fcv}L}{k} \quad (5.30)$$

where k is the thermal conductivity of the extracted vapor. This heat transfer coefficient, \overline{h}_{fcv} , and the top cross-sectional area of the heater are used in Eq. (5.23) to calculate R_{fcv} .

In addition to R_{fcv} , the radiation thermal resistance, R_{rad} , is needed to calculate the effective thermal resistances of heat transfer to the vapor plenum due to forced convection and radiation. The radiation thermal resistance is calculated utilizing Eq. (5.23) and the definition of the radiation heat transfer coefficient:

$$h_{rad} = \varepsilon\sigma(T_{htr} + T_{vap})(T_{htr}^2 + T_{vap}^2) \quad (5.31)$$

where ε is the emissivity of the heater (approximately 0.3) and σ is Boltzman's constant.

The effective thermal resistance of heat transfer to the vapor plenum due to natural convection and radiation to be used in Eq. (5.26) is calculated using the following relationship for resistors in parallel:

$$R_{vap} = \frac{R_{ncv}R_{rad}}{R_{ncv} + R_{rad}} \quad (5.32)$$

5.2 Uncertainty

An uncertainty analysis of the experimental data was done by dividing the error into two parts: bias error and precision error. From these two errors, uncertainty values were determined for each independent variable. Subsequently, propagation of the independent-variable uncertainty values to the dependent variables was calculated using the Kline-McClintock method [49].

5.2.1 Bias error

The bias error of an independent variable is estimated by the calibration error. Calibration of measurement instrumentations is required in order to reduce the manufacture uncertainty of the output readings. Most of the instrumentation used in

the data collection were previously calibrated and integrated into the test loop. However, two new pressure transducers were added to the existing experimental setup and required calibration. Both transducers have an absolute pressure range of 0 – 2.07 bar (0 - 30 psi). They were calibrated using a pressure chamber with several ports. A compressed air line was connected to one port controlled by a pressure regulator. The two transducers and a standard were connected to four other ports. The pressure standard (Omega Model PCL-MB and Serial No. GQS-26484) had an absolute pressure range of 0 – 6.9 bar (0 – 100 psi) with an uncertainty of 0.345 kPa (0.05 psi). The voltage output of the pressure transducers was recorded as a function of the absolute pressure output of the standard. Eleven pressure values were chosen within the expected range of the transducers from 1 to 1.75 bar (14.7 – 25 psi). At each point, five thousand voltage readings for each transducer were collected. Along with these samples, the mean and standard deviation of the samples and the standard pressure were recorded. Starting at ambient pressure, the pressure of the chamber was incrementally increased to the greatest value, then incrementally decreased and incrementally increased once again. This cycle was performed to identify any hysteresis effects associated with the transducers. No hysteresis effects were observed for both pressure transducers. In total, thirty-three data points were evaluated for the calibration of these transducers. The bias error of the pressure transducers (and independent variables in general) is defined in this study as

$$u_B = \sqrt{(e_{standard})^2 + (e_{curvefit})^2 + \left(\frac{\partial P}{\partial V} e_V\right)^2} \quad (5.33)$$

where $e_{standard}$ is the error associated with the calibration standard, $e_{curvefit}$ is the error of the curve fit, e_V is the error associated with data acquisition and experimental procedure variants relating to the standard deviation of the voltage values, and

$\frac{\partial P}{\partial V}$ represents the slope of the curve fit. The error associated with the calibration

standard is given by the manufacturer; the standard used in this calibration procedure had an uncertainty of 0.05% of its full scale pressure or 0.345 kPa (0.05 psi).

The curve fit error is determined by

$$e_{curvefit} = t_{\nu,95\%} e_{std} \quad (5.34)$$

where t is the Student-t distribution factor for 95% confidence, ν is the number of degrees of freedom of the fit and e_{std} is the standard error of the curve fit defined as

$$e_{std} = \sqrt{\frac{\sum_{i=1}^N (y_i - y_{ci})^2}{\nu}} \quad (5.35)$$

where N is the total number of data points and the quantity $y_i - y_{ci}$ is the difference between the measured value, y_i , and the value predicted from the curve fit, y_{ci} . The number of degrees of freedom used in Eqs. (5.34) and (5.35) is

$$\nu = N - (m + 1) \quad (5.36)$$

where m is the order of the curve fit (usually one) and N is the number of data points in the curve fit analysis. The standard errors of the curve fits for the pressure transducers were found using regression analysis in Microsoft Excel. For example, the calibration curve for the vapor-plenum pressure transducer is shown in Fig. 5.2 where P_{vap} is the absolute pressure measured by the calibration standard in kPa and

V_{vap} is the voltage output from the transducer. The curve fit equation of the vapor-plenum pressure transducer is $P_{vap} = 2037.3V_{vap} + 1.5351$. The standard error of the curve fit for P_{vap} is ± 0.093 kPa (0.0135 psi).

The error associated with variants in the calibration procedure is found by

$$e_V = t_{v,95\%} \frac{S_{x,max}}{\sqrt{N_{sample}}} \quad (5.37)$$

where v is equal to N_{sample} or the number of samples (repetitions) taken at each point and $S_{x,max}$ is the largest standard deviation of the calibration data points [49]. Usually, the average of the standard deviations is used, but in this study the maximum value is used to be conservative.

Using Eq. (5.33), the bias error of the two pressure transducers is calculated and reported in Appendix D. Similar calibration procedures were previously

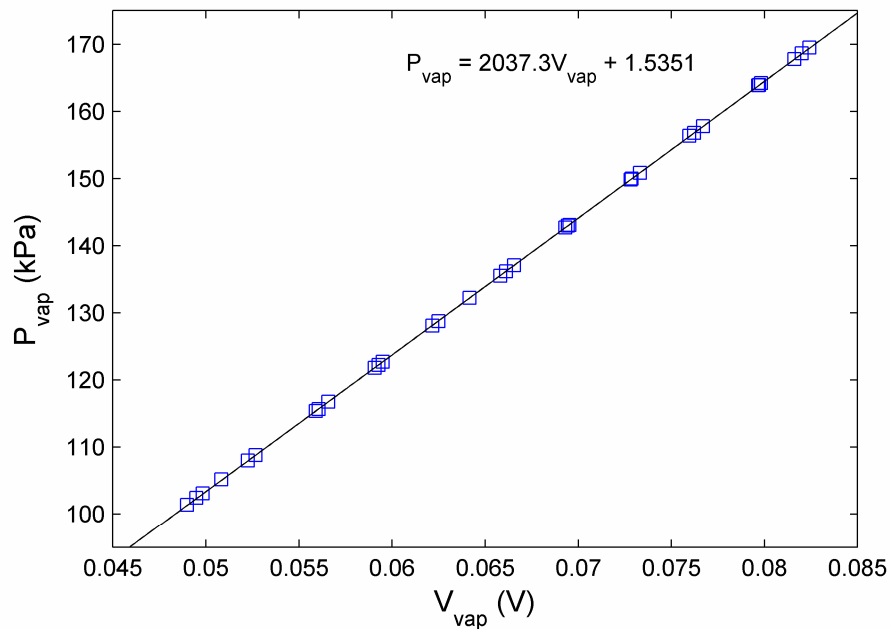


Figure 5.2: Plot of the pressure reading of the vapor plenum pressure transducer as a function of the output voltage.

performed for the existing pressure transducers, thermocouples and mass flow meters present in the test loop. A table of curve fit equations, the associated uncertainty, and measurement ranges are reported in Appendix D for each instrument used for data acquisition.

5.2.2 Precision error

The experimental precision error for each independent variable is calculated using pooled statistics [49]. The 95% precision error is calculated as

$$u_p = t_{M(N-1),95\%} \langle S_{\bar{x}} \rangle \quad (5.38)$$

where the Student-t distribution factor, t , is evaluated with a degree of freedom of $M(N-1)$, if M is equal to the number of replications and N is the number of repetitions or samples. Recall that repetitions are the number of data points in each replication.

The value $\langle S_{\bar{x}} \rangle$ represents the pooled standard deviation of the means and is calculated as

$$\langle S_{\bar{x}} \rangle = \sqrt{\frac{1/M \sum_{j=1}^M S_{xj}^2}{MN}} \quad (5.39)$$

where S_{xj} is the standard deviation calculated for each replication and j is index represents the replications, respectively.

The precision error of the extracted vapor flow rate is calculated using the precision estimate of the slope of the accumulated vapor mass as a function of time rather than the pooled standard deviation of the means. As mentioned in the previous section, a linear regression analysis of the extracted vapor mass and the time elapsed is used to identify the flow rate. The precision estimate of the flow rate is calculated as

$$\langle S_{\dot{m}_{vap}} \rangle = e_{std} \sqrt{\frac{N}{N \sum_{i=1}^N x_i^2 - \left(\sum_{i=1}^N x_i \right)^2}} \quad (5.40)$$

5.2.3 True measured value

The mean value of each experimental data point is calculated as a pooled mean, $\langle \bar{x} \rangle$, using

$$\langle \bar{x} \rangle = \frac{1}{MN} \sum_{j=1}^M \sum_{i=1}^N x_{ij} \quad (5.41)$$

where i and j indices represent the repetitions or samples and the replications, respectively. The pooled mean can also be thought of as an average of the averages. The uncertainty for each experimental data point is taken as the root mean square of the bias and precision errors:

$$u_{\bar{x}} = \sqrt{u_B^2 + u_P^2} \quad (5.42)$$

And the estimate of the true measured value is defined as

$$x' = \langle \bar{x} \rangle \pm u_{\bar{x}} \quad (5.43)$$

5.2.4 Propagation of error

The propagation of the independent variable uncertainty values to the dependent variables is estimated using the Kline-McClintock method. For a given function, R , of n independent variables

$$R = fcn(x_1, x_2, \dots, x_n) \quad (5.44)$$

with uncertainty values u_{x_1} , u_{x_2} , ..., u_{x_n} , the uncertainty in R , u_R , is

$$u_R = \sqrt{\sum_{i=1}^n \left(\frac{\partial R}{\partial x_i} u_{x_i} \right)^2} \quad (5.45)$$

The quantity in the parenthesis is the partial derivative of the dependent variable with respect to a given independent variable multiplied by the uncertainty of that same independent variable.

6 RESULTS AND DISCUSSION

The objective of the current study is to illustrate the feasibility of local vapor extraction through a porous membrane as a means to achieve a reduction in two-phase pressure drop across the heat sink. The model was used to predict the performance of the microscale heat sink as a function of inlet flow rate, input heat and vapor extraction pressure difference. Experimental data were collected in order to validate the predictive model. A sensitivity analysis was performed on the predictive model to estimate the influence of various parameters on the heat sink performance and to help explain some of the discrepancies observed between the experimental results and model predictions. Results of the model predictions are presented and discussed in both dimensional and non-dimensional format. Model predictions are used to discuss trends and physical implications.

6.1 Predictive Model Results

The model was used to predict the performance of the microscale heat sink for test conditions compatible with the experimental setup. However, the range of the independent variables was broadened to obtain a more detailed representation of the heat sink performance. The inlet subcooling and pressure at the exit of the heat sink microchannels were kept constant at 2.5 K and 101.3 kPa, respectively. The inlet flow rate, input heat, and pressure difference across the porous media were incrementally varied from 4 to 16 g/min, 12 to 60 W, and 0 to 60 kPa, respectively.

Model predictions of extracted vapor mass flow rate, \dot{m}_{vap} , versus pressure difference across the membranes are shown in Fig. 6.1 for six heat input values and a

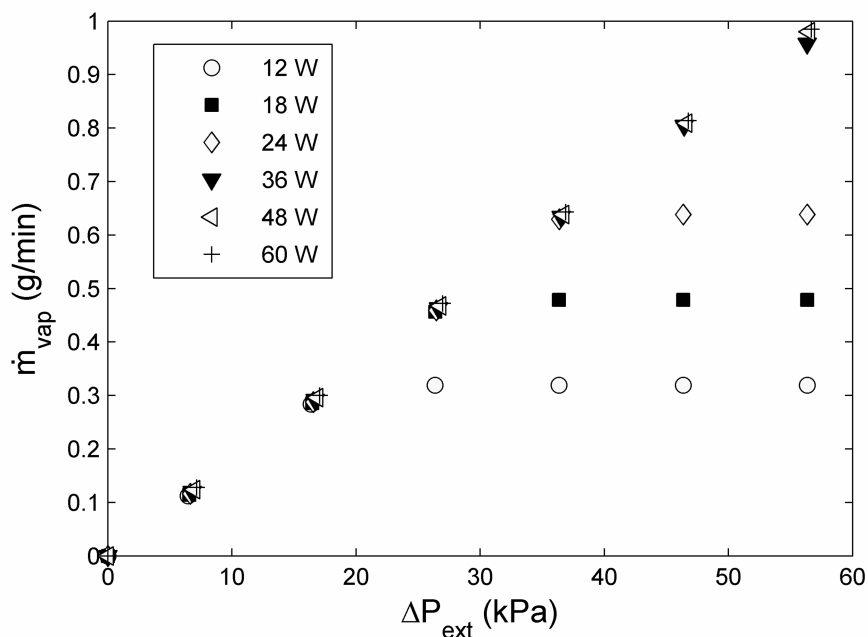


Figure 6.1: The vapor mass flow rate versus the membrane pressure difference for an inlet flow rate of 4 g/min for six heat input values.

fixed inlet mass flow rate of 4 g/min. As expected, the extraction vapor flow rate increases as the membrane pressure difference increases. At extraction pressure differences below 20 kPa, the extracted vapor flow rate values are identical for all the input heat values. The vapor flow rate is limited in this region by the membrane pressure difference and the membrane permeability. As the pressure difference across the membranes is increased, the extraction vapor flow rate plateaus at heat input values at or below 24 W. It appears that the 36 W line is about to plateau at an extraction pressure difference of 58 kPa. The extraction vapor flow rate plateau occurs when no more vapor is available to be extracted, i.e. when all of the vapor has been extracted. As the heat input value is increased, the maximum amount of vapor that can be extracted increases and the onset of the vapor flow rate plateau occurs at higher extraction pressure differences. Although not shown, the other inlet flow rates

modeled predicted the same vapor extraction flow rates and plateau occurrences as observed in Fig. 6.1 because the vapor generated in the microchannels is not modeled as a function of the inlet flow rate.

The extracted vapor mass flow rate normalized by the total inlet mass flow rate, ζ , versus the pressure difference across the membranes normalized by the pressure drop across the microchannel network with no vapor extraction is shown in Fig. 6.2 for four inlet flow rates and a fixed heat input of 12 W. Observed from Fig. 6.2 at low extraction normalized extraction pressure differences is an increase in the fraction of the total mass extracted with increasing normalized membrane pressure difference. Also noted is an increase in the fraction of vapor extracted, ζ , with decreasing inlet mass flow rate. Vapor extraction plateaus near the same membrane pressure difference of approximately 20 kPa for each inlet flow rate as (see Fig. 6.1),

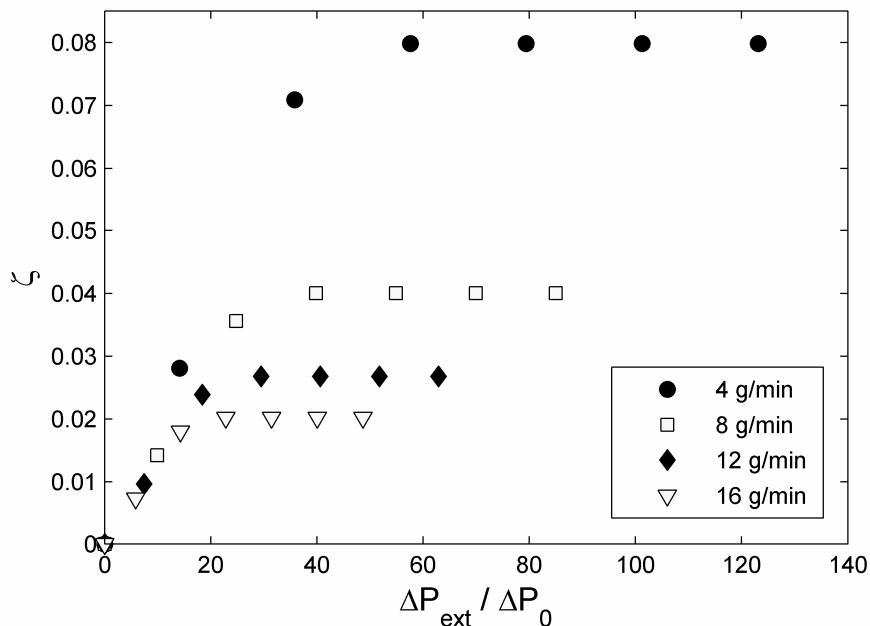


Figure 6.2: The normalized extracted vapor flow rate versus the normalized membrane pressure difference for an input heat of 12 W for four inlet flow rates.

but the plateau occurs at an increased normalized membrane pressure difference with decreasing inlet mass flow rate. For this relatively low heat input of 12 W, local vapor extraction is maximized with a small membrane pressure difference penalty. In contrast, at the highest heat input investigated, vapor extraction never plateaus as observed in Fig. 6.3, which shows the normalized vapor flow rate versus the normalized extraction pressure difference for a fixed heat input of 60 W and the same four inlet flow rates investigated in Fig. 6.2. The same trend of increasing normalized vapor extraction with increasing normalized membrane pressure difference is observed as was in Fig. 6.2. It is also noted that as the inlet flow rate increases, the slope of the trend lines decreases because the amount of vapor extracted predicted is not a function of inlet mass flow rate as mentioned in conjunction with Fig. 6.1.

The pressure drop through the fractal-like branching network, in general, will vary with the inlet flow rate, inlet subcooling and heat input. To inspect the effect of local vapor extraction on the network pressure drop, the network pressure drop, ΔP_{frac} , is plotted as a function of membrane pressure difference, ΔP_{ext} . The resultant plot for an inlet flow rate of 4 g/min is shown in Fig. 6.4. It is observed that as the pressure difference across the membranes increases, the pressure drop across the fractal network decreases. This is explained by the fact that the amount of vapor remaining in the microchannels decreases. As the thermodynamic quality of the flow decreases, the density increases and the velocity decreases resulting in decreased network pressure drop values. As the pressure difference across the membranes increases, it is observed that the network pressure drop plateaus for energy input values at or below 24 W. This coincides with the vapor extraction plateaus observed in Fig. 6.1.

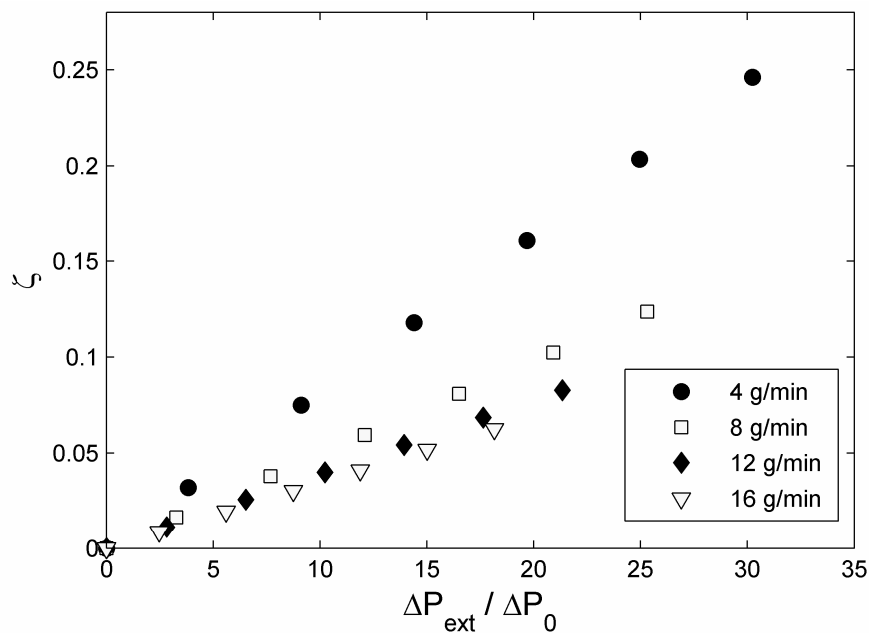


Figure 6.3: The normalized extracted vapor flow rate versus the normalized membrane pressure difference for an input heat of 60 W for four inlet flow rates.

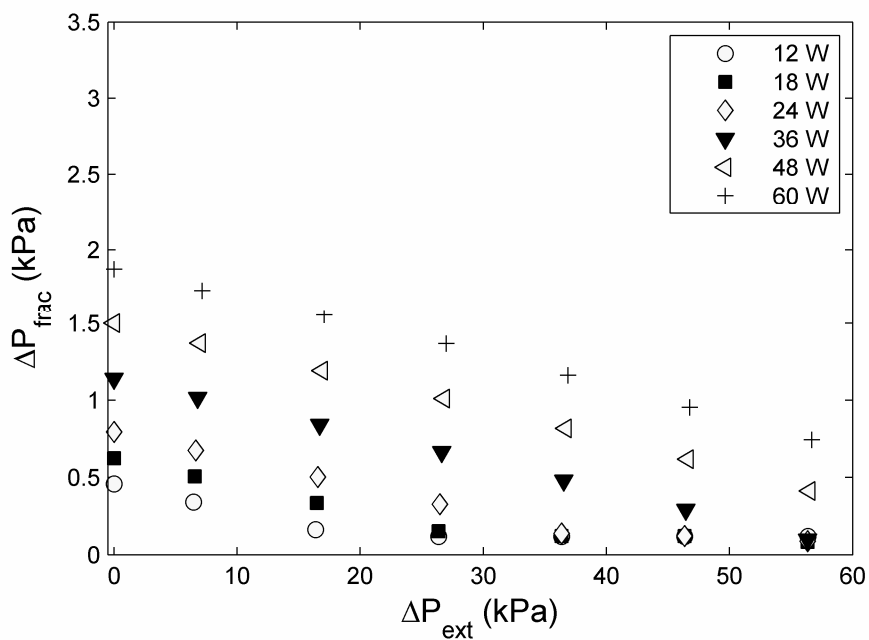


Figure 6.4: Network pressure drop versus the membrane pressure difference for an inlet flow rate of 4 g/min and six input energy values.

Similarly, the pressure drop plateau occurs at increasing membrane pressure difference as the heat input is increased.

For an increased inlet flow rate of 16 g/min, the network pressure drop versus the membrane pressure difference is shown in Fig. 6.5 for the same energy input values as shown in Fig. 6.4. The network pressure drop values have increased, as is expected with the increased inlet flow rate. Because the same trends are observed in Fig. 6.5 as were observed in Fig. 6.4 and the vapor extraction for a given energy input is not predicted as a function of the inlet flow rate, the fractal pressure drop plateau begins at the same membrane pressure differences in Fig. 6.5 as was observed in Fig. 6.4. Although not shown, the same trends were observed for the intermediate inlet flow rate values as observed in Figs. 6.4 and 6.5.

To investigate the reduction in the network pressure drop due to local vapor extraction, the pressure drop reduction, defined as $\Delta P_0 - \Delta P_{frac}$, is normalized by the predictive pressure drop with no vapor extraction, ΔP_0 . The normalized pressure drop

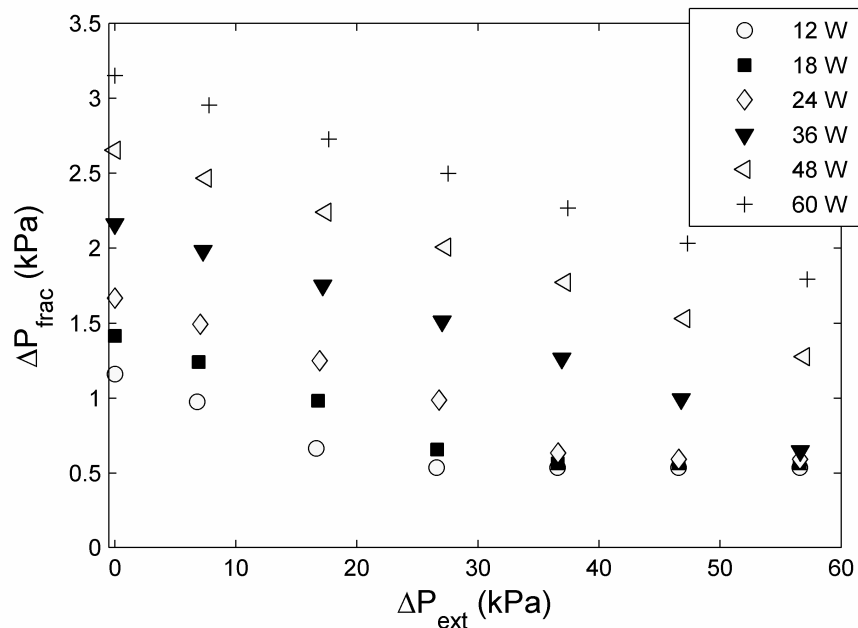


Figure 6.5: Fractal pressure drop versus the membrane pressure difference for an inlet flow rate of 16 g/min and six input energy values.

reduction versus the normalized membrane pressure difference is shown in Fig. 6.6 for a fixed inlet flow rate of 4 g/min and six heat inputs. It is observed that below a normalized membrane pressure difference of 40 the normalized pressure drop reduction for all heat input cases collapse to a single line. This is explained by the observation made of Fig. 1 that the predicted vapor extraction is not a function of heat input for this normalized membrane pressure difference region resulting in a linear normalized pressure drop reduction that is also not a function of heat input. It is observed that the normalized pressure drop reduction for the 12 W heat input condition plateaus. However, the normalized pressure drop reduction of the 18 and 24 W heat input conditions deviate from the linear normalized pressure drop reduction but do not plateau. The normalized pressure reduction of these three heat input conditions deviate from the linear normalized pressure drop reduction in conjunction with the vapor extraction plateaus observed in Fig. 6.2. It is expected that because no more vapor is being extracted, the network pressure drop plateaus as observed in Fig. 6.6 for the 12 W heat input condition. However, the 18 and 24 W heat input conditions did not plateau and the normalized pressure drop reduction continued to increase. This could be explained by the residence time of vapor in the microchannels being reduced with the increased normalized membrane pressure difference above 70. The amount of vapor extracted is not increased as observed in Fig. 6.1, but the pressure drop could be reduced because the length through which the vapor is pushed through the flow network may be reduced. The lack of further normalized pressure drop reduction in the 12 W heat input condition after its plateau could be explained by an insufficient amount of vapor (compared to the total mass flow rate) being generated

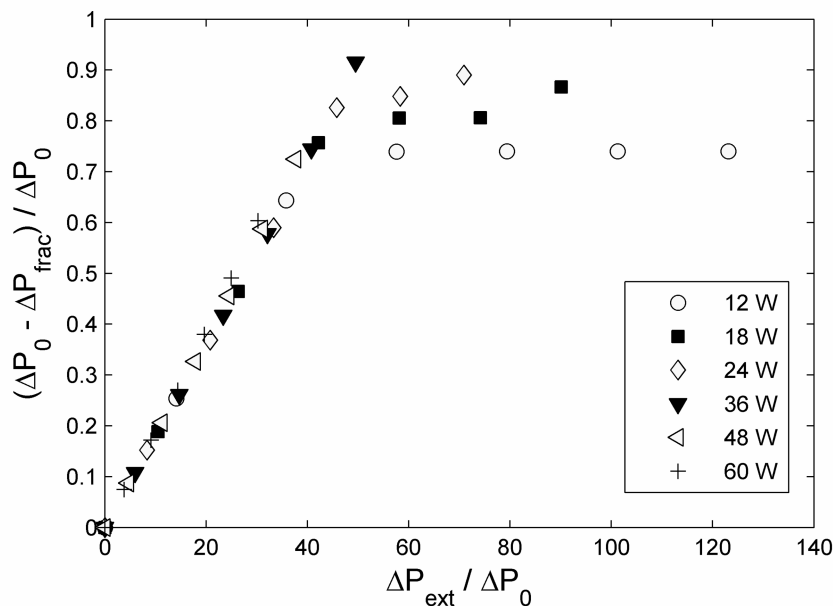


Figure 6.6: Normalized network pressure drop reduction versus normalized membrane pressure difference for an inlet flow rate of 4 g/min and six input energy values.

or normalized membrane pressure differences to reduce the residence time of the extracted vapor. It is also observed that the local extraction of vapor reduces the two-phase pressure drop up to 90% for the conditions modeled, as observed for a heat input of 36 W and a normalized membrane pressure difference of 50 in Fig. 6.6. The normalized pressure drop reduction is limited for a heat input of 48 and 60 W is limited below a normalized membrane pressure difference of 40 because the membrane pressure difference did not range above 60 kPa.

The normalized reduction in fractal pressure drop versus the normalized membrane difference for an increased inlet flow rate of 16 g/min and the same heat input values as shown in Fig. 6.6 are presented in Fig. 6.7. The same general trends are observed as those in Fig. 6.6. However, the normalized pressure drop reduction deviates from the linear trend for the 12, 18 and 24 W heat input conditions before

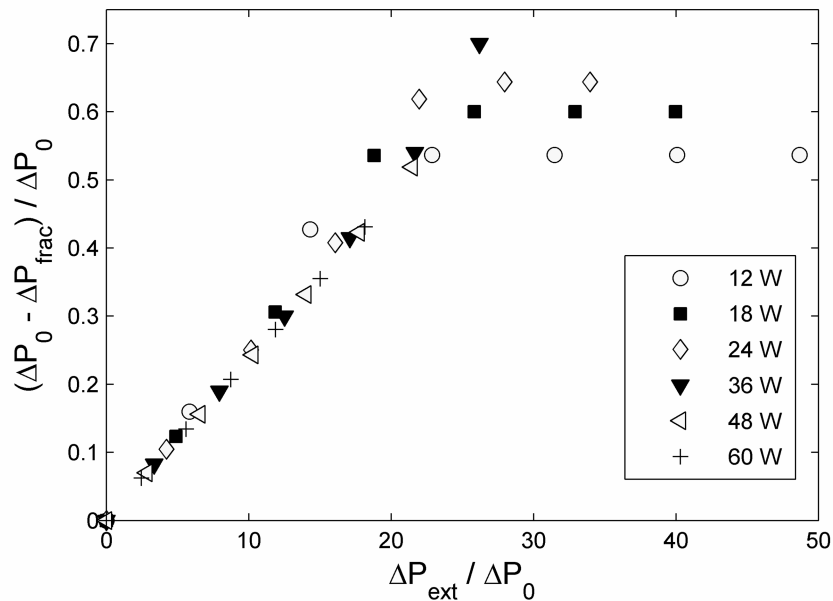


Figure 6.7: Normalized network pressure drop reduction versus the normalized membrane pressure difference for an inlet flow rate of 16 g/min and six input energy values.

they plateau at a normalized membrane pressure difference of 20. It is proposed that this observed increase in the slope of the normalized pressure drop reduction is caused by the large density gradient of saturated fluid in the low quality region (less than 0.0025). In Fig. 6.2 it is observed that the 16 g/min heat input condition has nearly maximized its vapor extraction at a normalized membrane pressure difference of 15. The results observed in Fig. 6.7 experience an exponential increase in the fluid density just before the plateau of the normalized pressure drop reduction resulting in the observed increase in its slope. The same trend is not observed in Fig. 6.6 because there is not sufficient resolution in the results just before the normalized pressure drop reduction plateau. The normalized pressure drop reduction not increasing after the plateaus observed in Fig. 6.7 and for the other inlet flow rates evaluated could be

explained by the normalized pressure differences not being large enough to reduce the residence time of the vapor for these conditions.

The benefit-to-cost flow power ratio versus the membrane pressure difference for an inlet flow rate of 4 g/min and four energy input values are presented in Fig. 6.8. As mentioned in the data reduction and analysis, a benefit-to-cost flow power ratio below one indicates that the extraction work is greater than the reduction in the network flow power. It is observed that the benefit-to-cost power ratio decreases as the membrane pressure difference increases. It is also observed that the power benefit-to-cost ratio remains below one for the conditions considered in Fig. 6.8.

For an increased inlet flow rate of 16 g/min, the benefit-to-cost flow power ratio versus the membrane pressure difference is shown in Fig. 6.9 for the same energy input values as shown in Fig. 6.8. The benefit-to-cost flow power ratio values have increased in Fig. 6.9 in comparison to Fig. 6.8, as is expected with the increased inlet

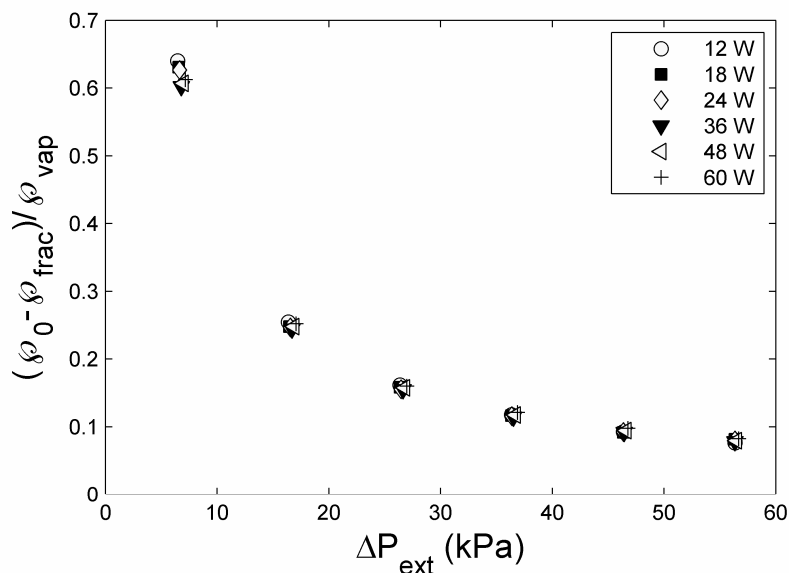


Figure 6.8: Benefit-to-cost power ratio versus the membrane pressure difference for an inlet flow rate of 4 g/min and six input energy values.

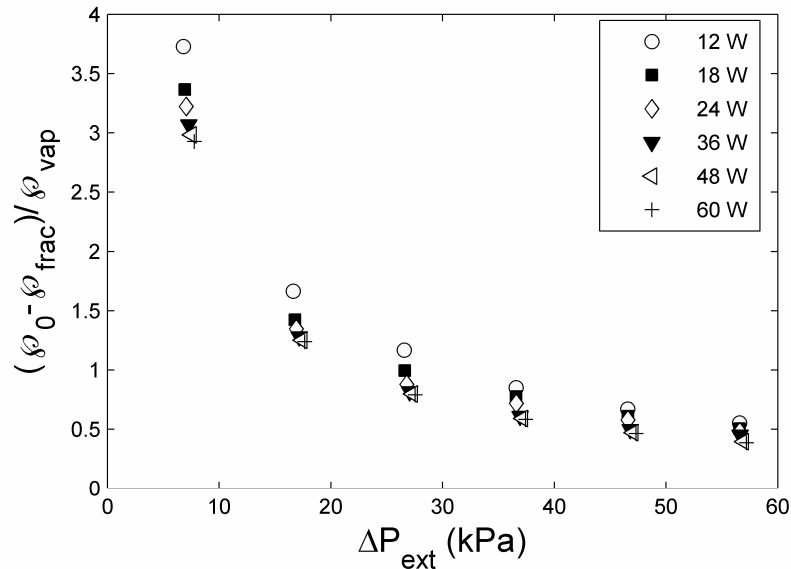


Figure 6.9: Benefit-to-cost power ratio versus the membrane pressure difference for an inlet flow rate of 16 g/min and six input energy values.

flow rate. A similar relationship between the benefit-to-cost power ratio and the membrane pressure difference is observed in Fig. 6.9 as in Fig. 6.8. It is also observed that the benefit-to-cost ratio slightly decreases as the energy input is increased. In contrast to the low power ratio values of Fig. 6.8, the benefit-to-cost power ratio is larger than one for a membrane pressure difference less than approximately 30 kPa. Although not shown, the same trends were observed for the intermediate inlet flow rates as observed in Figs. 6.8 and 6.9

6.2 Predictive Model Validation

To validate the predictive model, inlet subcooling, inlet flow rate, input energy, vapor plenum pressure and exit plenum pressure values were used as input for model predictions. The experimentally measured pressure drop across the network was corrected using the contraction, expansion, bend and friction pressure correction

equations discussed in §5.1—Eqs. (5.1) – (5.11). The experimentally measured network pressure drop values were corrected by 0.28 to 0.38 kPa using these correlations, but pressure adjustments of 1.2 to 2.3 kPa were needed to obtain good agreement between the experimentally measured and theoretically predicted network pressure drop values. Because the pressure corrections did not adequately adjust the experimental data it was assumed that the macroscale correlations may not characterize well the losses at the microscale. Therefore, an experimental approach was undertaken to account for the pressure drop inside the flow network itself. Because most minor losses will occur between the pressure transducer in the inlet plenum of the manifold to the inlet of the fractal-like flow network and because the fluid enters the fractal-like flow network subcooled, pressure drop corrections were experimentally acquired under three single-phase conditions with inlet flow rates of 8, 10 and 12 g/min, a nominal inlet subcooling of 2.5 K, and no heat input. The predictive model was also run for identical conditions. The measured single-phase pressure drop was compared to the single-phase predicted pressure drop for each test case. These differences were subtracted from the experimental two-phase pressure drop values to correct for the inlet minor losses. This is appropriate because the inlet conditions for the two-phase experimental test conditions are similar to those of the single-phase calibration points due to the similar inlet subcooling flow conditions. An order of magnitude analysis on the expansion coefficient at the periphery of the fractal network indicates that the pressure correction due to expansion is negligible for both single-phase and two-phase testing conditions. As devised, this experimental pressure correction accounts for the pressure drop due to the flow obstruction of the inlet

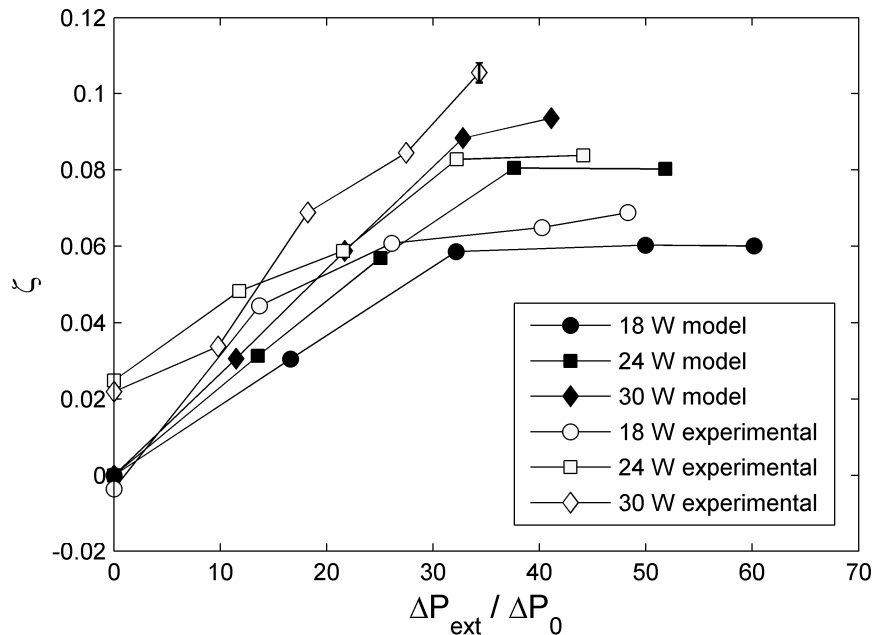


Figure 6.10: Normalized extracted vapor flow rate versus normalized membrane pressure difference of the predictive model and experimental data for an inlet flow rate of 8 g/min.

plenum thermocouple, possible misalignment of the fractal network inlet hole over the inlet plenum and other factors in addition to those discussed in §5.1.

The mass extraction and network pressure drop results of the experimental testing and predictive model are reported together in Figs. 6.10 and 6.11, respectively. The normalized vapor flow rate versus the normalized extraction pressure difference is shown in Fig. 6.10 for an inlet flow rate of 8 g/min and three heat input cases. The measurement uncertainties of the experimental data associated with ζ in Fig. 6.10 are 3 – 9% (approximately the size of the symbols used) and 1 – 5% associated with the normalized extraction pressure difference, $\Delta P_{ext} / \Delta P_0$. A representative uncertainty value of the normalized vapor flow rate is shown in Fig. 6.10. For normalized membrane pressure difference values above 20, the discrepancy between the model and experimental data remains below 20%. For normalized membrane pressure

differences below 20, a larger difference as well as different slopes for the 18 and 24 W heat input lines were observed. It was also observed that the normalized vapor flow rate for the 18 and 24 W heat input conditions was not near zero for a normalized membrane pressure difference of zero. These unexpected observations could be explained by the definition of the membrane pressure difference. The membrane pressure difference is defined in the current study as the difference between the average pressure in the flow network minus the vapor plenum pressure. However, there exist local membrane pressure differences above zero that facilitate the extraction of vapor. Otherwise, it is presently unclear why these normalized vapor flow rate values were significantly greater than zero. It is also observed that the model consistently under predicts the amount of vapor extracted from the two-phase flow. Similar differences between the model predictions and experimental data were observed for the two other inlet flow rates of 10 and 12 g/min. The most that the normalized vapor flow rate was under predicted for all the data is 0.025 with an average under prediction of 0.01. The quality of these predictions will be further assessed after investigation of the network pressure drop results.

The network pressure drop values are shown in Fig. 6.11 versus the membrane pressure difference for an inlet flow rate of 10 g/min and three heat input values. The measured uncertainty in the network pressure drop is 1 – 3% and is 1 – 5% in the extraction pressure difference. A representative uncertainty value of the pressure drop across the fractal network is shown in Fig. 6.11. At membrane pressure difference values below 20 kPa, the pressure drop values are similar in both the predictive model and experimental data. As the membrane pressure difference is increased, the model

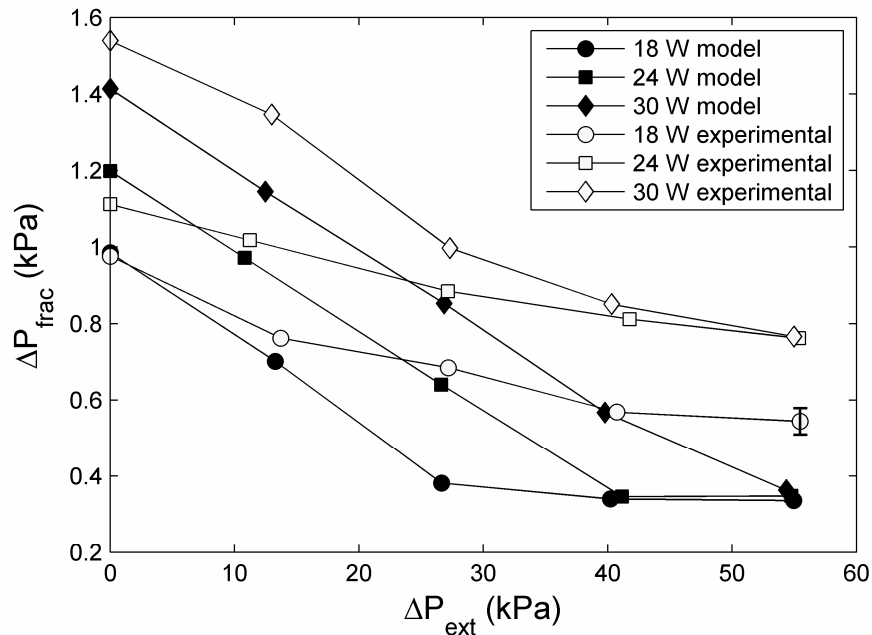


Figure 6.11: Network pressure drop versus membrane pressure difference of the predictive model and experimental data for an inlet flow rate of 10 g/min.

predicts a greater pressure drop reduction than that observed experimentally. It is observed that the difference between the model results and experimental data for the network pressure drop with no vapor extraction in Fig. 6.11 increases as the input energy increases. This could be explained by a portion of the heat input being transferred to the flow in the inlet plenum and as the heat input is increased the flow may reach saturation before entering the microchannels. This would increase the inlet plenum minor losses, e.g. the contraction of the flow at the inlet of the microchannels. Below a membrane pressure difference of 30 kPa, it is also observed in Fig. 6.11 that the network pressure drop of the predictive model and experimental data for the 30 W energy input condition have the same pressure drop reduction trend; however, above 30 kPa, the trends differ for the 30 W energy input condition. The trends for the other two energy input conditions differ at membrane pressure differences of 15 kPa or

lower. It is unclear why the experimental and theoretical trends of the network pressure drop for the 30 W energy input condition are more similar than the trends of the network pressure drop for the 18 and 24 W energy input conditions. The discrepancies between and the observed trends of the experimental data and predictive model are similar for the other two inlet flow rates of 8 and 12 g/min. Reasons are not obvious; however, microscale uncertainties present in the current study considered minor in macroscale applications may be very large. The most obvious explanation is the compression of the porous membranes into the microchannels resulting in reduced channel heights. One way to assess what may be causing these observed differences between the model and experimental data is to perform a sensitivity analysis on the parameters (variables) used in the theoretical model. A complete compilation of plots comparing the predictive model to experimental data is available in Appendix G.

6.3 Sensitivity Analysis

A sensitivity analysis using the predictive model is performed to quantify the effect of the uncertainty values of various parameters on the heat sink performance. The analysis is conducted by comparing results of perturbed parameters or variables to those from a base case set of parameters and variables. The analysis was conducted for a range of vapor extraction pressure differences. The variables are perturbed sequentially to isolate the effect of each uncertainty value. The base case conditions are listed in Table 6.1 along with their respective perturbed values. The inlet mass flow rate and exit plenum pressure had maximum uncertainty values of 0.75 g/min and 0.4 kPa, respectively. The inlet subcooling had a measured uncertainty of 0.3 K, but

Table 6.1: Base case and perturbed values for the parameters and variables of interest in the sensitivity analysis.

Variable	Base value	Perturbed value
\dot{m}_{in} (g/min)	10	0.75
P_{ex} (kPa)	101	0.50
ΔT_{sc} (K)	2.5	0.50
\dot{Q}_{frac} (W)	24	1
H (μm)	200	15
L_{mem} (μm)	140	15
κ_{mem} (m^2)	1.37×10^{-14}	2.74×10^{-15}
ΔP_{ext} (kPa)	0 – 55 kPa	--

in the experimental data the inlet subcooling values varied by as much as 1.5 K above and below the nominal inlet subcooling value. From the electric circuit analogy discussed in §5.1, it was calculated that a maximum of 1 W of the input heat was lost to the surroundings and the extracted vapor. The uncertainty of the membrane permeability is estimated as 20% as was suggested by the manufacturer. Also, for proper sealing between the membranes and the fractal-like flow network, the membranes partially filled the microchannels as a result of the compression of the test manifold. The adjusted height of the microchannels and thickness of the porous Nylon membranes were estimated to be 15 μm . After removal from the test manifold, the fractal-like microchannel pattern was preserved were the membranes filled the channels. To assess the compressed membrane thickness and reduced microchannel height, digital calipers were used to measure the thickness of the microchannel pattern and the thickness of the membranes between the microchannels. The average thicknesses were used to obtain predictive results from the theoretical model. The uncertainty values of the thicknesses used in the sensitivity analysis contain the

streamwise change in the thickness values and resolution uncertainty of the digital calipers.

The results of the sensitivity analysis, presented in Figs. 6.12-6.17, display the effect of changing parameters and variables by the value of their uncertainty on both the network pressure drop and vapor extraction flow rate. The sensitivity of the predicted pressure drop and vapor mass flow rate to variations in the inlet flow rate, m_{in} , and the exit plenum pressure, P_{ex} , is shown in Figs. 6.12 and 6.13. Subjected to a 7.5% increase and decrease in the inlet flow rate, the pressure drop changes from the base case value by approximately 6% (as is evident from Fig. 6.12) due to the linear relationship between the pressure drop due to friction and mass flow rate. The non-linear effect of vapor generation and extraction on the network pressure drop could explain the lack of an exact linear response in the network pressure drop to perturbations of the inlet flow rate. The change in the extraction vapor flow rate due to changes in inlet mass flow rate, as noted in Fig. 6.13, is negligible.

Changes to the exit plenum pressure as is noted in both Figs. 6.12 and 6.13 causes the membrane pressure difference to be slightly altered. As a consequence, the predicted pressure drop and vapor flow rate values fall on the base case trend line as is noted in both Figs. 6.12 and 6.13. A 0.5 kPa increase and decrease in the exit plenum pressure results in an inverse change of approximately 0.02 kPa to the network pressure drop and a corresponding change of 0.02 g/min to the vapor flow rate. Because both the network pressure drop and extracted vapor mass flow rate plateau for membrane pressure differences above 40 kPa, perturbing the exit plenum pressure does not affect the performance as the maximum amount of vapor is being extracted.

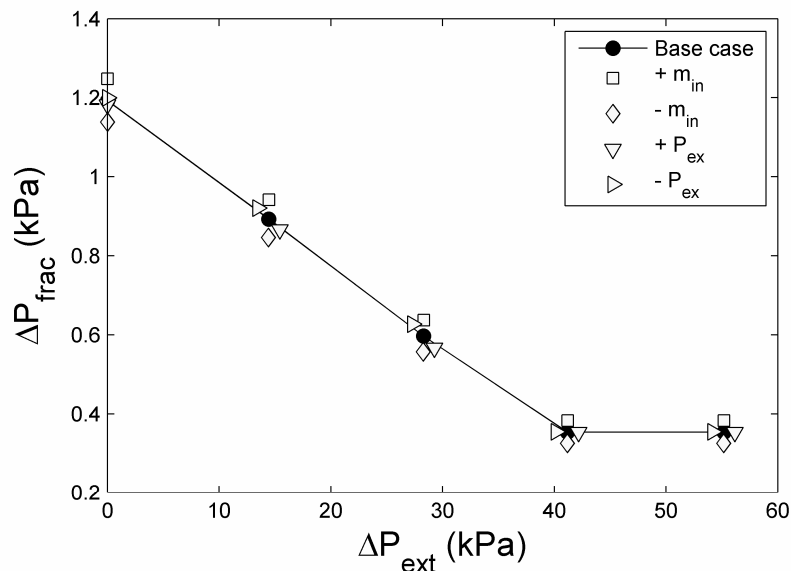


Figure 6.12: Sensitivity analysis of the network pressure drop versus the membrane pressure difference for perturbed values of the inlet flow rate and exit plenum pressure.

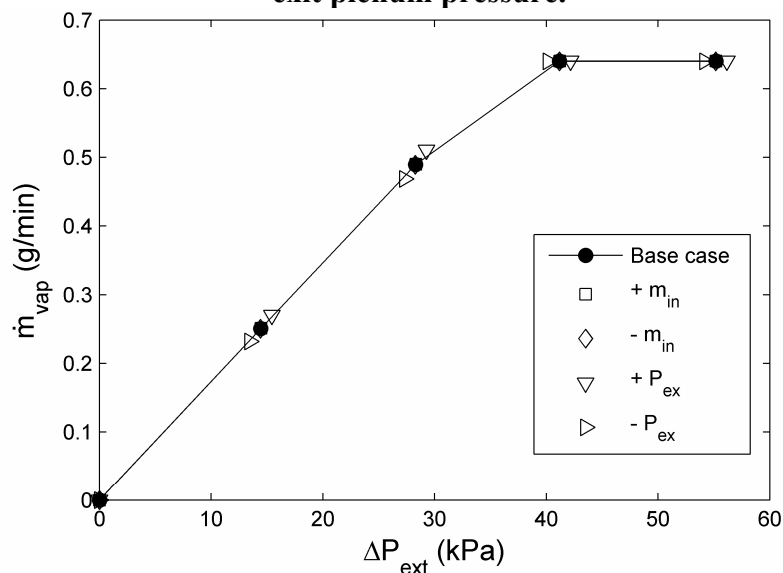


Figure 6.13: Sensitivity analysis of the extracted vapor flow rate versus the membrane pressure difference for perturbed values of the inlet flow rate and exit plenum pressure.

A sensitivity analysis of the inlet subcooling and heat input to predicted performance measurements is summarized in Figs. 6.14 and 6.15. The inlet subcooling, ΔT_{sc} , has a negligible effect on both the network pressure drop in Fig. 6.14

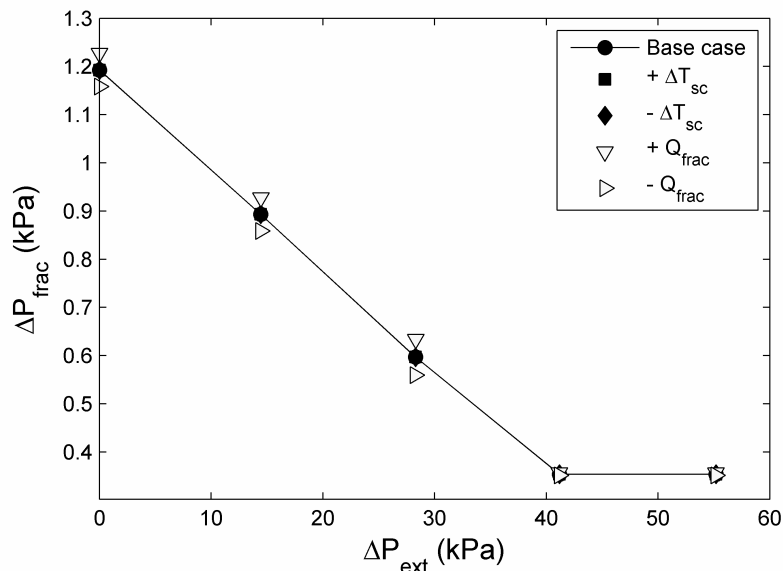


Figure 6.14: Sensitivity analysis of the network pressure drop versus the membrane pressure difference for perturbed values of the inlet subcooling and input energy.

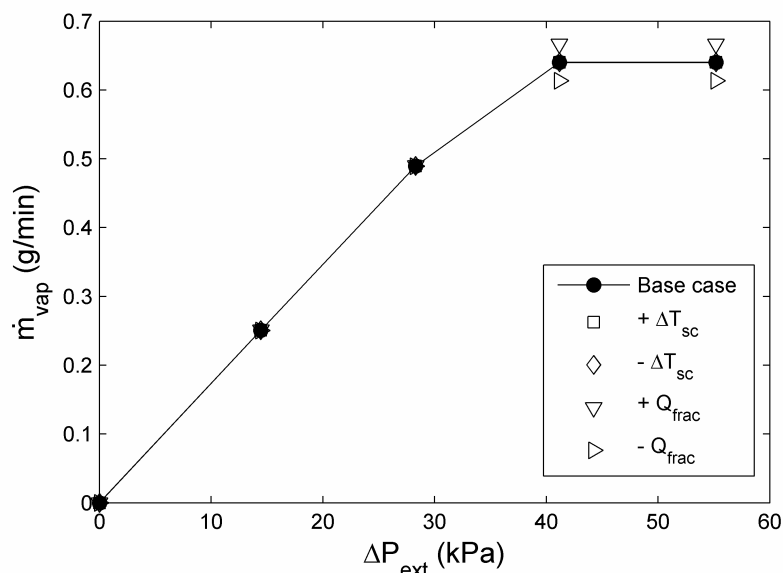


Figure 6.15: Sensitivity analysis of the extracted vapor flow rate versus the membrane pressure difference for perturbed values of the inlet subcooling and input energy.

and the vapor flow rate in Fig. 6.15. This is due to the latent heat dominating the sensible heat. An increase or decrease 1 W to the input heat, Q_{frac} , uniformly increases the network pressure drop by approximately 0.025 kPa for membrane pressure

differences below 40 kPa, as is noted in Fig. 6.14. For membrane pressure differences above 40 kPa, there is no observable change. The opposite effect is seen in the vapor flow rate in Fig. 6.15. Below membrane pressure differences of 40 kPa, there is a negligible change in the vapor flow rate with changes in the heat input because the permeability limits of the membranes prohibit more vapor from being extracted. For membrane pressure differences above 40 kPa, where the extraction vapor flow rate plateaus as a result of all the vapor being extracted, a 0.025 g/min increase in the vapor flow rate is observed with a 1 W increase in the energy input because the maximum amount of vapor available for extraction (or generated) is related to the input heat.

A sensitivity analysis of the microchannel height, H , porous membrane thickness, L_{mem} , and membrane permeability, κ_{mem} , on the network pressure drop and extracted vapor flow rate is presented in Figs. 6.16 and 6.17, respectively. An eight

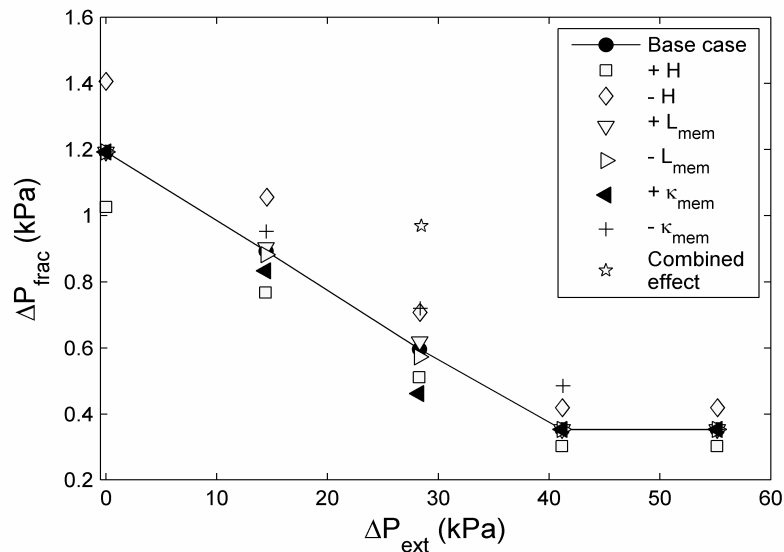


Figure 6.16: Sensitivity analysis of the network pressure drop versus the membrane pressure difference for perturbed values of the microchannel height, membrane thickness and membrane permeability.

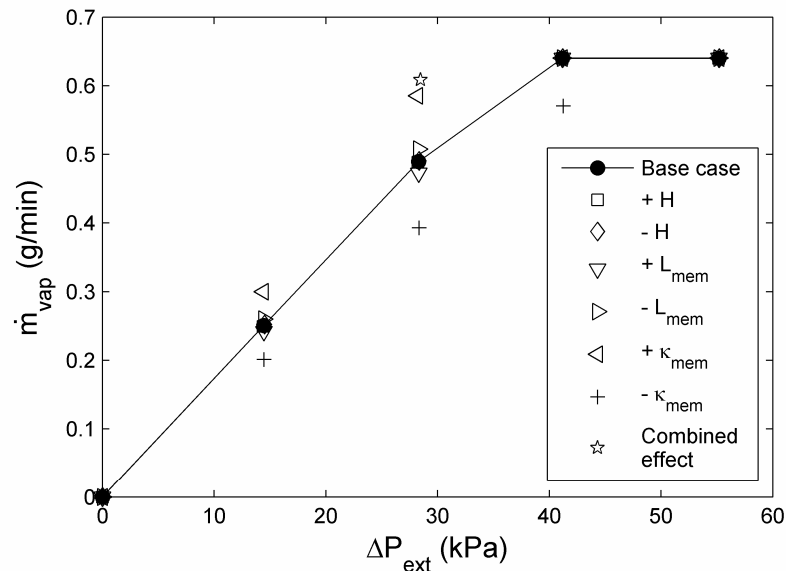


Figure 6.17: Sensitivity analysis of the extracted vapor flow rate versus the membrane pressure difference for perturbed values of the microchannel height, membrane thickness and membrane permeability.

percent increase and decrease in the channel height resulted in approximately a fifteen percent decrease and increase, respectively, in the pressure drop as observed in Fig. 6.16 and a negligible change in the vapor flow rate as observed in Fig. 6.17. The observed change in the network pressure drop is consistent to its inverse square relationship to the channel height for a fixed mass flow rate. Perturbing the membrane thickness had a negligible effect on the pressure drop and only a minor effect on the vapor flow rate. A twenty percent change in the membrane permeability resulted in a significant impact on both the pressure drop across the flow network and the vapor flow rate. A 20% reduction in the permeability increases the resistance to vapor extraction thereby reducing the vapor flow rate by as much as 0.1 g/min and increasing the network pressure drop by as much as 0.17 kPa for a membrane pressure difference of approximately 30 kPa as observed in Figs. 6.16 and 6.17. Also, evident from both Figs. 6.16 and 6.17 is that the membrane pressure difference value at which

the network pressure drop and vapor extraction plateau occurs increases with a decrease in membrane permeability. On the other hand, an increase in the permeability appears to initiate the plateau at a lower membrane pressure difference.

From the sensitivity analysis it is observed from Figs. 6.12, 6.14, and 6.16 that the uncertainty in the inlet mass flow rate, input energy, microchannel height, membrane thickness and membrane permeability have an observable influence on the network pressure drop. In Fig. 6.16, the combined increase in inlet flow rate, input energy and membrane thickness and decrease in the microchannel height and membrane permeability is observed to increase the predicted network pressure drop by 0.4 kPa, as represented by the star symbol. Similarly, it is observed from Figs. 6.13, 6.15 and 6.17 that the exit pressure, input energy, membrane thickness and membrane permeability uncertainty values have an observable influence on the amount of vapor extracted from the flow. In Fig. 6.17, the combined increase in exit pressure, energy input, and membrane permeability and decrease in the membrane thickness is observed to increase the extracted vapor flow rate by 0.1 g/min, as represented by the star symbol.

The sensitivity analysis accounts for a portion of the difference observed between the experimental data and predictive model. Referring back to the energy input of 24 W, inlet mass flow rate of 8 g/min and normalized membrane pressure difference of approximately 20 on Fig. 6.10, which corresponds with the combined sensitivity analysis effect of 0.1 g/min from Fig. 6.17, it appears that the combined uncertainty can account for the difference in the experimental and predicted vapor flow rate. For the same data point on Fig. 6.11, the network pressure drop difference

between experimental and predicted results can be accounted for by the combined uncertainty value of 0.4 kPa from Fig. 6.16. However, for membrane pressure differences above 30 kPa, the combined sensitivity analysis is significantly reduced and cannot solely account for the difference between the experimental data and predicted results. The measured discrepancy between the experimental and predicted results above a membrane pressure difference of 30 kPa is as large as 0.4 kPa whereas that predicted from a combined sensitivity analysis in this region is less than 0.4 kPa at approximately 0.1 kPa.

A sensitivity analysis using the predictive model was performed to quantify the effect of the uncertainty values of parameters on the experimental pressure drop correction. The analysis is conducted by comparing the results of perturbed parameters and variables to those from a base case set of parameters and variables. The analysis was conducted for an inlet flow rate of 8, 10 and 12 g/min. The perturbed parameters and variables included in this sensitivity analysis are the inlet flow rate, exit pressure, and channel height. For an increased inlet flow rate and decreased channel height, the single-phase sensitivity analysis lead to a 0.07 kPa increase in the pressure drop correction resulting in a decreased experimental network pressure drop. This improves the comparison between the model and experimental data for membrane pressure differences below 20 kPa. More details regarding the single-phase sensitivity analysis are discussed in Appendix H. The larger discrepancies in the membrane pressure difference region above 30 kPa could be reconciled by several possible factors. With vapor being extracted, it is possible the flow does not become hydrodynamically fully developed as assumed possible by the

model and, therefore, the higher friction factor values associated with the developing region might need to be incorporated in the model. Furthermore, the extraction of the vapor from the microchannels possibly reduces the thickness of the hydrodynamic boundary layer at the top wall which would lead to an increased velocity gradient at the wall. This would increase the wall shear stress and network pressure drop. One or both of these explanations might account for the additional difference between the predictive model and experimental data in the membrane pressure difference region above 30 kPa not accounted for by the sensitivity analysis. Another probable source of error is that the model was generated assuming a separated two-phase flow regime. It is possible that the flow is not in the separated flow regime and the predictive model needs to be modified. To assess these effects, a fundamental experimental examination of the flow conditions, i.e. velocity and void fraction, could be undertaken.

7 CONCLUSIONS AND RECOMMENDATIONS

A study of the effect of local vapor extraction on the network pressure drop during convective boiling in a fractal-like microchannel heat sink has been carried out. The thesis statement was analyzed both experimentally and theoretically with a predictive model. Correlations and equations governing two-phase flow and pressure distributions in microchannels and governing vapor transport through porous media were programmed in MATLAB[®]. The predictive model was run for a wide range of operating conditions. An experimental set up was also designed and fabricated to facilitate the experimental validation of the thesis statement and the predictive model. The experimental data was collected and analyzed for a limited range of operating conditions considered in the predictive modeling.

It was proposed that the local extraction of vapor from two-phase flows in branching microchannel heat sinks (using a relatively small pressure differential across a hydrophobic, porous membrane) should maintain the high heat flux capabilities of two-phase flows, but yield a reduction in streamwise (radial) pressure drop. The predictive model results and experimental data focused on the feasibility of local vapor extraction from convective boiling in microchannels and its beneficial impact on the network pressure drop of two-phase flows. The vapor phase extraction is shown to be feasible and dependent on the pressure difference applied across the membrane, the energy input, the membrane intrinsic permeability, the membrane thickness, and the inlet mass flow rate of subcooled liquid entering the heat sink.

The network pressure drop is reduced with increasing vapor extraction. Pressure drop values were reduced by as much as 80% in the model results and by as much as 50% in the experimental data for similar testing conditions. The reduction in pressure drop values exceeds the reduction in pressure drop simply due to decreased mass flow rates through the microchannel network. It was also observed that the reduction in the network flow power exceeded the work needed to locally extract vapor for low membrane pressure differences and large inlet flow rates. It should be noted that the benefit-to-cost power ratio was evaluated assuming the extracted vapor was condensed. The cost of vapor extraction should be increased to include the cost of condensation however this was not included in the analysis because it is possible that this could be done using “free” energy depending on the application.

Good agreement within 35% was shown between the pressure drop values of the predictive model and experimental data in the low membrane pressure difference below 25 kPa. The discrepancy between the results and the data increased as the membrane pressure difference increased. Several possible explanations are proposed for the observed differences. (1) The model was generated without incorporating the possible influence of vapor extraction on the governing equations and their underlying assumptions for two-phase pressure distribution in the microchannels. (2) The predictive model assumed that the flow reached fully-developed hydrodynamic conditions in the microchannels. White [25] argues that fully-developed conditions cannot be assumed when suction (vapor extraction) or injection occurs to an internal flow. Rather, the flow remains in the developing regime and the friction factor values are increased over those of fully developed flows. (3) Vapor phase extraction likely

also reduces the thickness of the velocity boundary layer, which would result in a greater velocity gradient at the wall. The increased velocity gradient increases the wall shear stress and the pressure drop needed to drive the flow. (4) It is also possible that the flow is not in the annular two-phase regime as assumed in developing the model and that correlations and governing equations for slug two-phase flows need to be incorporated.

Several recommendations are suggested to improve the predictive model and experimental facility. The test manifold and experimental flow loop should be modified to allow visual inspection of the two-phase flow in the microchannel branching network. The flow regimes present under vapor extraction conditions need to be identified. It is possible that different regimes are present as the membrane pressure difference is changed. Interactions between the liquid and vapor phases with and without vapor extraction should be investigated. From flow visualization studies, the predictive model should be modified to include the characteristics of the flow regime(s) present and the interaction between the two phases. Visual inspection will increase understanding of the physical interpretations of the observed results and will improve the accuracy and validity of the predictive model.

Many problems were encountered during the fabrication of the experimental setup and the collection of the experimental data. Most of these problems were associated with the thermal limitations of the porous media. The initial hydrophobic membranes used melted and filled the fractal microchannel network. Half of the porous aluminum surface is blocked by the heater wire and thermal cement. The energy input is limited by the temperature limits of the porous aluminum and

hydrophobic membranes and the amount of embedded resistance wire. To remove these and other similar problems and limitations, it is recommended that an alternative method be pursued. It may be possible in the near future to bond porous, hydrophobic bulk metallic glass with microscale lotus structures to the top of a bulk metallic glass microchannel flow network.

It is also recommended that the heat transfer characteristics be investigated. Conclusions from the literature review suggest that vapor phase extraction maintains the high heat transfer characteristics of low quality two-phase flows. Although it was shown that the reduction in the network flow power did not exceed the extraction work for some conditions, it is possible that the improved heat transfer characteristics in this region are such that the extraction work penalty is acceptable. After a better understanding of the physical phenomena present is obtained, the predictive model can be broadened to include local temperature calculations and overall heat transfer characteristics. Infrared imaging of the fractal network could be used to experimentally measure the bulk fluid and wall temperature distributions.

REFERENCES

1. E. M. Sparrow, J.E. Niethammer, and A. Chaboki, Heat transfer and pressure drop characteristics of array of rectangular modules in electronic equipment, *International Journal of Heat and Mass Transfer*, vol. 25, pp. 961-973 (1982).
2. B.A. Jubran, S. A. Swiety, and M.A. Hamdan, Convective heat transfer and pressure drop characteristics of various array configurations to simulate the cooling of electronic modules, *International Journal of Heat and Mass Transfer*, vol. 39, pp. 3519-2529, 1996.
3. D. B. Tuckerman and R. F. W. Pease, High-Performance Heat Sinking for VLSI, *IEEE Electron Device Lett.*, vol. EDL-2, pp. 126-129, 1981.
4. W. Qu and I. Mudawar, Experimental and numerical study of pressure drop and heat transfer in a single-phase micro-channel heat sink, *International Journal of Heat and Mass Transfer*, vol. 45, pp. 2549-2565, 2002.
5. L. Zhang, S. S. Banerjee, J. Koo, D.J. Laser, M. Ashegi, K.E. Goodson, J. G. Santiago, and T.W. Kenny, A micro heat exchanger with integrated heaters and thermometers, *Proceedings of Solid State Sensor and Actuator Workshop*, pp. 275-280, June 2000.
6. H. H. Bau, Optimization of Conduits' Shape in Micro Heat Exchangers, *International Journal of Heat and Mass Transfer*, vol. 41., pp. 2717-2723, 1998.
7. G. B. West, J. H. Brown, and B. J. Enquist, A General Model for the Origin of Allometric Scaling Laws in Biology, *Science*, vol. 276, pp. 122-126, 1997.
8. D. V. Pence, Improved Thermal Efficiency and Temperature Uniformity using Fractal-like Branching Channel Networks, *Proceedings of the International Conference on Heat Transfer and Transport Phenomena in Microscale*, ed. G.P. Celata, Begell House: New York, pp. 142-148, 2000.
9. D. V. Pence, Reduced Pumping Power and Wall Temperature in Microchannel Heat Sinks with Fractal-like Branching Channel Networks, *Microscale Thermophysical Engineering*, vol. 6, pp. 319-330, 2002.
10. D. V. Pence and K. Enfield, Inherent Benefits in Microscale Fractal-like Devices for Enhanced Transport Phenomena, *Design and Nature II: Comparing Design in Nature with Science and Engineering*, WIT Press, pp. 1051-1057, 2004.

11. R. Mertz, A. Wein, and M. Groll, Experimental investigation of flow boiling heat transfer in narrow channels, *Second European Thermal Sciences and 14th UIT National Heat Transfer Conference*, Rome, May 26-31, 1996.
12. W. Qu and I. Mudawar, Measurement and prediction of pressure drop in two-phase micro-channel heat sinks, *International Journal of Heat and Mass Transfer*, vol. 46, pp. 2737-2753, 2003.
13. M. E. Steinke and S. G. Kandlikar, An Experimental Investigation of Flow Boiling Characteristics of Water in Parallel Microchannels, *Journal of Heat Transfer*, vol. 126, pp. 518-526, 2004.
14. L. Jiang, M. Wong, and Y. Zohar, Forced Convection Boiling in a Microchannel Heat Sink, *Journal of Microelectromechanical Systems*, vol. 10, pp. 80-87, 2001.
15. L. Zhang, J. Koo, L. Jiang, M. Ashegi, K. E. Goodson, J. G. Santiago, and T. W. Kenny, Measurement and Modeling of Two-Phase Flow in Microchannels with Nearly Constant Heat Flux Boundary Conditions, *Journal of Microelectromechanical Systems*, vol. 11, pp. 12-19, 2002.
16. B. J. Daniels, D. V. Pence, and J. A. Liburdy, Predictions of Flow Boiling in Fractal-like Branching Microchannels, *ASME2005-82484, Proceedings of IMECE 2005*, Orlando, Florida, 2005.
17. W. Qu and I. Mudawar, Flow boiling heat transfer in two-phase micro-channel heat sinks—I. Experimental investigation and assessment of correlation methods, *International Journal of Heat and Mass Transfer*, vol. 46, pp. 2755-2771, 2003.
18. T.S. Ravigururajan, Impact of channel geometry on two-phase flow heat transfer characteristics of refrigerants in microchannel heat exchangers, *Journal of Heat Transfer*, vol. 120, pp. 485-491, 1998.
19. P.A. Kew and K. Cornwell, Correlations for the prediction of boiling heat transfer in small-diameter channels, *Applied Thermal Engineering*, vol. 17, pp. 707-715, 1997.
20. G.R. Warrier, V.K. Dhir, and L.A. Momoda, Heat transfer and pressure drop in narrow rectangular channel, *Experimental Thermal and Fluid Science*, vol. 26, pp. 53-64, 2002.
21. T. H. Yen, N. Kasagi, and Y. Suzuki, Forced Convective Boiling Heat Transfer in Microtubes at Low Mass and Heat Fluxes, *International Journal of Multiphase Flow*, vol. 29, pp. 1771-1792, 2003.

22. M. Ikeuchi, T. Yumikura, M. Fujii and G. Yamanaka, Heat-transfer characteristics of an internal micro-porous tube with refrigerant-22 under evaporating conditions, *ASHRAE Transactions*, vol. 90, pp. 196-211, 1984.
23. C. N. Ammerman and S. M. You, Enhancing Small-Channel Convective Boiling Performance Using a Microporous Surface Coating, *Journal of Heat Transfer*, vol. 123, pp. 976-983, 2001.
24. J. Thorud, J. A. Liburdy and D. V. Pence, Microchannel Membrane Separation Applied to Confined Thin Film Desorption, *Experimental Thermal Fluids Sciences*, vol. 30, pp. 713-723, 2006.
25. F. M. White, *Viscous Fluid Flow*, 2nd ed., McGraw Hill, New York, NY, pp. 291-293.
26. A. Y. Alharbi, D. V. Pence and R. N. Cullion, Fluid Flow Through Microscale Fractal-like Branching Channel Networks, *Journal of Fluids Engineering*, vol. 125, pp. 1051-1057, 2003.
27. A. Y. Alharbi, D. V. Pence and R. N. Cullion, Thermal Characteristics of Microscale Fractal-like Branching Channels, *Journal of Heat Transfer*, vol. 126, pp. 744-752, 2004.
28. W. Qu and I. Mudawar, Transport phenomena in two-phase micro-channel heat sinks, *Journal of Electronic Packaging, Transactions of the ASME*, vol. 126, pp. 213-224, 2004.
29. L. S. Tong and Y. S. Tang, *Boiling Heat Transfer and Two-Phase Flow*, 2nd ed., Taylor & Francis, Washington, D.C., pp. 120.
30. R. W. Lockhart and R. C. Martinelli, Proposed correlation of data for isothermal two-phase, two-component flow in pipes, *Chemical Engineering Progress*, vol. 45, pp. 39-48, 1949.
31. D. Chisholm, Friction pressure gradient during the flow of boiling water, *Engineering and Boiler House Review*, vol. 78, pp. 287-289, 1963.
32. D. Chisholm, A theoretical basis for the Lockhart-Martinelli correlation for two-phase flow, *International Journal of Heat and Mass Transfer*, vol. 10, pp. 1767-1778, 1967.
33. D. Butterworth and G. F. Hewitt, *Two-phase flow and heat transfer*, Oxford University Press, pp. 58-90.

34. D. Chisholm, *Two-Phase Flow in Pipelines and Heat Exchangers*, Longman, New York, NY.
35. H. J. Lee and S. Y. Lee, Pressure drop correlations for two-phase flow within horizontal rectangular channels with small heights, *International Journal of Multiphase Flow*, vol. 27, pp. 783-796, 2001.
36. K. Mishima and T. Hibiki, Some characteristics of air-water two-phase flow in small diameter vertical tubes, *International Journal of Multiphase Flow*, vol. 22, pp. 703-712, 1996.
37. A. A. Armand, The resistance during the movement of a two-phase system in horizontal pipes, *Izvestiya Vsesoyuznogo Teplotekhnicheskogo Instituta (A.E.R.E. Transactions 828)*, vol. 1, pp. 16-23, 1946.
38. S. M. Zivi, Estimation of steady-state steam void-fraction by means of the principle of minimum entropy production, *Journal of Heat Transfer*, vol. 86, pp. 247-252, 1964.
39. T. S. Zhao and Q. C. Bi, Pressure drop characteristics of gas-liquid two-phase flow in vertical miniature triangular channels, *International Journal of Heat and Mass Transfer*, vol. 44, pp. 2523-2534, 2001.
40. P. M. Y. Chung and M. Kawaji, The effect of channel diameter on adiabatic two-phase flow characteristics in microchannels, *International Journal of Multiphase Flow*, vol. 30, pp. 735-761, 2004.
41. R. K. Shah and A. L. London, *Laminar Flow Forced Convection in Ducts, Supplement 1 to Advances in Heat Transfer*, Academic Press, New York, NY, 1978.
42. R. J. M. DeWiest, *Flow Through Porous Media*, Academic Press, New York, NY, 1969.
43. A. Doerr, Micro-channel Bifurcating Heat Exchanger, *Senior Project Report*, Oregon State University: Mechanical Engineering, 2000.
44. A. Bejan, Constructal Tree Network for Fluid Flow between a Finite-Size Volume and One Source or Sink, *Revue Generale de Thermique*, vol. 36, pp. 592-604, 1997.
45. R. D. Blevins, *Applied Fluid Dynamics Handbook*, Von Nostrand Reinhold Company, New York, NY, 1984.

46. R. J. Phillips, *Forced convection, liquid cooled, microchannel heat sinks*, M.S. Thesis, Department of Mechanical Engineering, Massachusetts Institute of Technology, Cambridge, MA, 1987.
47. F. M. White, *Fluid Mechanics*, 5th ed., McGraw-Hill, New York, NY, 2003.
48. F. P. Incropera and D. P. DeWitt, *Fundamentals of Heat and Mass Transfer*, 5th ed., John Wiley & Sons, New York, NY, 2002.
49. R. S. Figliola and D. E. Beasley, *Theory and Design for Mechanical Measurements*, 3rd ed., John Wiley & Sons, New York, NY, 2000.

APPENDICES

APPENDIX A: TEST MANIFOLD DETAIL DRAWINGS

This appendix contains detail drawings of the test manifold parts and the manifold assembly generated in SolidWorks®. Dimensions for the parts are provided in the drawings and references are made to indicate placement of o-rings, tap sizes, etc. An exploded view of the test manifold assembly is shown in Fig. 1.A. Figure 2.A is the drawing for the clamp parts used to tightly enclose the assembly. The bottom filler part through which the flow enters the microchannels and around which the bottom clamp is attached is found in Fig. 3.A. The flow enters through the center hole and the two outer holes serve to drain the excess water from the fixture. The porous aluminum part that serves as the heating block and a porous medium is shown in Fig. 4.A. The path of the embedded heating wire is outlined by the traced line. Figure 5.A details the top filler part through which the vapor is extracted. The five small ports are for two lead wires for the heating element, two thermocouples, and a pressure transducer. The port towards the end is the excess vapor exit. The encasing part in Fig. 6.A encloses a small volume for the exit liquid and excess vapor.

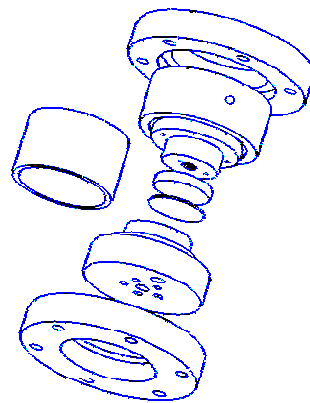


Figure 1.A: Exploded view of the test manifold assembly.

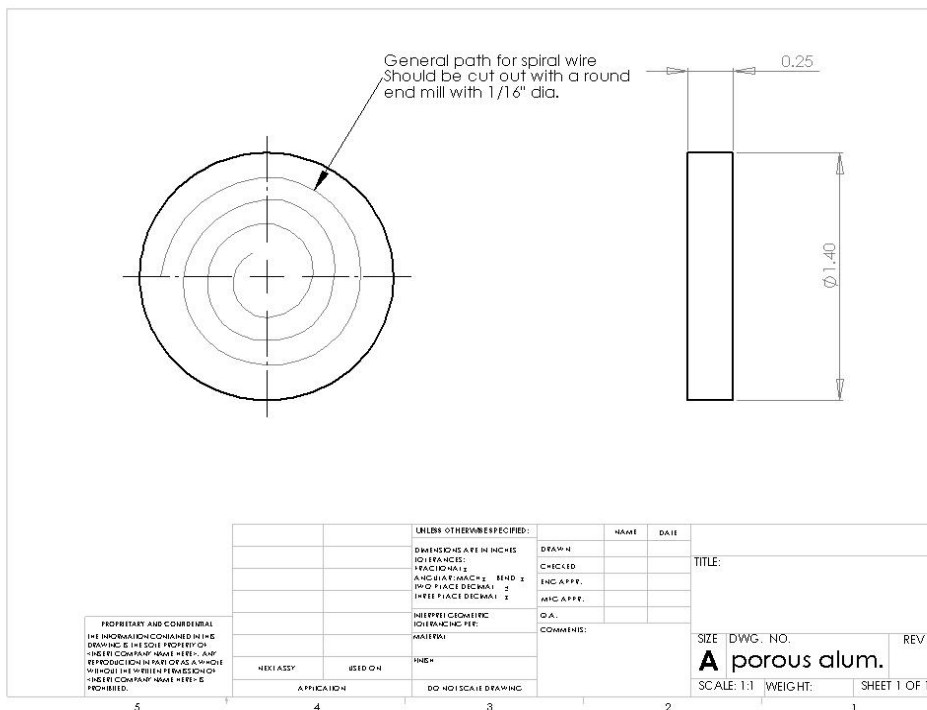


Figure 4.A: Porous aluminum layer with path of embedded wire shown.

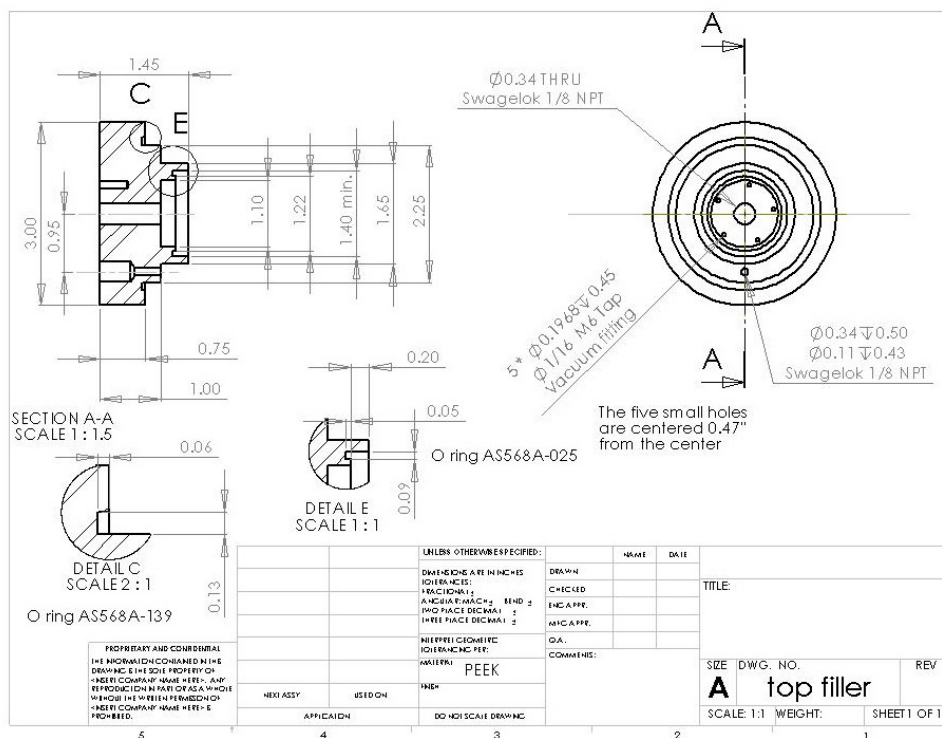


Figure 5.A: Top filler part through which the extracted vapor exits.

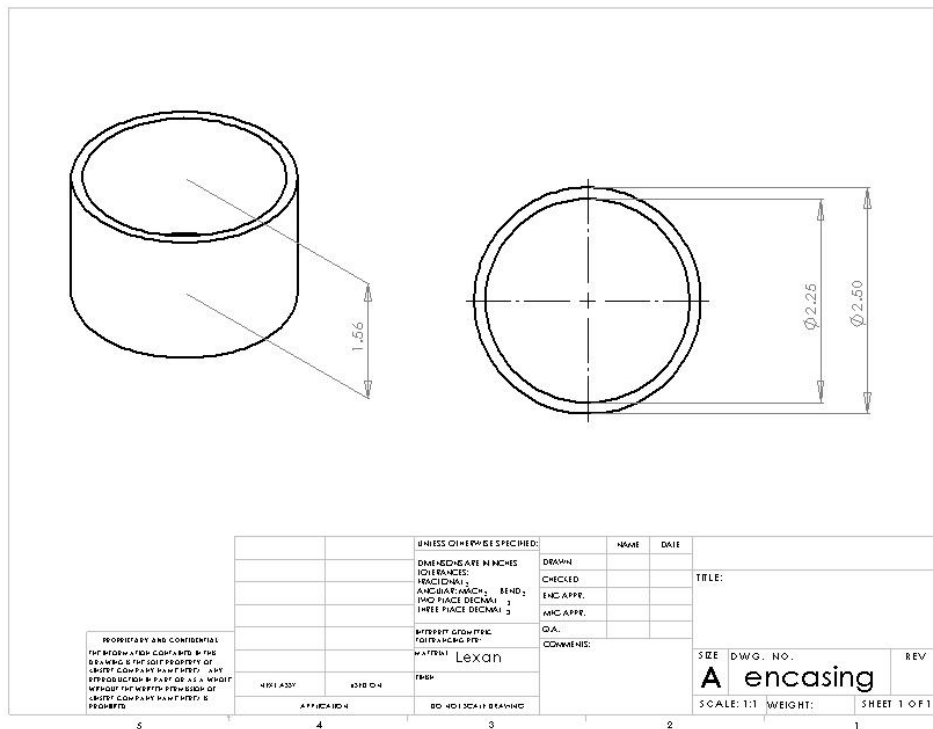


Figure 6.A: Encasing to enclose the inner parts of the test manifold.

APPENDIX B: EXPERIMENTAL SETUP IMAGES

Images of the experimental setup for this thesis project are provided below. Figures 1.B – 5.B are pictures of the experimental flow loop and test fixture. In Fig. 1.B, bare stainless steel tubing enters the hot oil bath. The preheated liquid exits the bath and the line is insulated and wrapped with heater rope to minimize heat losses. Across the heater rope approximately 50 V is applied to maintain the flow just below saturation when it enters the test manifold. The other insulated lines shown in the figure are part of an existing ammonia desorber flow loop. The water supply tank (clear tank in the bottom left), surge tank (grey) and the bladder tank (white) are shown in Fig. 2.B. The black pump draws water from the supply tank to the bladder tank which is pressurized by the surge tank. The catch and weigh system for the extracted vapor is shown in Fig. 3.B. The vapor is condensed in the cold bath and flows into the bottle on top of the scale. The scale is connected to the serial port of the nearby computer and the mass of the catch system is monitored and recorded. The tank pictured in this figure is the reservoir for the liquid and vapor that pass through the microchannels. Figure 4.B shows part of the test loop and how it is integrated with the existing flow loop. The water enters the flow loop from the bottom left and passes through an in-line filter before reaching the first three-way shut-off valve (left edge of figure). The temperature, pressure and mass flow rate are then measured for the inlet flow. After the regulatory needle valve, the flow loop diverges at the second three-way valve. The transducers used to measure the temperature, pressure and flow rate of the exit flow are shown in the right edge of the figure. The test fixture with the

inlet and exit flow lines and its transducers are shown in Fig. 5.B. Figure 6.B is an example of the spiral pattern used to embed the resistance wire in the porous aluminum. The resistance wire is cemented into the grooved pattern and then a thermocouple is cemented to the top surface of the porous aluminum.



Figure 1.B: Image of inlet flow entering and exiting hot oil reservoir to be preheated.



Figure 2.B: Image of supply tank (clear), bladder tank (white) and surge tank (grey).

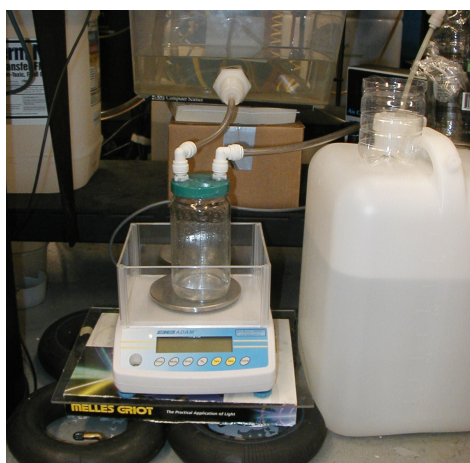


Figure 3.B: Catch and weigh system used to measure flow rate of extracted vapor including liquid collector and condenser.

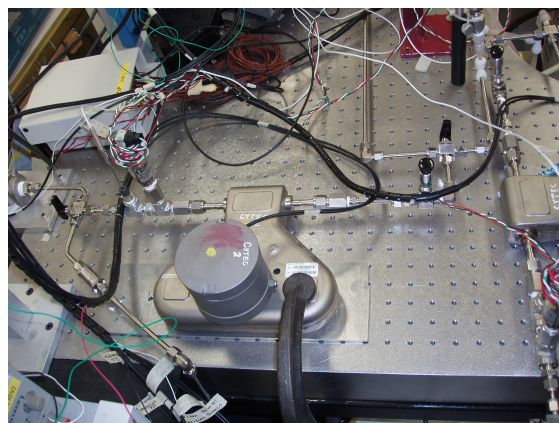


Figure 4.B: Transducers used to measure the temperature, pressure and flow rate of the inlet and exit flow lines.



Figure 5.B: Test manifold with flow lines and its transducers to measure the needed flow properties.



Figure 6.B: Example of the porous aluminum heater used in this project before embedding the resistance wire.

APPENDIX C: COMPONENT LIST

The manufacturer, model and quantity of each component in the experimental flow loop and instrumentation are listed in Tables 1.C and 2.C.

Table 1.C: Experimental flow loop components.

Component	Manufacturer	Model	Quantity
Pump	SHURflo	75421-00	1
Surge tank	AA Tanks	FX 200 V	1
Bladder tank	Elbi	DV-150	1
Air filter	Rti Eliminator	3P-060-M02-F1	1
Water filter	Swagelok	SS-4F-15	2
Ball valve	Sharpe	110J11	3
Three-way valve	Swagelok	SS-42XS4	4
Liquid needle valve	Ideal Valve	V-54-1-11	2
Vapor needle valve	Swagelok	SS-1RS4	1
Flow meter	Micromotion	476702	2
Heat transfer oil	Paratherm	NF	--
Hot oil bath	Thermo Electron	Neslab EX7	1
Cold water bath	Hart Scientific	7320	1
Building air regulator	ARO	CQ493-600-2	1
Bladder air regulator	Control Air	Type 700	1
Cold water pump	March Mfg.	BC-3C-MD	1
Vapor pump	Air Cadet	400-3901	1
Porous membrane	GE Osmonics	R04SH320F5	--
Heater wire	Omega Engr.	NIC60-010-062	--
Thermocouple	Therm-X	TR-120TT-T116-FG-2.5-STR	3
Thermocouple	Omega Engr.	5TC-TT-T-20	1
Pressure transducer	Omega Engr.	PX2300-2DI	1
Pressure transducer	Omega Engr.	PX212-030 AV	3
Pressure transducer	Omega Engr.	PX212-200 AV	1
Pressure transducer	Omega Engr.	PX312-030 AV	1
Vapor scale	Adam	ACBplus-600H	1

Table 2.C: Instrumentation components.

Component	Manufacturer	Model	Quantity
Data Acquisition board	National Instr.	PCI-6043E	2
Terminal blocks	National Instr.	SCB-68	2
DC Power Supply	Agilent	E3617A	2

APPENDIX D: CALIBRATION AND UNCERTAINTY VALUES

The calibration curve, uncertainty and range for each measurement device are given in Table 1.D. The calibration curve or curve fit for each device was found in a manner similar to that explained in §5.2.1. In these equations, V represents the output voltage from the measurement device, I represents the output current and f represents the frequency output of the Coriolis mass flow meters. The scale was connected via the serial port and provided a direct digital output. The uncertainty values are calculated using Eq. 5.30. The uncertainty values are given as absolute values with the same units as indicated next to the device name, with the exception of the mass flow meters. The range for each measurement device is established by the manufacturer.

Table 1.D: Calibration curve, uncertainty, and range for each measurement device.

Measurement Device	Calibration Curve	Uncertainty (\pm)	Range
P_{in} (kPa)	$P_{in} = 2004.17 V_{in} + 1.411$	0.435*	0 – 207
P_{out} (kPa)	$P_{out} = 861.75 I_{out} - 3.373$	0.035#	0 – 14
P_{vap} (kPa)	$P_{vap} = 2037.29 V_{vap} + 1.535$	0.357*	0 – 207
T_{in} ($^{\circ}$ C)	$T_{in} = 1 V_{in} + 2.1892$	0.211*	0 – 980
T_{out} ($^{\circ}$ C)	$T_{out} = 1 V_{out} + 2.1842$	0.213*	0 – 980
T_{vac} ($^{\circ}$ C)	$T_{vac} = 1 V_{vpc} + 2.0227$	0.212*	0 – 980
T_{al} ($^{\circ}$ C)	$T_{al} = 1 V_{al} + 2.0227$	1.000#	0 – 260
\dot{m}_{in} (g / min)	$\dot{m}_{in} = 0.065 f_{in}$	0.116%#	0 – 1361
\dot{m}_{out} (g / min)	$\dot{m}_{out} = 0.065 f_{out}$	0.103%#	0 – 1361
m_{vap} (g)	---	0.005#	0 – 600

* Uncertainty includes both bias and curve fit errors associated with the measurement device.

Uncertainty is manufacturer provided bias error.

APPENDIX E: OPERATING PROCEDURE

A complete operation procedure for using the experimental flow loop to collect experimental data is provided in this section. A schematic of the experimental flow loop is provided in Fig. 4.7. The valve numbers referenced in the body of the operating procedure are written on each valve. A summary of the operating procedure is provided in §4.6.

Filling Bladder Tank (*only if needed*)

- If the bladder tank needs to be filled, open the shut-off valves (**V20** and **V21**) upstream of the bladder tank. Make sure the shut-off valve (**V22**) immediately downstream of the bladder tank is closed.
- Fill the five-gallon supply tank with deionized, degassed water and leave one of the openings uncovered.
- Plug in the pump and allow it to run as long as the water line in the supply tank is above the exit. **Do not let the pump run dry (without water)!**
- Refill the supply tank and pump the water into the bladder tank if needed.
- Unplug the pump, close the supply tank, and close the two shut-off valves upstream of the bladder tank.

Start-up

- Turn on the cold water bath and the cold water pump. Open the drain valve on the back of the bath. Continually monitor the water level in the cold water bath and make necessary adjustments to the needle valve sitting on the bath.
- Set the cold water bath temperature to 1 °C and allow it to come to temperature.
- Turn on the hot oil bath and allow it to come to the desired inlet temperature. Note: make sure that the bath is being controlled by the internal sensor and not the external sensor.
- Make sure the surge tank is connected to the building air supply.
- Position the three-way valve located near the top of the surge tank so that the arrow is pointing towards **W** (water loop).
- Adjust the bladder tank pressure by setting the surge-tank pressure regulator to 30 psi.
- Turn on the vapor mass scale.
- Turn on the data acquisition program (save to a junk file).
- Open the shut-off valve (**V22**) immediately downstream of the bladder tank.

- Turn all four three-way valves (**V4**, **V6**, **V12** and **V24**) on the table so the arrow points towards **W**.
- Adjust the needle valve (**V5**) immediately downstream of the inlet flow meter until the desired inlet flow rate is reached.
- Adjust the exit plenum needle valves (**V23** and **V11**) as needed so that fluid level in the exit plenum is below the fractal but above the liquid drain holes. (It is recommended to mark the level line with an overhead projector pen on the Lexan tube.)
- Turn on the vapor pump and adjust vacuum pressure until the desired pressure is reached in the vapor plenum.
- Turn on the power supply and set the current to the desired amount.
- Turn on the heater rope by plugging it into the variable voltage controller and adjusting the voltage to approximately 50 V.
- Once the inlet temperature reaches steady state (it takes 15 to 40 minutes), adjust the heater rope voltage and/or the oil bath temperature to obtain the desired inlet temperature.

Steady State

- Once at steady state, data collection for a given test run can begin
- Stop the data acquisition program and restart it. Now save the data to a file appropriately named.
- Monitor the inlet flow rate.
- Monitor the fluid level in the exit plenum.
- To reduce the inlet flow rate: tighten needle valve **V5**.
- To increase the inlet flow rate: loosen needle valve **V5**.
- To lower the exit-plenum fluid level: check the inlet flow rate and adjust as needed, loosen the exit liquid needle valve, **V11**, and/or tighten the excess-vapor needle valve, **V23**.
- To increase the exit-plenum fluid level: check the inlet flow rate and adjust as needed, tighten the exit liquid needle valve, **V11**, and/or loosen the excess-vapor needle valve, **V23**.
- Note: It is acceptable if there are small, periodic changes in the exit-plenum fluid level as long as many cycles of data are captured in the acquisition.
- Collect data for approximately 20 minutes.
- Stop the data acquisition program.
- To begin a new test run:
 - adjust the heater rope voltage and/or oil bath temperature, heater current, inlet flow rate, and vapor plenum pressure to new set points
 - restart data acquisition program saving to a junk file
 - allow steady state to be reached
 - follow the **Steady State** instructions

Shut-down

- The shut-down procedure is to ensure the experiment is safely stopped without damaging test equipment or devices.
- Restart the data acquisition program to monitor instrument values during shut-down.
- Turn off the power supply to the wire heater.
- Turn off the oil bath and unplug the heater rope.
- Turn off the cold water pump and the cold water bath. Close the cold water bath drain.
- Turn off the vapor pump.
- As the oil bath and test fixture cools down, maintain the inlet flow rate between 5 and 20 g/min.
- Turn off the scale.
- When the inlet and vapor plenum temperatures are below 40° C, turn all four three-way valves on the table off (arrow pointing in the middle).
- Stop the data acquisition program.
- Before leaving the room, double check that water is not flowing through the test manifold, the cold water bath, cold water pump, power supplies, heater rope and hot oil reservoir are turned off, and the cold water bath drain is closed.

Changing Flow Loops

- Note: if the water flow loop will not be used for a while or the ammonia loop is expected to be used, the following steps need to be observed
- Attach tubing to the inlet line so that the oil bath is bypassed and any possible ammonia flow goes straight to the reservoir.
- Once the oil is at room temperature, drain the oil into the appropriately marked container.
- Once empty, fill the oil bath with the ammonia loop oil.
- Disconnect the Swagelok fittings above the oil bath and remove the lid with the tubing.
- Replace the original oil-bath lid.
- Ensure that the oil bath drain is not leaking.
- Close the shut-off valve immediately downstream of the bladder tank (V22).

APPENDIX F: DESIGN SPECIFICATIONS

This appendix contains analysis performed in order to control the experimental flow loop parameters and to determine the experimental data test range. The first analysis approximates the appropriate oil bath temperature as a function of the inlet flow rate. In the second analysis, an energy balance analysis is used to determine appropriate test points at which to gather experimental data.

Oil Bath Temperature

The length of the tubing in the hot oil bath is approximately 6 m. The outlet bulk fluid temperature of the water can be evaluated using the following relationship for a constant free stream temperature

$$\frac{\Delta T_o}{\Delta T_i} = \frac{T_\infty - T_{m,o}}{T_\infty - T_{m,i}} = \exp\left(-\frac{\bar{U}A_{surf}}{\dot{m}c_p}\right) \quad (1.F)$$

where $T_{m,o}$, $T_{m,i}$ and T_∞ represent the bulk outlet, bulk inlet and free stream temperatures, respectively. The average overall heat transfer coefficient, \bar{U} , includes contributions due to forced convection at the inner surface of the tubing and natural convection at its outer surface. Assuming the resistance to conductance through the tubing is insignificant, the average overall heat transfer coefficient is evaluated as

$$\bar{U} = \frac{1}{\frac{1}{h_{fcv}} + \frac{1}{h_{ncv}}} \quad (2.F)$$

The heat transfer coefficient of forced convection at the inner surface is found using the correlation proposed by Whitaker [48] for developing laminar flows

$$\overline{Nu}_{D,fcv} = 1.86 \left(\frac{Re_D Pr}{L/D} \right)^{1/3} \left(\frac{\mu}{\mu_{surf}} \right)^{0.14} \quad (3.F)$$

where the properties are evaluated at the average bulk temperature except for μ_{surf} , which is evaluated at the surface temperature. The flow is assumed to be hydrodynamically developing throughout its passage in the oil bath due to the bends present in the coils. In using this correlation, it is assumed that the surface temperature of the tubing is constant at a few degrees below the bath temperature. The heat transfer coefficient of natural convection at the outer surface is found using a correlation recommended by Churchill and Chu [48] for isothermal horizontal cylinders:

$$\overline{Nu}_{D,ncv} = \left\{ 0.60 + \frac{0.387 Ra_D^{1/6}}{\left[1 + (0.559/Pr)^{9/16} \right]^{8/27}} \right\}^2 \quad (4.F)$$

The Rayleigh number is defined as

$$Ra_D = \frac{gB(T_s - T_\infty)D^3}{\nu\alpha} \quad (5.F)$$

where g is the gravity constant and B is the volumetric thermal expansion coefficient.

The property values are evaluated at the film temperature or average temperature of the free stream oil and the surface temperature of the tubing. The heat transfer coefficient for both types of convection is obtained from the Nusselt number correlations using its definition

$$Nu_D \equiv \frac{hD}{k} \quad (6.F)$$

Using Eqs. (1.F) – (6.F), the recommended oil bath temperature as a function of mass flow rate is calculated. It was found that the flow exited the oil bath at the same temperature as the oil bath for the flow rates used in this project. To avoid cavitation of the flow from saturation the heater bath temperature was set below the saturation temperature at 99 °C.

Experimental Test Range

An energy balance is used to identify the experimental test range. The inlet mass flow rate is determined by a thermodynamic analysis of the heat sink. The input heat from the wire heater is limited to 30 W due to the hydrophobic membrane operating limit of 180 °C. The inlet subcooling was set at 2.5 °C and an exit quality ranging between 0.04 and 0.1 was desired to avoid complete phase transformation and utilize the low quality regime heat transfer benefits. The thermodynamic equation for evaluating the microchannel flow is

$$\dot{Q}_{frac} = \dot{m}_{in} \{c_p (T_{l,sat} - T_{in}) + (i_{out} - i_l)\} \quad (8.F)$$

$$\text{where} \quad i_{out} = (1 - x_{out})i_l + x_{out}i_v$$

where \dot{Q}_{frac} is the supplied power, c_p is the specific heat of water, T_{in} is the inlet temperature, $T_{l,sat}$ is the saturation or boiling temperature, i_l is the saturation liquid enthalpy, i_{out} is the exit enthalpy evaluated at differing exit qualities (x_{out}), i_v is the saturation vapor enthalpy and \dot{m}_{in} is the inlet flow rate. The first part of Eq. 8.F represents the sensible heat required to raise the flow a few degrees to its saturation temperature. The second part is the latent heat required to vaporize the flow and raise its quality. In this calculation, the effect of extracting the vapor from the flow is

neglected. The range of flow rates tested in the experiments reflects the heating analysis performed here.

APPENDIX G: EXPERIMENTAL DATA AND PREDICTIVE MODEL RESULTS

To validate the predictive model, experimental values of inlet subcooling, inlet flow rate, input energy, vapor plenum pressure and exit plenum pressure values were used as inputs for model predictions. The rest of the results of the experimental data collection and predictive model not reported in Figs. 6.8 and 6.9 are reported in Figs. 1.G – 4.G. The same trends as discussed in §6.2 are observed in Figs. 1.G – 4.G as observed in Figs. 6.8 and 6.9. The normalized vapor extraction results are shown in Figs. 1.G and 2.G versus the normalized membrane pressure difference for an inlet flow rate of 10 and 12 g/min, respectively. The network pressure drop results are shown in Figs. 3.G and 4.G versus the membrane pressure difference for an inlet flow rate of 8 and 12 g/min, respectively.

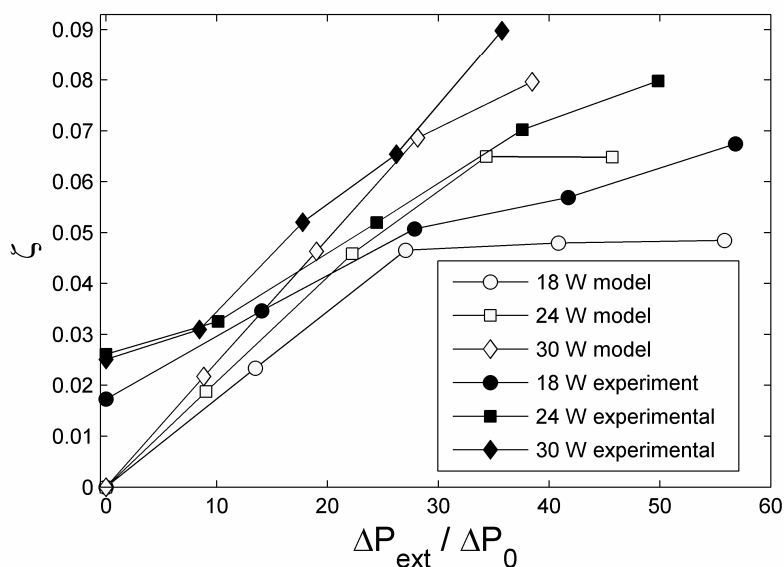


Figure 1.G: Normalized extracted vapor flow rate versus normalized membrane pressure difference of the predictive model and experimental data for an inlet flow rate of 10 g/min.

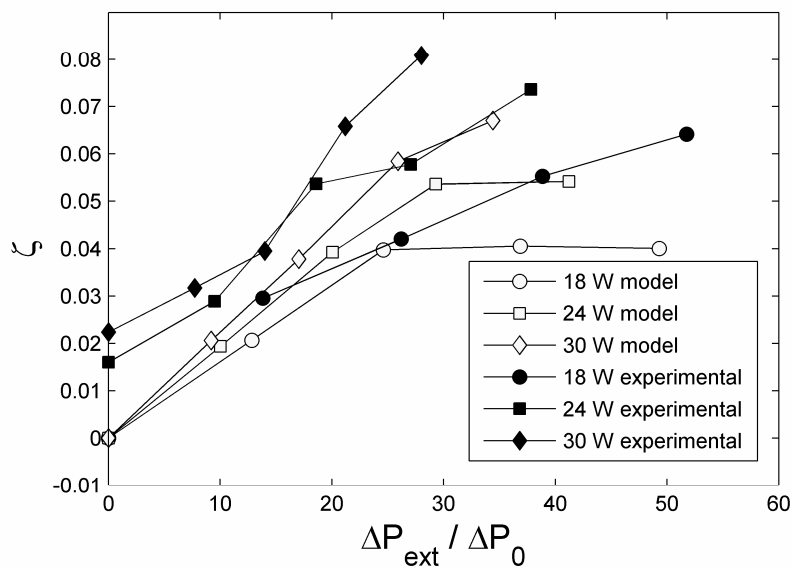


Figure 2.G: Normalized extracted vapor flow rate versus normalized membrane pressure difference of the predictive model and experimental data for an inlet flow rate of 12 g/min.

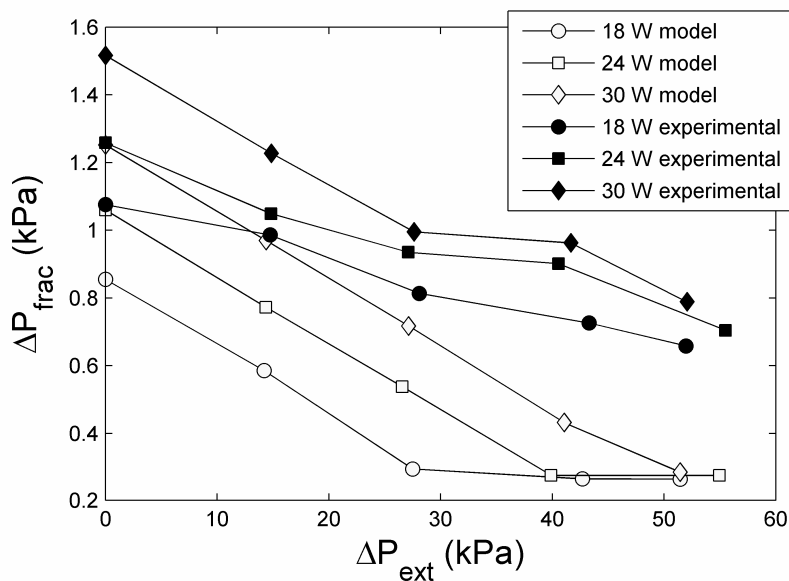


Figure 3.G: Network pressure drop versus membrane pressure difference of the predictive model and experimental data for an inlet flow rate of 8 g/min.

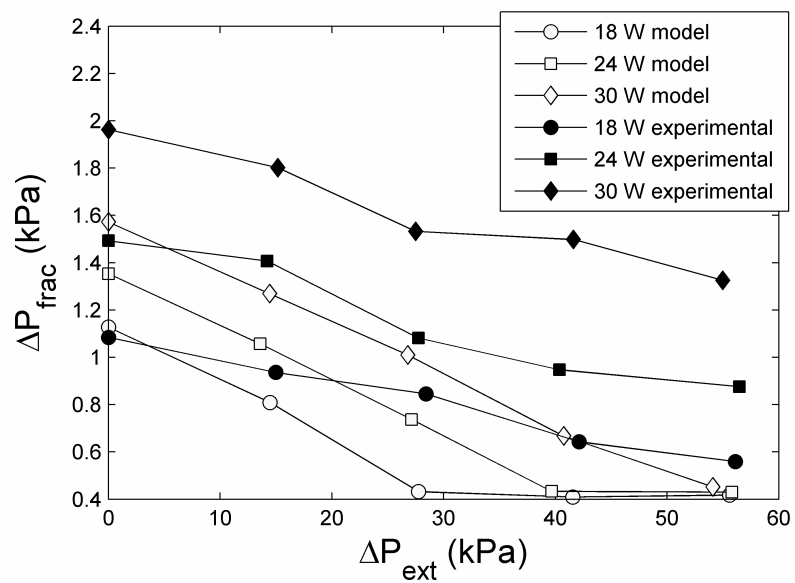


Figure 4.G: Network pressure drop versus membrane pressure difference of the predictive model and experimental data for an inlet flow rate of 12 g/min.

APPENDIX H: SINGLE-PHASE SENSITIVITY ANALYSIS

The experimental data network pressure drop values were adjusted using experimental single-phase pressure corrections. The experimental single-phase pressure drop was compared between the predictive model and the experimental data for three single-phase points with similar inlet conditions as those associated with the two-phase data collection. The pressure drop difference between the experimental reference points and the predictive model were used as the pressure drop correction in analyzing the experimental data. A sensitivity analysis was performed on the single-phase reference points to quantify the effect of uncertainty values on the pressure correction. The base cases had an inlet flow rate of 8, 10 and 12 g/min, a membrane pressure difference of 0 kPa, no energy input, inlet subcooling of 2.5 K, exit plenum pressure of 101 kPa and a microchannel height of 200 μm . The energy input and

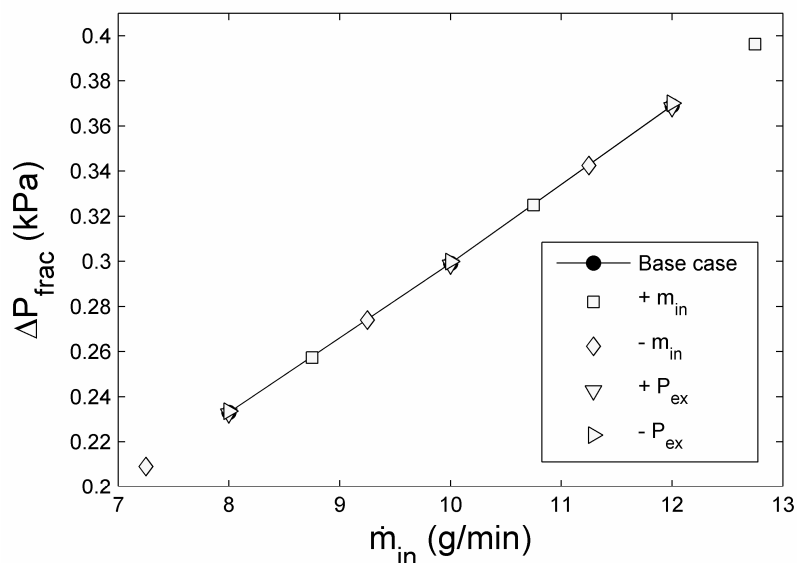


Figure 1.H: Single-phase sensitivity analysis of the network pressure drop versus the inlet flow rate for perturbed values of the inlet flow rate and exit plenum pressure.

membrane pressure difference were not perturbed because the analysis is performed for adiabatic single-phase flow. The sensitivity analysis of the inlet subcooling in the two-phase flow indicated that its uncertainty had negligible impact on the network pressure drop. The sensitivity analysis of the inlet flow rate, \dot{m}_m , and exit pressure, P_{ex} , is shown in Fig. 1.H. The pressure drop changed linearly with the change in the inlet flow rate similar to the two-phase sensitivity analysis. The change in the exit plenum pressure has a negligible effect on the single-phase pressure drop. The sensitivity analysis of the microchannel height is presented in Fig. 2.H showing the same inverse square relationship between the network pressure drop and channel height as observed in the two-phase sensitivity analysis. The combined effect of inlet flow rate and channel height uncertainty results in an uncertainty of 0.08 kPa in the pressure correction.

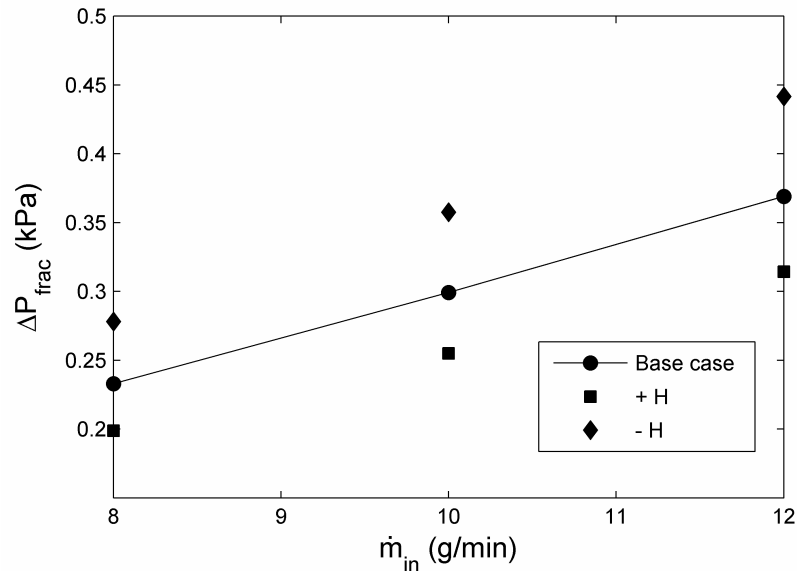


Figure 2.H: Single-phase sensitivity analysis of the network pressure drop versus the inlet flow rate for perturbed values of the microchannel height.

